# University of Alberta

Characterization of Radiation Induced Current in RF coils of Linac-MR Systems

by

Benjamin Lester Burke

A thesis submitted to the Faculty of Graduate Studies and Research
in partial fulfillment of the requirements for the degree of

Doctor of Philosophy

in

Medical Physics

Department of Physics

©Benjamin Lester Burke

Spring 2013
Edmonton, Alberta

Permission is hereby granted to the University of Alberta Libraries to reproduce single copies of this thesis and to lend or sell such copies for private, scholarly or scientific research purposes only. Where the thesis is converted to, or otherwise made available in digital form, the University of Alberta will advise potential users of the thesis of these terms.

The author reserves all other publication and other rights in association with the copyright in the thesis and, except as herein before provided, neither the thesis nor any substantial portion thereof may be printed or otherwise reproduced in any material form whatsoever without the author's prior written permission.

# Abstract

Real-time MR imaging of the cancer patients undergoing external beam radiation treatment represents the next generation in image guided radiotherapy. However, the radio frequency (RF) coil of the MRI is exposed to the pulsed radiation of the linear accelerator in the systems where a medical linear accelerator is integrated with the MRI. This thesis is primarily concerned with the instantaneous effect of pulsed radiation on the RF coils, in particular the Radiation Induced Current (RIC). The RIC results from the charge imbalance created by the ejection of Compton electrons from the thin conductors of the RF coils during the pulsed irradiation. This work spans the initial observations of the RIC in real coils, a detailed characterization of the RIC and finally its impact on the MR image. The first part presented the measurements of the instantaneous RIC in two different MRI RF coils. Some basic characterization of the RIC included the isolation of the RF coil component responsible for RIC, the dependence of RIC on linear accelerator dose rate, and the effect of placing wax buildup on the coil to reduce RIC. The copper windings of the RF coils were isolated as the main source of RIC. A linear dependence of the RIC amplitude on dose rate was observed. The RIC was decreased with wax buildup, suggesting an electronic disequilibrium as the cause of RIC. In the second part, a buildup method of RIC removal in planar conductors is tested, a Monte Carlo method of RIC calculation in metal conductors is presented and validated, and the Monte Carlo method is used to examine the effects of magnetic fields on both planar conductor and practical cylindrical coil geometries. The buildup method of RIC removal is effective in

planar geometries and in cylindrical coil geometries when the coil conductor is in direct contact with the patient. The presence of air gap between the coil and patient makes this method of RIC removal less effective although placing buildup still reduces the RIC by up to 60%. The SNR is improved in the images obtained concurrently with radiation if buildup is applied to the coil. The final part examined the effect of RIC on MR image quality. Imaging experiments were performed on the prototype linac-MR system and the RIC-induced signal-to-noise ratio (SNR) degradation of MR images was quantified. An image post-processing algorithm was proposed which removes some of the RIC-corrupted data from the MR images to recover some of the lost image SNR. The presence of RIC in MR RF coils leads to a loss of SNR which is directly related to the linac dose rate. The RIC related loss in SNR is likely to increase for future commercial systems that are likely to provide larger dose rate than the prototype system (250 cGy/min).. Some of this SNR loss can be recovered through the use of a post-processing algorithm which removes the RIC artefact from the image k-space.

# Table of Contents

# List of Tables

# List of Figures

# List of Abbreviations

| | |
|---|---|
| CBCT | Cone Beam Computed Tomography |
| CDF | Cumulative Distribution Function |
| CPE | Charged Particle Equilibrium |
| CT | Computed Tomography |
| CTV | Clinical Target Volume |
| DCS | Differential Cross Section |
| EPID | Electronic Portal Imaging Device |
| FID | Free Induction Decay |
| GTV | Gross Tumour Volume |
| IGRT | Image Guided Radiotherapy |
| IMRT | Intensity Modulated Radiation Therapy |
| KV | Kilovoltage |
| Linac | Linear Accelerator |
| OBI | On-board Imager |
| MC | Monte Carlo |
| MLC | Multileaf Collimator |
| MRI | Magnetic Resonance Imaging |
| MV | Megavoltage |
| MVCT | Megavoltage Computed Tomography |
| NMR | Nuclear Magnetic Resonance |
| PDF | Probability Distribution Function |
| PTV | Planning Target Volume |

| | |
|---|---|
| RBP | Rotating Bi-Planar |
| RF | Radio frequency |
| RIC | Radiation Induced Current |
| RT | Radiation Therapy |
| SNR | Signal-to-Noise Ratio |

# 1 Introduction

## *1.1 Introduction to Radiation Therapy*

Radiation therapy (RT), also called radiotherapy, has been a primary tool in both the treatment and palliation of cancer for many years. Its effectiveness at destroying cancerous tissue ensures that it will continue to be used in the years to come. The RT process begins with the discovery of cancer through the use of diagnostic imaging, biopsy techniques and other medical tests. In radiotherapy planning, a 3-dimentional (3-D) shape, also known as the gross tumour volume (GTV), is delineated in high resolution diagnostic images of the patient [ICRU50, 1993; ICRU62, 1999]. A small 3-D margin is added to the GTV to account for the areas surrounding the tumour where microscopic tumour spreading is suspected and the whole volume is referred to as the clinical target volume (CTV) [ICRU50, 1993; ICRU62, 1999]. The CTV is the intended target for the radiation beam used in RT; ideally only the CTV would be irradiated and there would be no normal tissue damage. However, during the course of RT inevitable uncertainties in the tumour location occur, due in part to daily patient setup error and in part to internal tumour motion [van Herk, 2004]. This requires an additional 3-D margin to be placed around the CTV. The setup error is a geometric error arising from small differences in patient setup with respect to the RT treatment beams during the course of fractionated RT. Organ motion refers to movement of the tumour, critical structures or both due to normal physiological functions of the body, such as respiration. With this last 3-D margin added, the total volume is now called the

planning target volume (PTV) [ICRU50, 1993; ICRU62, 1999]. Treatment plans covering the PTV with a prescribed dose then ensure that the CTV will receive the proper therapeutic radiation dose despite the uncertainties mentioned above. Treatment plans also ensure that a minimum possible dose is delivered to the healthy tissue and the radiation sensitive critical structures surrounding the tumour.

### 1.1.1 Intensity-modulated RT

Advances in radiotherapy have allowed cancer treatment to improve by having higher energy treatment beams and the delivery of more conformal doses, which allow dose escalation to the tumour volume while minimizing the irradiation of surrounding normal tissues [Verellen, et al., 2007]. The advent and improvement of 3-D treatment planning improved conformal radiation dose delivery, leading to greater tumour control and eradication [Verellen, et al., 2007; Dawson, et al., 2007]. Intensity modulated radiation therapy (IMRT) uses high energy photon beams, whose intensity varies spatially, in order to deliver tightly shaped dose distributions around the PTV, thus allowing the treatment of tumours in close proximity to critical structures. The addition of multileaf collimators (MLCs) was an important step for computer controlled delivery of IMRT [Bernier, et al., 2004], allowing for a steeper falloff of the radiation dose from the PTV to nearby normal tissue thus ensuring increased sparing of critical organs.

The steeper dose falloff afforded by the modern IMRT planning and delivery necessitates highly reproducible setup of the patients' tumour with respect to the beam, such that the probability of a geographic miss is reduced.

Thus, the advances in treatment planning and delivery are only useful if the tumour can be accurately imaged and contoured, and the patient accurately set up for the treatment. Accurate daily localization of diseased volume may also allow for the reduction in the margins around the tumour, used to account for setup uncertainty, and normal tissue sparing [Bernier, et al., 2004; Dawson, et al., 2007; Verellen, et al., 2007]. Alongside the aforementioned advances in RT, there has been significant progress in methods to image the patient as well.

On the treatment planning side, a revolution in radiotherapy was created in the 1970s by the introduction of computed tomography (CT) imaging of tumours. CT imaging, for the first time, provided tumour and normal tissue delineation in 3-D and the *in vivo* electron density information required for accurate radiation dose calculation, such that conformal radiation dose distributions using multiple, shaped treatment beams could be planned [Bernier, et al., 2004]. Slowly, magnetic resonance imaging (MRI) was introduced in radiotherapy planning to overcome the limitations of CT imaging related to iso-dense tumours, e.g. in central nervous system and soft-tissue sarcoma [Bernier, et al., 2004]. In these cases, visual contrast between tumour and surrounding normal tissue and soft tissue organs is too poor in CT for accurate delineation, although CT is still typically used to obtain the electron density information for radiation dose calculation [Verellen, et al., 2007; Dawson, et al., 2007]. MRI's exquisite soft tissue contrast is ideal for visual separation of the tumour from the surrounding normal tissues providing very accurate delineation of GTV. Substantial efforts are underway to map the MRI images into electron density via segmentation through

a process called MRI simulation [Chowdhury, et al., 2012; Nurushev, et al., 2011]. Therefore, it is likely that MRI will become the primary imaging modality for radiotherapy planning.

### 1.1.2 Treatment errors: organ motion and setup variability

As mentioned in section 1.1.1, the goal of IMRT is to deliver a conformal radiation dose to the tumour volume, and spare the surrounding normal tissues and critical structures. However, there are a few sources of uncertainty in the overall process of IMRT planning, verification and delivery that prevent the full benefit of IMRT for the patients [van Herk, 2004]. Patient setup error and internal organ motion are the most important sources of such uncertainty.

Setup error is the geometric error in positioning the patient with respect to the treatment beams during the course RT. Organ motion occurs during a RT treatment session where the tumour volume and/or critical structures move due to respiration and other physiological functions. Much work has been done to quantify and understand organ motion [van Herk, 2004; Rietzel, et al., 2004; Langen, et al., 2001; Webb, 2006]. Many different mechanisms have attempted to account for organ motion such as respiratory gating, mathematical modeling of breathing and motion, fiducial markers for tracking and many more [Webb, 2006]. The majority of the schemes proposed in [Langen, et al., 2001] and [Webb, 2006] either rely on pre/post treatment session imaging to estimate what movement occurred during the treatment or modeling the movement mathematically to calculate errors. An ideal system would image the tumour in real-time during the treatment fraction and align the radiation beam to the current

position of the tumour. This is called image-guided radiotherapy (IGRT) and is the driving force behind the research presented in this thesis.

## *1.2 Current IGRT techniques*

### 1.2.1 Portal imaging

The most widespread IGRT technology is the electronic portal imaging device (EPID) [Verellen, et al., 2007]. EPIDs use the megavoltage (MV) photon beam of the linear accelerator (linac) and an image receptor to provide 2-D MV radiographic images of the patient in the treatment position, on the day of treatment. Generally these images are used for positioning verification, but can also be used for dose monitoring [Verellen, et al., 2007; Van Dyke, 1999]. Due to the small differences in beam attenuation at MV photon energies between various tissue types and the overlaying of 3-D structures onto a 2-D plane, EPIDs suffer from poor soft tissue contrast. The latter problem has been circumvented by rotating the EPIDs to obtain images at various angles, providing MV cone beam CT (CBCT) images. However, soft tissue contrast in the MV CBCT images is generally much poorer compared to the planning CT images. MV CBCT cannot be used to image the patient in real-time due to the mechanical rotation needed for the collection of the projection data.

### 1.2.2 Kilovoltage imaging

The lack of contrast at MV energies can be somewhat improved by using an on-board imager (OBI), which incorporates a kilovoltage (KV) x-ray source and 2-D image detector, similar to an EPID, mounted perpendicular to the treatment beam

[Verellen, et al., 2007; Dawson, et al., 2007]. The OBI provides kV projection images that have better contrast than the corresponding MV portal images. The radiographs at two orthogonal angles are then compared with the corresponding digitally reconstructed radiographs obtained from the planning CT to align the patient in the treatment beam coordinate system, generally based on matching the bony anatomy in two image sets. In some cases fiducial markers, such as gold seeds, are implanted in the solid tumours and can be imaged with OBI systems to provide a match based on the tumour location. In addition, the OBI system can rotate around the patient to create kV CBCT images. CBCT images are generally compared with the patient's planning CT images to align the patient's internal organs in 3-D. OBI systems are generally used for pre-treatment alignment of the patients' bony anatomy and/or 3-D tumour location. They cannot provide 3-D images of the patient in real-time due to the prolonged mechanical rotation of the kV source and image receptor necessary for collecting CBCT projection data.

### 1.2.3 Ultrasound

Ultrasound visualizes soft tissues through the use of ultrasonic waves. The reflection of these waves from different tissue interfaces forms the basis of this imaging technique [Kim, et al., 2006]. Ultrasound is useful in imaging muscle and soft tissue; as such it was commonly used for target localization in prostate treatments [Kim, et al., 2006] before the widespread availability of OBI systems. Ultrasound imaging has the benefit of not increasing patient dose and is generally not uncomfortable for the patient. However, the image quality degrades quickly if there are gaseous regions between the transducer and imaging object; therefore it

is not suitable for lung imaging [Kim, et al., 2006]. Ultrasound image quality is also highly dependent on the skill of the operator and this lack of reproducibility resulting from the subjectivity of both the operation and interpretation of the images is highly undesirable. Finally, since an operator must be present during its use, imaging is not possible during the radiation treatment.

### 1.2.4 Tomotherapy

Another approach to IGRT is helical Tomotherapy, which combines helical CT imaging with a 6 MV linac [Mackie, et al., 1993; Mackie, et al., 1999; Verellen, et al., 2007; Dawson, et al., 2007]. The kV X-ray tube in the CT scanner has been replaced with a 6 MV linac and the CT collimating jaws have been replaced with an MLC to enable IMRT. The system has two beam settings: a 3.5 MV imaging beam and a 6 MV treatment beam. The patient is treated with IMRT as the couch is translated through the bore of the scanner. MVCT images can be acquired with the patient in the treatment position, but images cannot be acquired during treatment because the same linac is used for both imaging and treatment. MVCT images have much poorer contrast compared to the planning CT images, thus, 3-D bony anatomy is generally used for pre-treatment alignment of the patient with the treatment coordinate system.

While the image based patient alignment methods discussed above provide 2-D or 3-D anatomical information of the patient in treatment position, they cannot be used for tracking moving tumours. In some cases, fiducial markers have been implanted in the tumour and EPIDs have been used for tracking the motion of the fiducial markers as a surrogate of tumour motion. There are difficulties

associated with this approach. Since the modulated treatment beam is used for fiducial imaging, the fiducials may be obscured by the MLC for a fraction of beam-on time. In general, it is not always easy to auto-detect the fiducials in MV radiographs. Fiducials can also move within the tumour causing tracking errors [Webb, 2006].

There are other approaches to tumour tracking that do not require radiographic imaging per se. Two of these are mentioned below.

### 1.2.5 Optical Tracking

Optical tracking has been used to track respiration induced motion. The system generally employs an infrared camera along with reflective markers placed on the patient's skin to track the diaphragm movement [Vedam, et al., 2003] – an example of this is the Varian RPM system (Varian, Inc., Palo Alto, California, USA). The camera tracks the motion of the reflective markers as a surrogate for the tumour motion. This system is able to function during beam on; however, the drawback is that there is only non-definitive, correlative information about tumour motion; the tumour's actual position is not known as this is not an imaging system. The consistency of the tumour-surrogate relationship has been questioned [Hosiak, et al., 2004] and use of these systems can lead to geographic misses of the tumour. The system only works for a small patient population who have been deemed highly reproducible in their breathing patterns.

### 1.2.6 Radio frequency tracking

The Calypso system (Calypso Medical Technologies, Seattle, WA, USA) uses electromagnetic transponders, permanently implanted in the patient's prostate, to emit radio frequency (RF) signals which convey the position and movement of the prostate during RT. This system has been shown to provide sub-millimetre accuracy in phantom studies [Balter, et al., 2005]. Again, this system does not provide a 3-D image of the tumour and the implantation of the transponders is very invasive.

## *1.3 MRI for real-time IGRT*

Current IGRT methods do not provide direct tumour imaging in real-time. As a consequence, tumours cannot be tracked in real-time and the margins required for combating internal tumour motion still remain substantial. This still prevents further escalation of radiation dose to the tumour, especially if the dose limiting critical structure is close to the tumour. For IGRT to further improve a system capable of providing high quality, 3-D images of the tumour volume in real-time is required. The use of MRI as the imaging modality in such a system is ideal because MRI can provide exquisite soft tissue contrast. MRI does not use ionizing radiation so no unintended radiation dose is delivered to the patient and, importantly, it is capable of image acquisition during treatment beam-on to provide real-time imaging. The integration of MRI with a teletherapy RT unit is being investigated by a few other centers and each of these systems is briefly described below.

### 1.3.1 Research at other centers

#### 1.3.1.1 Viewray

A research group at the University of Florida developed a system which has been commercialized into a device called Renaissance™ (ViewRay, Inc., Gainesville, Florida, USA). This system is comprised of an 0.35 Tesla, double-doughnut MRI system coupled with three RT heads, each a containing 15,000 Curie Cobalt 60 source, 120 degrees apart [Dempsey, 2006; Mutic, 2012]. IMRT is possible with this system through the doubly focused MLCs that collimate each head. The center of the MRI field of view is coincident with the radiotherapy isocenter to allow the acquisition of 4-D cine MRI. The system can: assess intra-fractional movement of the tumour volume, provide soft tissue localization and reconstruct the daily dose delivered to the patient [Dempsey, 2006]. The radiation beams are oriented perpendicular to the main magnetic field direction, resulting in the well known electron return effect [Raaijmakers, et al., 2005]. The low field used by the system will have reduced magnetic field effects on the dose distributions inside the patient that create hot and cold spots near the lung-soft tissue interface, and around the other naturally occurring air cavities [Kirkby, et al., 2010]. The system could have difficulties arising from the ferromagnetic nature of Cobalt disturbing the magnetic field homogeneity, though it is expected that these obstacles have been overcome in their commercial unit. Since this system is now controlled by private entrepreneurs, the current state of system development is unknown to the research community although reports of MRI alone operation have recently become available [Hu, et al., 2012]. The machine may suffer longer treatment

times compared to linac-based systems due to the lower dose rate of $Co^{60}$, but these longer times will be reduced by their use of three $Co^{60}$ sources.

#### 1.3.1.2 MRI-accelerator

A research group from the UMC Utrecht have a design for a system they call the MRI-accelerator, which integrates a closed-bore 1.5 Tesla MRI system with a 6 MV linear accelerator [Lagendijk, et al., 2008]. Their experimental device has the linac placed next to the MRI system [Raaymakers, et al., 2009] to avoid unwanted interferences between the two systems. In the final design the linac will rotate around the stationary MRI scanner and the radiation beam must therefore pass through the MRI scanner before reaching the patient. The system uses a modified cylindrical, superconducting magnet which displaces both the superconducting coils and gradient system from the part of the cylindrical surface around which the linac is projected to rotate. The radiation beam is designed to be perpendicular to the main magnetic field. There are specially designed coils in the cryostat that oppose the main magnetic field, so that the magnetic field is reduced to very small levels at the location of linac mounting. Also, the linac will rotate outside the specially designed Faraday cage to avoid RF interference. The high field MRI system provides a benefit to imaging as the signal-to-noise ratio (SNR) will be inherently higher. Disadvantages to this system include the MR scanner being in the radiation beam path, and, more importantly, the perpendicular orientation to the linac beam of the high magnetic field strength can affect patient dosimetry [Kirkby, et al., 2010], creating hot and cold spots in the patients. This group has published several papers with dosimetric results and technical considerations

[Lagendijk, et al., 2008; Raaymakers, et al., 2009; Raaymakers, et al., 2004; Raaijmakers A. , et al., 2007a; Raaijmakers, et al., 2007b].

### 1.3.2 Linac-MR at the Cross Cancer Institute

Our research group at the Cross Cancer Institute and the University of Alberta have designed and successfully integrated a low field, 0.2 Tesla, bi-planar MRI with a 6 MV linac [Fallone, et al., 2009]. This small scale prototype has been used to study several aspects of linac-MR integration including, but not limited to, RF noise, RF shielding, MLC tolerance to magnetic fields, tumour tracking and radiation induced currents [Burke, et al., 2009; Burke, et al., 2010; Lamey, et al., 2010a; Lamey, et al., 2010b; Lamey, et al., 2010c; Yun, et al., 2010; Yun, et al., 2012; Burke, et al., 2012; Burke, et al., 2012]. Two other, full-scale, prototypes have been designed and are being constructed as this work is being written; these designs can be seen in Figure 1.1 and Figure 1.2. In both prototypes the linac, magnet structure and gradient coils will rotate in unison about a single rotational axis. Figure 1.1 shows the 'perpendicular' or transverse orientation of the rotating bi-planar (RBP) system. In this design the radiation beam is mounted perpendicular to the main magnetic field direction and also perpendicular to the head-to-toe patient direction. Figure 1.2 shows the 'parallel' or longitudinal orientation of the RBP system. In this system the linac is rotated by 90° from the transverse system, so that now the radiation beam is parallel to the main magnetic field and still perpendicular to the head-to-toe patient direction (Figure 1.2).

Several other aspects of linac-MR integration have also been investigated using computer simulation and experimental means, such as: magnet design and

optimization [Tadic, et al., 2010; Tadic, et al., 2011; Tadic, et al., 2012]; linac simulation and design [St. Aubin, et al., 2010a; St. Aubin, et al., 2010b; St. Aubin, et al., 2010c; St. Aubin, et al., 2010d; St. Aubin, et al., 2010e; St. Aubin, et al., 2010f], and magnetic shielding [Santos, et al., 2012]; dosimetry in magnetic fields [Kirkby, et al., 2008; Kirkby, et al., 2009; Kirkby, et al., 2010; Keyvanloo A. , et al., 2012]; MR-based treatment planning [Stanescu, et al., 2008; Wachowicz, et al., 2010].

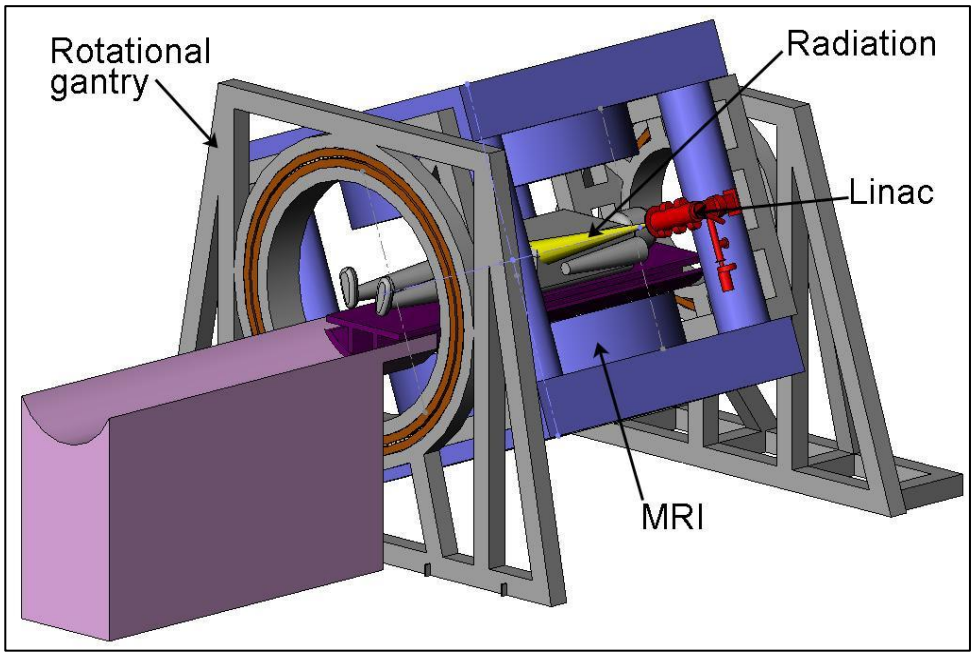


**Figure 1.1 - Perpendicular configuration of linac-MR system designed at Cross Cancer Institute. The linac (red) is mounted so that the radiation beam (yellow) is perpendicular to the main magnetic field. The split solenoid magnetic is shown in blue and the rotational gantry in gray. The linac and MRI will rotate as one piece.**

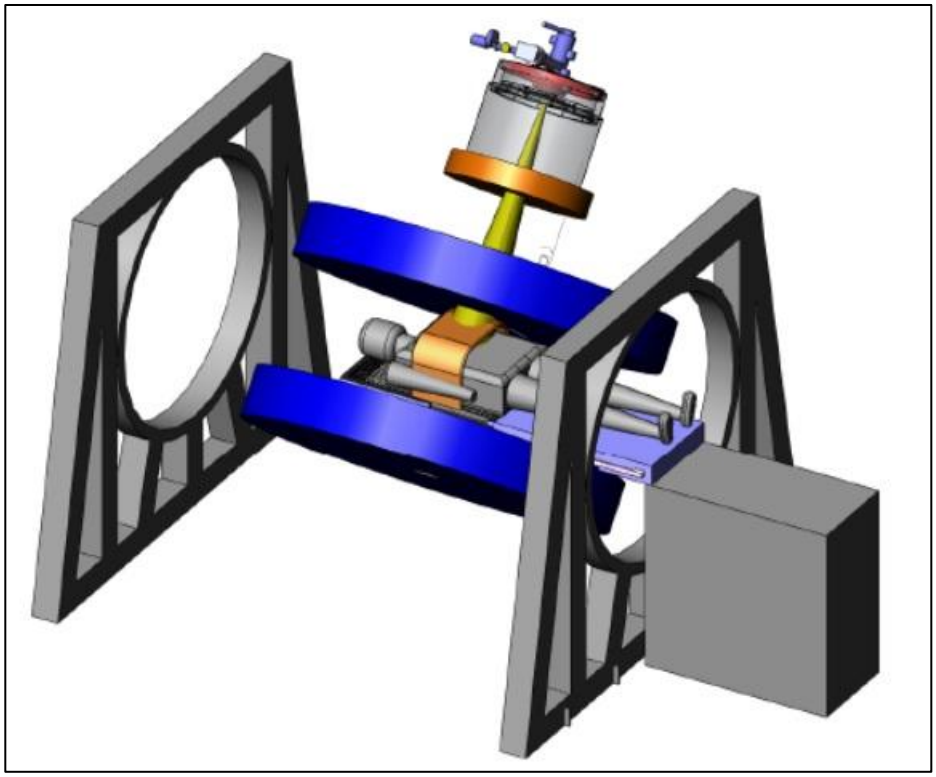

**Figure 1.2 - Parallel configuration of linac-MR system. The radiation beam (yellow) is now parallel to the main magnetic field of the split solenoid magnet (blue). The radiation beam is also shown striking an RF coil (copper) surrounding the patient.**

## *1.4 Research Motivation*

In the integrated teletherapy and MRI systems, the RF coils used for MR imaging will be irradiated directly. There are different categories of radiation induced effects which could result from the RF coils being in the radiation beam: (1) instantaneous effects – coincide with the linac radiation pulses, or $Co^{60}$ beam on time, and include radiation induced current, (2) accumulative effects – long term effects resulting from continued radiation and could include partial or permanent damage to coil hardware, and (3) dosimetric effects – possible modification of the patient skin dose caused by the presence of the RF coil in the beam trajectory. All of these effects should be studied and understood; however, this work will constrain itself to the instantaneous effects, namely the radiation induced current.

The radiation induced current is a transient phenomenon coinciding with the time of irradiation of the RF coils and, as such, its impact will be larger for a linac based system than a $Co^{60}$ based system since the dose per pulse for a linac is generally three orders of magnitude higher than the instantaneous dose from a $Co^{60}$ based system.

## *1.5 Thesis Outline*

The radiation induced current (RIC) present in MRI RF coils when exposed to the pulsed radiation of the linac could interfere with proper MR imaging. The goals of this project are: (1) to characterize the RIC in RF coils – perform some simple measurements to determine the source of RIC and some of its properties, (2) model the RIC using Monte Carlo simulations, (3) use the Monte Carlo simulations to devise a method to eliminate or reduce the RIC in the RF coils, (4) incorporate magnetic fields into the simulations to determine the effect of magnetic field strength and direction on the RIC, and (5) use the linac-MR prototype to image with linac radiation and examine the effect of RIC on the MR images. These goals will be addressed in the following chapters.

Chapter two will present the theory associated with the work contained herein. It will begin with a description of some basic principles of radiation physics along with a description of RIC, a brief review of the scientific literature, and an explanation for RIC presence in RF coils. A brief introduction to Monte Carlo methods and the Monte Carlo program PENELOPE [Salvat, et al., 2009] will follow. Finally, the basic concepts of MR imaging will be presented.

Chapter three presents the results of a series of preliminary measurements. These measurements examine the following: (a) the effect of RF shielding, through the use of a Faraday RF cage, on RIC measurement, (b) the isolation of the RF coil component that is producing the RIC, (c) the effect of dose rate on RIC, (d) the change in RIC due to the application of wax buildup to the RF coils, and (e) a time and frequency analysis of RIC measured on two different RF coils. The purpose of this chapter was to complete the objective item (1) from above.

Chapter 4 presents the Monte Carlo RIC simulation algorithm and its validation against measurements. The use of buildup material to reduce the RIC in RF coils is explained and tested. RIC simulations are then used to test the buildup method using various RF coil geometries. Finally, magnetic fields are incorporated into the simulations and the effects of both magnetic field strength and direction on RIC, and its subsequent reduction using buildup, are examined. The purpose of this chapter is to complete objectives (2)-(4) from above.

Chapter 5 examines the effect of RIC on MR images using the linac-MR prototype. The effect of RIC on image SNR as a function of: linac repetition rate, imaging repetition time (TR), RF coil and imaging sequence are discussed. A post-processing algorithm for the removal of the RIC artefact from the MR data is presented and tested. This chapter completes the final objective, (5), from above.

Finally, chapter 6 summarizes and concludes the work presented and discusses future research possibilities.

## 1.6 References

Balter, J., Wright, J., Newell, J., Friemel, B., Dimmer, S., Cheng, Y., et al. (2005). Accuracy of a wireless localization system for radiotherapy. *International Journal of Radiation Oncology*Biology*Physics , 61* (3), 933-937.

Bernier, J., Hall, E., & Giaccia, A. (2004). Radiation oncology: a century of achievemens. *Nature Reviews Cancer , 4*, 737-747.

Burke, B., Fallone, B., & Rathee, S. (2010). Radiation induced currents in MRI RF coils: application to linac/MRI integration. *Physics in Medicine and Biology , 55*, 735-746.

Burke, B., Ghila, A., Fallone, B. G., & Rathee, S. (2012). Radiation induced current in the RF coils of integrated linac-MR systems: The effect of buildup and magnetic field. *Medical Physics , 39*, 5004-5014.

Burke, B., Lamey, M., Rathee, S., Murray, B., & Fallone, B. (2009). Radio frequency noise from clinical linear accelerators. *Physics in Medicine and Biology , 54*, 2483-2492.

Chowdhury, N., Toth, R., Chappelow, J., Kim, S., Motwani, S., Punekar, S., et al. (2012). Concurrent segmentation of the prostate on MRI and CT via linked statistical shape models for radiotherapy planning. *Medical Physics , 39* (4), 2214-2228.

Dawson, L., & Jaffray, D. (2007). Advances in Image-Guided Radiation Therapy. *Journal of Clinical Oncology , 25* (8), 938-946.

Dempsey, J. (2006). An Image-guided device providing 4D cine MRI simultaneous to radiotherapy delivery. *Journal of Radiotherapy in Practice , 5* (3), 179.

Fallone, B., Murray, B., Rathee, S., Stanescu, T., Steciw, S., Vidakovic, S., et al. (2009). First MR images obtained during megavoltage photon irradiation from a prototype integrated linac-MR system. *Medical Physics , 36* (6), 2084-2088.

Hosiak, J., Sixel, K., Tirona, R., Cheung, P., & Pignol, J. (2004). Correlation of lung tumor motion with external surrogate indicators of respiration. *International Journal of Radiation Oncology*Biology*Physics , 60* (4), 1298-1306.

Hu, Y., Pehchenaya Green, O., Parikh, P., Olsen, J., & Mutic, S. (2012). TH-E-BRA-07: Initial Experience with the ViewRay system - Quality Assurance Testing of the Imaging Component. *Medical Physics , 39*, 4013.

ICRU50. (1993). *Prescribing, Recording and Reporting Photon Beam Therapy.* Bethesda: ICRU.

ICRU62. (1999). *Prescribing, Recording and Reporting Photon Beam Therapy.* Bethesda: ICRU.

Keyvanloo, A., Burke, B., Tadic, T., Warkentin, B., Kirkby, C., Rathee, S., et al. (2012). WE-E-BRB-06: Monte Carlo Calculations of the Skin Dose for Longitudinal Linac-MR System Using Realistic Three-Dimensional Magnetic Field Modeling. *Medical Physics , 39*, 3957.

Kim, S., & Suh, T.-S. (2006). Imaging in radiation therapy. *Nuclear Engineering and Technology , 38* (4), 327-342.

Kirkby, C., Murray, B., Rathee, S., & Fallone, B. (2010). Lung dosimetry in a linac-MRI radiotherapy unit with a longitudinal magnetic field. *Medical Physics , 37* (9), 4722-4732.

Kirkby, C., Stanescu, T., & Fallone, B. (2009). Magnetic field effects on the energy deposition spectra of MV photon radiation. *Physics in Medicine and Biology , 54*, 243-257.

Kirkby, C., Stanescu, T., Rathee, S., Carlone, M., Murray, B., & Fallone, B. (2008). Patient dosimetry for hybrid MRI-radiotherapy systems. *Medical Physics , 35* (3), 1019-1027.

Lagendijk, J., Raaymakers, B., Raaijmakers, A., Overweg, J., Brown, K., Kerkhof, E., et al. (2008). MRI/linac integration. *Radiotherapy and Oncology , 86*, 25-29.

Lamey, M., Burke, B., Blosser, E., Rathee, S., De Zanche, N., & Fallone, B. (2010a). Radio frequency shielding for a linac-MRI system. *Physics in Medicine and Biology , 55*, 995-1006.

Lamey, M., Rathee, S., Johnson, L., Carlone, M., Blosser, E., & Fallone, B. (2010c). Radio frequency noise from the modulator of a linac. *IEEE Transactions on Electromagnetic Compatibility , 52* (3), 530-536.

Lamey, M., Yun, J., Burke, B., Rathee, S., & Fallone, B. (2010b). Radio frequency noise from an MLC: a feasibility study of the use of an MLC for linac-MR systems. *Physics in Medicine and Biology , 55*, 981-994.

Langen, T., & Jones, D. (2001). Organ motion and its management. *International Journal of Radiation Oncology*Biology*Physics , 50* (1), 265-278.

Mackie, T., Balog, J., Ruchala, K., Shepard, D., Alrdridge, S., Fitchard, E., et al. (1999). Tomotherapy. *Seminars in Radiation Oncology , 9* (1), 108-117.

Mackie, T., Holmes, T., Swerdloff, S., Reckwerdt, P., Deasy, J., Yang, J., et al. (1993). Tomotherapy: A new concept for the delivery of dynamic conformal radiotherapy. *Medical Physics , 20* (6), 1709-1719.

Mutic, S. (2012). WE-A-BRA-02: First Commercial Hybrid MRI-IMRT System. *Medical Physics , 39*, 3934.

Nurushev, T., Kim, J., Hearshen, D., Pantelic, M., Kotys-Traughber, M., Elshaikh, M., et al. (2011). SU-E-J-78: Initial Experience with MR Simulation in Radiation Therapy Using An Open-Platform MR Scanner: Considerations for Routine Clinical Use. *Medical Physics* , 3460.

Raaijmakers, A. J., Raaymakers, B. W., & lagendijk, J. J. (2005). Integrating a MRI scanner with a 6 MV radiotherapy accelerator: dose increase at tissue-air interfaces in a lateral magnetic field due to returning electrons. *Physics in Medicine and Biology , 50*, 1363-1376.

Raaijmakers, A., Raaymakers, B., & Lagendijk, J. (2007b). Experimental verification of magnetic field dose effects for the MRI-accelerator. *Physics in Medicine and Biology , 52*, 4283-4291.

Raaijmakers, A., Raaymakers, B., van der Meer, S., & Lagendijk, J. (2007a). Integrating a MRI scanner with a 6MV radiotherapy accelerator: impact of the surface orientation on the entrance and exit dose due to the transverse magnetic field. *Phyics in Medicine and Biology* , 929-939.

Raaymakers, B., Lagendijk, J., Overweg, J., Kok, J., Raaijmakers, A., Kerkhof, E., et al. (2009). Integrating a 1.5 T MRI scanner with a 6 MV accelerator: proof of concept. *Physics in Medicine and Biology , 54* (12), N229-N237.

Raaymakers, B., Raaijmakers, A., Kotte, A., Jette, D., & Lagendijk, J. (2004). Integrating a MRI scanner with a 6MV radiotherapy accelerator: dose deposition in a transverse magnetic field. *Physics in Medicine and Biology , 49,* 4109-4118.

Rietzel, E., Rosenthal, S., Gierga, D., Willett, C., & Chen, G. (2004). Moving targets: detection and tracking of internal organ motion for treatment planning and patient set-up. *Radiotherapy & Oncology , 73,* S68-72.

Salvat, F., Fernandez-Varea, J., & Sempau, J. (2009). *PENELOPE-2008, A code system for Monte Carlo simulation of electron and photon transport.* Barcelona: OECD Nuclear Energy Agency.

Santos, D., St. Aubin, J., Fallone, B., & Steciw, S. (2012). Magnetic shielding investigation for a 6 MV in-line linac within the parallel configuration of a linac-MR system. *Medical Physics , 39* (2), 788-797.

St. Aubin, J., Santos, D., Steciw, S., & Fallone, B. (2010d). Effect of longitudinal magnetic fields on a simulated 6 MV linac. *Medical Physics , 37,* 4916-4923.

St. Aubin, J., Steciw, S., & Fallone, B. (2010b). An integrated 6 MV linear accelerator model from electron gun to dose in a water tank. *Medical Physics , 37,* 2279-2288.

St. Aubin, J., Steciw, S., & Fallone, B. (2010c). Effect of transverse magnetic fields on a simulated in-line 6 MV linac. *Physics in Medicine and Biology , 55,* 4861-4869.

St. Aubin, J., Steciw, S., & Fallone, B. (2010f). Magnetic decoupling of the linac in a low field bi-planar linac-MR system. *Medical Physics , 37*, 4755-4761.

St. Aubin, J., Steciw, S., & Fallone, B. (2010a). The design of a simulated in-line side-coupled 6 MV linear accelerator waveguide. *Medical Physics , 37*, 466-476.

St. Aubin, J., Steciw, S., & Fallone, B. (2010e). Waveguide detuning caused by transverse magnetic fields on a simulated in-line 6 MV linac. *Medical Physics , 37*, 4751-4754.

Stanescu, T., Jans, H.-S., Pervez, N., Stavrev, P., & Fallone, B. (2008). A study on the magnetic resonance imaging (MRI)-based radiation treatment planning of intracranial lesions. *Physics in Medicine and Biology , 53*, 3679-3693.

Tadic, T., & Fallone, B. (2010). Design and optimization of a novel bored biplanar permanent-magnet assembly for hybrid magnetic resonance imaging systems. *IEEE transactions on magnetics , 46* (12), 4052-4058.

Tadic, T., & Fallone, B. (2012). Design and optimization of superconducting MRI magnet systems with magnetic materials. *IEEE Transactions on Applied Superconductivity* , 1-11.

Tadic, T., & Fallone, B. (2011). Three-Dimensional nonaxisymmetric pole piece shape optimization for biplanar. *IEEE Transactions on Magnetics , 47* (1), 231-238.

Van Dyke, J. (1999). *The modern technology of radiation oncology: A compendium for medical physicists and radiation oncologists.* Madison: Medical Physics Publishing.

van Herk, M. (2004). Errors and margins in radiotherapy. *Seminars in radiation oncology , 14* (1), 52-54.

Vedam, S., Kini, V., Keall, P., Ramakrishnan, V., Mostafavi, H., & Mohan, R. (2003). Quantifying the predictability of diaphram motion during respiration with a non-invasive external marker. *Medical Physics , 30* (4), 505-513.

Verellen, D., De Ridder, M., Linthout, N., Tournel, K., Soete, G., & Storme, G. (2007). Innovations in image-guided radiotherapy. *Nature Reviews Cancer , 7*, 949-960.

Wachowicz, K., Stanescu, T., Thomas, S., & Fallone, B. (2010). Implications of tissue magnetic susceptibility-related distortion on the rotating magnet in an MR-linac design. *Medical Physics , 37* (4), 1714-1721.

Webb, S. (2006). Motion effects in (intensity modulated) radiation therapy: a review. *Physics in Medicine and Biology , 51*, R403-R425.

Yun, J., St. Aubin, J., Rathee, S., & Fallone, B. (2010). Brushed permanent magnet DC MLC motor operation in an external magnetic field. *Medical Physics , 37* (5), 2131-2134.

Yun, J., Yip, E., Wachowicz, K., Rathee, S., Mackenzie, M., Robinson, D., et al. (2012). Evaluation of a lung tumor autocontouring algorithm for intrafractional tumor tracking using low-field MRI: A Phantom Study. *Medical Physics , 39* (3), 1481-1494.

# 2 Theory

As mentioned in § 1.4, one of the consequences of integrating a linear accelerator with an MRI system is that the RF coils used by the MRI are exposed to the pulsed radiation of the linac. When high energy (MeV) photons impinge upon thin metals, such as the copper windings used as the conductors in MRI RF coils, high energy electrons are produced through Compton interactions and are ejected from the conductor. This efflux of electrons produces a charge imbalance in the conductor, making it positively charged. If the metal conductor is part of an electrical circuit, as is the case for the RF coils, then electrons will flow from the circuit into the coil to neutralize the charge imbalance. This leads to a current flowing from the coil into the circuit. This current is known as radiation induced current; it is also called Compton current because it is produced via Compton scattering and has been reported on by many authors.

Meyer *et al* reported in 1956 on the RIC seen in polyethylene and Teflon upon exposure to X-rays from a 2 MeV Van de Graaff generator and a $^{60}$Co beam [Meyer, et al., 1956]. Johns *et al.* (1958) reported the RIC due to the $^{60}$Co beam in parallel plate ionization chambers providing RIC as the basis of the polarity effect observed in these chambers [Johns, et al., 1958]. Several authors have published reports on RIC in varying materials when exposed to pulsed radiation [Degenhart, et al., 1961; Abdel-Rahman, et al., 2006]; which are of particular relevance to this work.

Degenhart et al. were one of the first groups to examine the effects of pulsed nuclear radiation, in particular the transient effects. They used the pulsed

radiation from a uranium reactor and exposed several electrical components to this radiation. These included coaxial cables, resistors, sensistors, capacitors, rectifiers and magnetic ferrites. They observed transient, radiation induced effects in all of the tested materials and permanent changes in the semiconductor materials. They were one of the first groups to suggest that electrical circuit components could experience transient malfunction during pulsed radiation [Degenhart, et al., 1961].

Abdel-Rahman et al. observed RIC in parallel plate ionization chambers when exposed to the pulsed radiation of clinical linear accelerators, both electrons and photons. They used a phantom embedded extrapolation chamber, which allows them to vary the separation between the plates of the ion chamber. They were able to discern that the polarity effect observed in ionization chambers can be divided into two categories: (1) a voltage dependent effect that produces a signal difference between two polarity readings which varies with the polarizing voltage (2) a voltage-independent polarity effect for which the difference between two polarity readings is independent of the polarizing voltage [Abdel-Rahman, et al., 2006]. The voltage-independent effect is caused by RIC in the parallel-plate chamber, with the main source being the collecting electrode. They also found that by placing their chamber at depth (i.e. adding buildup) they were able to reduce the RIC until it was near zero at the depth of radiological maximum dose, 1.5 cm for 6 MV photons and 3.0 cm for 18 MV photons [Abdel-Rahman, et al., 2006].

For this work RIC refers to the current that is induced in the conductive windings of MRI RF coils when exposed to the pulsed radiation of a linac. This work will deal with the measurement of RIC in pulsed radiation, the Monte Carlo simulation of RIC and imaging with the prototype linac-MR system to quantify the effect that RIC has on MR image quality. The theory presented in this chapter will be split into three sections: radiation effects, Monte Carlo simulations and MRI basic concepts. These three sections will provide the foundation with which the rest of this work can be understood.

## 2.1 Radiation effects

In radiological physics there are several important mechanisms of photon interactions with matter. These include but are not limited to: photoelectric absorption, coherent and incoherent (Compton) scattering, pair and triplet production. Each of these interaction mechanisms has a finite interaction cross-section and the total interaction cross section of a photon is simply the sum of the individual cross-sections. The detailed description of all the processes and their interaction cross-sections is beyond the scope of this work, as this work concerns itself with radiation induced currents, not dose calculation. Previous work has shown that radiation induced currents are largely produced via Compton interactions [Johns, et al., 1958; Meyer, et al., 1956], but both photoelectric and pair production events can occur at the energies used in this work and produce electrons capable of adding to the RIC signal. These three processes will be explained in more detail. The energies at which each interaction is dominant are

shown schematically in Figure 2.1. This work uses the 6 MV photon beam from a clinical linear accelerator.

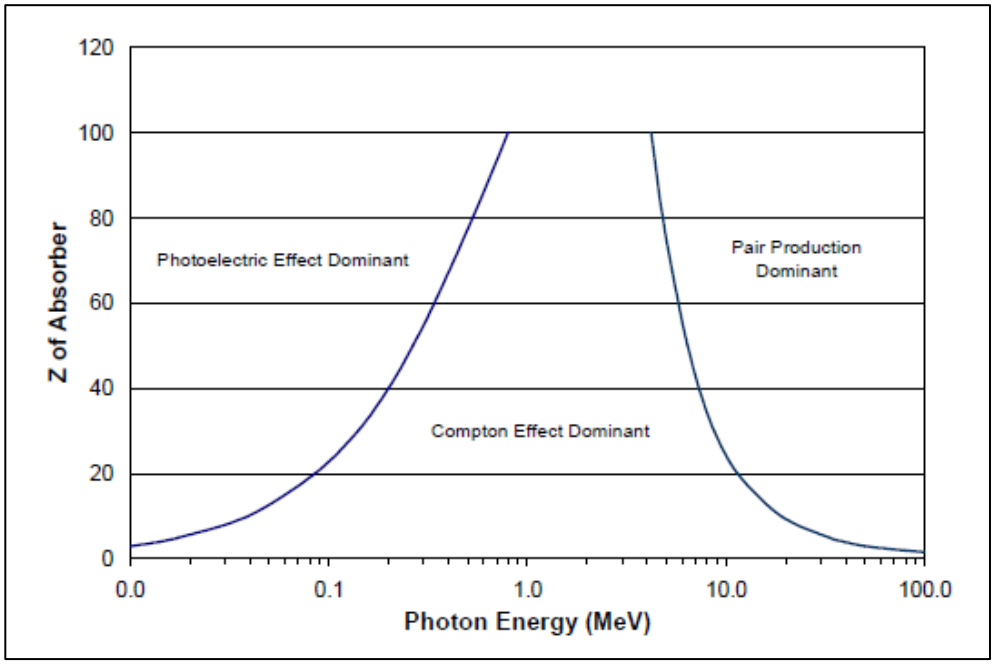


**Figure 2.1- Energy dependence of three dominant photon interactions at clinical photon energies. The figure shows the relationship with atomic number (Z) as well as energy. [data taken from NIST database]**

### 2.1.1 Photoelectric absorption

In a photoelectric absorption event, shown in Figure 2.2, an incoming photon with energy *hv* interacts with an atom as a whole and is absorbed. An electron is then ejected from one of the atomic shells with binding energy $E_b$. The kinetic energy of this ejected electron is given by:

$$T = hv - E_b \qquad \textbf{(2.1)}$$

This type of event cannot occur with a free electron as the atom is needed in order to conserve momentum.

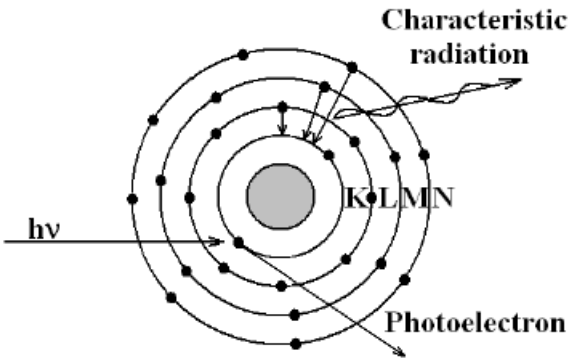


**Figure 2.2 - Schematic representation of a photoelectric absorption. The incoming photon with energy *hv* interacts with the atom and ejects a photoelectron.**

The cross section for photoelectric absorption, in general, decreases with increasing photon energy for a given material; however, there are a series of discontinuities which represent the binding energies of the electrons of the various atomic shells. An example of this is seen in Figure 2.3, which shows the photoelectric cross-section for lead as a function of photon energy. These discontinuities show that a photoelectric absorption event is most likely to occur when the incident photon energy is the same as the binding energy of the electron. The photoelectric cross section has the general form [Nahum, 2007]:

$$\sigma_{ph} \cong \frac{kZ^4}{(hv)^3} \qquad \textbf{(2.2)}$$

Equation (2.2) shows that the cross-section increases with the 4$^{th}$ power of atomic number (Z) and decreases with the 3$^{rd}$ power of photon energy. Thus this process is dominant at lower photon energies, particularly in high Z materials.

Once a photoelectron is ejected from an atom, there is a vacancy left in its shell which is subsequently filled with an electron from an outer shell. The energy is conserved between the two shells involved through the emission of either a characteristic photon or an Auger electron. The energy of the characteristic photon

is the difference between the binding energy of the two shells. The energy of the Auger electron is equal to the energy released in the initial transition minus the binding energy of the Auger electron.

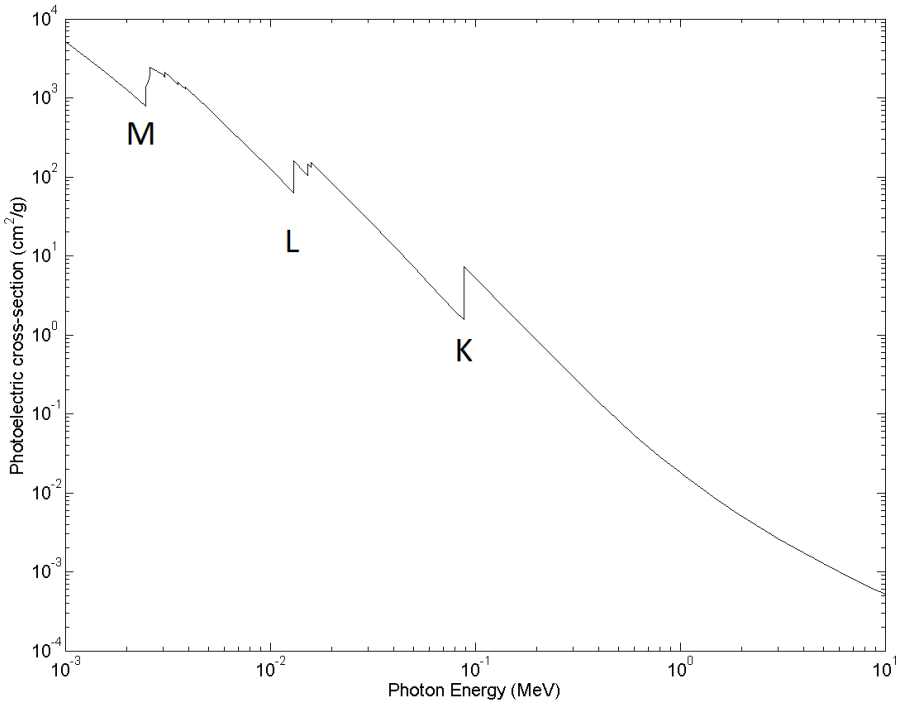


**Figure 2.3 - The photoelectric absorption cross-section for lead shown in $cm^2/g$ as a function of photon energy in MeV. Data taken from NIST's XCOM program. The discontinuities at the binding energies of the K, L and M atomic shells can be seen.**

### 2.1.2 Compton scattering

The mechanism of Compton scattering is seen schematically in Figure 2.4. In a photon scattering event, of any kind, the incident photon will change direction after the interaction. If some of the energy of the incident photon is lost, the scattering is called Compton or incoherent scattering. Alternatively, if the incident photon does not lose energy then the event is called Rayleigh or coherent scattering.

During an incoherent scattering event the incident photon with energy *hν* transfers part of its energy to an electron. The scattering photon then leaves the interaction with new energy, *hν'*, at angle θ relative to the incident photon direction, while the scattered electron has energy E and direction ϕ relative to the original photon direction.

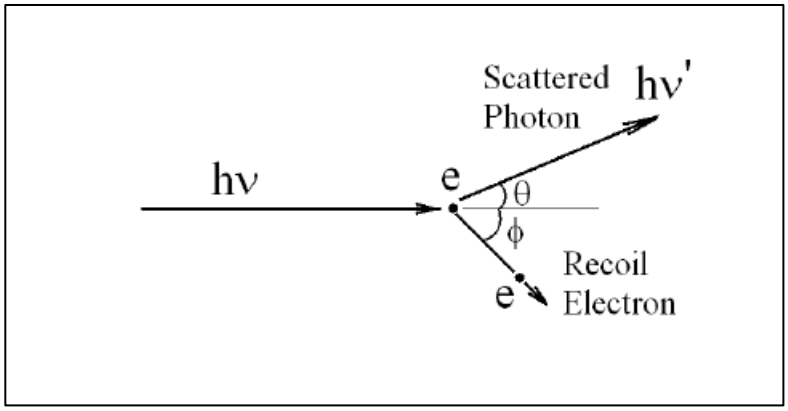


**Figure 2.4 - Schematic of Compton scattering process showing the incident high energy photon, scattering electron, scattered photon and recoil electron.**

The energy of the scattered photon can be expressed as:

$$h\nu' = \frac{h\nu}{1 + \alpha(1 - \cos\theta)} \qquad \textbf{(2.3)}$$

where $\alpha = h\nu/(m_0c^2)$, c is the speed of light and $m_0$ is the electron rest mass. Equation (2.3) is called the Compton equation [Johns, et al., 1983; Nahum, 2007]. The energy and direction of the scattered electron are determined by using conservation of both energy and momentum:

$$E = h\nu - h\nu' = h\nu\left(\frac{\alpha(1 - \cos\theta)}{1 + \alpha(1 - \cos\theta)}\right) \qquad \textbf{(2.4)}$$

Equation (2.4) shows that maximum energy is transferred to the electron when the photon scattering angle is 180°, signifying a 'direct hit' where the

electron is scattered straight forward and the photon is scattered straight back. The electron energy is this case becomes:

$$E_{max} = hv\frac{2\alpha}{1+2\alpha} \tag{2.5}$$

The scattered photon's energy is minimum, given as follows:

$$hv'_{min} = hv\frac{1}{1+2\alpha} \tag{2.6}$$

On the other hand when the incident photon does not change direction at all after scattering, signifying a grazing hit, no energy is imparted to the electron, as seen by the numerator of (2.4) becoming zero, while the photon retains all of its energy [Johns, et al., 1983; Nahum, 2007]. In the case of RIC only the non-zero electron scattering interactions are of interest since only electrons of finite kinetic energy have a finite probability of leaving the conductive material of the RF coil

The Compton cross-section depends on the angle of the scattered photon through the Klein-Nishina formulation [Johns, et al., 1983] and the integral (over all angles) Compton cross-section has the following complicated form:

$$\sigma_{Com} = 2\pi r_0^2\left\{\left(\frac{1+\alpha}{\alpha^2}\right)\left(\frac{2(1+\alpha)}{1+2\alpha} - \frac{\ln(1+2\alpha)}{\alpha}\right) + \frac{\ln(1+2\alpha)}{2\alpha} - \frac{1+3\alpha}{(1+2\alpha)^2}\right\} \tag{2.7}$$

where $r_0$ is the classical electron radius $\approx 2.81794\text{x}10^{-15}$m. If the electrons involved in the Compton scattering processes are assumed to be unbound to the atomic nucleus, the integral Compton cross-section is independent of the atomic number of the material. This approximation is usually accurate except for very low photon energies, when the binding energy becomes comparable to the energy

of the photon. The Compton cross section generally decreases slowly with increasing photon energy, but at the energies used in radiotherapy it is the dominant interaction mechanism in tissue.

### 2.1.3 Pair Production

In the pair production interaction, illustrated in Figure 2.5, the incident photon with energy *hv* is absorbed by the electric field of the nucleus. In order to conserve charge and momentum, an electron-positron pair is created. The sum of the kinetic energies of the electron and positron is equal to the energy of the incident photon reduced by the rest mass energy of the two charged particles as given below:

$$T^- + T^+ = hv - 2m_0c^2 \quad \textbf{(2.8)}$$

Where $T^-$ and $T^+$ are the kinetic energies of the electron and positron, respectively, and $m_0c^2$ is the rest energy of the electron. The incident photon must have energy greater than $2m_0c^2$ for the pair production process to occur. While, in theory, the positron and electron can share the excess photon energy in any combination, the probability for either particle absorbing most of the energy is small [Nahum, 2007]. In general, the likelihood of equal distribution of the excess energy between the electron-positron pair is the largest. The probability of pair production is zero below the threshold energy, and then increases rapidly with energy. In terms of the material dependence, the pair production cross-section is directly proportional to the square of the atomic number, i.e.:

$$_a\sigma_{Pair} \propto Z^2 \quad \textbf{(2.9)}$$

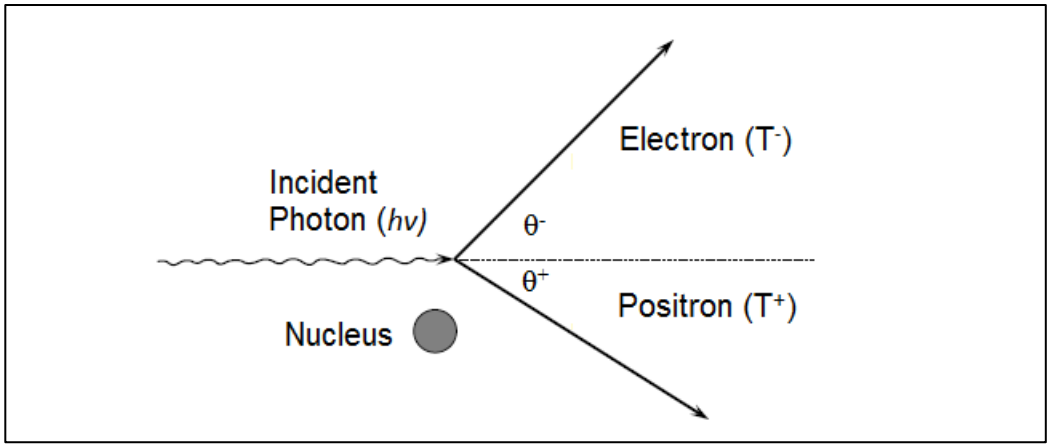


**Figure 2.5 - Schematic representation of pair production showing the incident photon and the electron-positron pair created with kinetic energies T and T.**

Since pair production produces an electron, along with the positron, it can contribute to RIC.

### 2.1.4 Charged particle equilibrium

While this work does not deal explicitly with radiation dose measurement, the following two definitions need to be clarified to lay the foundation for the discussion of charged particle equilibrium (CPE). The concept of CPE is necessary to understand the work discussed in Chapter 4, which involves the addition of buildup material to RF coil conductors.

*Kerma* – stands for Kinetic Energy Released per Mass in the medium and represents the sum of all kinetic energies imparted to charged, ionizing particles by uncharged ionizing particles. Thus in the interactions involving photons and electrons, it is energy imparted to electrons by the photons. Macroscopically, it represents the kinetic energy transferred ($dE_{tr}$) to a volume element of mass *dm* [ICRU85, 2011]:

$$K = \frac{d\bar{E}_{tr}}{dm} = \Phi \cdot \left(\frac{\mu}{\rho}\right) \cdot \bar{E}_{tr} \qquad \textbf{(2.10)}$$

Where Φ is the photon fluence and $\frac{\mu}{\rho}$ is the mass attenuation coefficient for the medium. The product of these two terms gives the number of photon interactions that take place per unit mass.

*Absorbed Dose* – represents the amount of energy deposited ($E_{ab}$) in a volume element of mass *dm* by the ionizing radiation [ICRU85, 2011]:

$$D = \frac{d\bar{E}_{ab}}{dm} \qquad \textbf{(2.11)}$$

This differs from *Kerma*, which accounts for all of the kinetic energy given to the charged particles by interacting photons inside the volume of interest. If the charged particles become energetic enough to leave the volume of interest, then not all of the energy imparted to the charged particles contributes to the absorbed dose in the volume of interest. While the absorbed dose accounts for the total energy deposited in the volume of interest by the charged particles, the charged particles moving through the volume of interest need not have been set into motion within the volume of interest. Thus there is no simple relationship between the absorbed dose and *Kerma*, in general, except in the regions of matter where CPE exists.

CPE can be defined, in the broadest sense, as the following: CPE is said to exist in an irradiated volume of interest if the number of charged particles, of a specified type, entering this volume is equal to the number of similarly charged particles leaving the volume. In a region of CPE, no net change in charge occurs. For the purpose of this work we will restrict ourselves to equilibrium of electrons.

In the range of radiotherapy photon energies, the probability of pair and triplet production is significantly smaller than the probability of Compton scattering (for instance at 2 MeV, nominally the mean energy of a 6 MV clinical beam, the Compton scattering cross section is 26 and 63 times larger than the pair production cross section in copper and aluminum, respectively) thus the positrons are produced so infrequently that they can safely be disregarded. This type of CPE can also be called electronic equilibrium.

Figure 2.6 has a simple schematic of a hypothetical scenario to explain the CPE process. In each of the voxels A through H in Figure 2.6b, an electron of identical energy, travelling in a straight forward direction in assumed to be created. CPE does not exist in voxel A because an electron leaves this voxel but there is no electron stopping in the voxel to replace it. The same is true of voxel B; here the electron originating in A enters and leaves the voxel, yielding no change and the electron track started in B also leaves the volume with no replacement. In this scenario, the first voxel in which CPE exists is D, as it has an electron, A, coming to rest in its volume to balance the charge lost by its own track, D. This hypothetical scenario is an extreme simplification to illustrate the process of CPE, it assumes that the photon beam has the same fluence in all the voxels and assumes the same number of interactions occur in each voxel. Neither of these assumptions are true in a realistic case.

The dots at the beginning of the tracks in Figure 2.6b indicate the electron being set into motion. The hashed marks along the lines in Figure 2.6b represent energy (dose) depositing events along the electron tracks, the more hashes in a

voxel, the higher the dose in that voxel, the angle of the hashed lines is simply used to differentiate one voxel from the voxels adjacent to it. This is shown visually in Figure 2.6a. The vertical bars indicate the end of the electron track and the region in which that electron is depositing its energy. The dose increases from its minimum at the surface of A, to an approximately constant value at and beyond D. The region from A-D is called the buildup region..

Figure 2.6a also shows that CPE begins to exist when the absorbed dose and *Kerma* are equal. Looking to Figure 2.6c it is apparent that absorbed dose and *Kerma* are not exactly equal when beam attenuation is taken into account. At any depth beyond the buildup region, the number of electrons coming to rest at that depth is slightly higher than the number of electrons being set into motion in that volume, due to beam attenuation. Thus the absorbed dose will always be slightly larger than the kerma. However, for this work the approximations of Figure 2.6a is sufficient to understand the build up method used to remove RIC, which will be discussed later in Chapter 4.

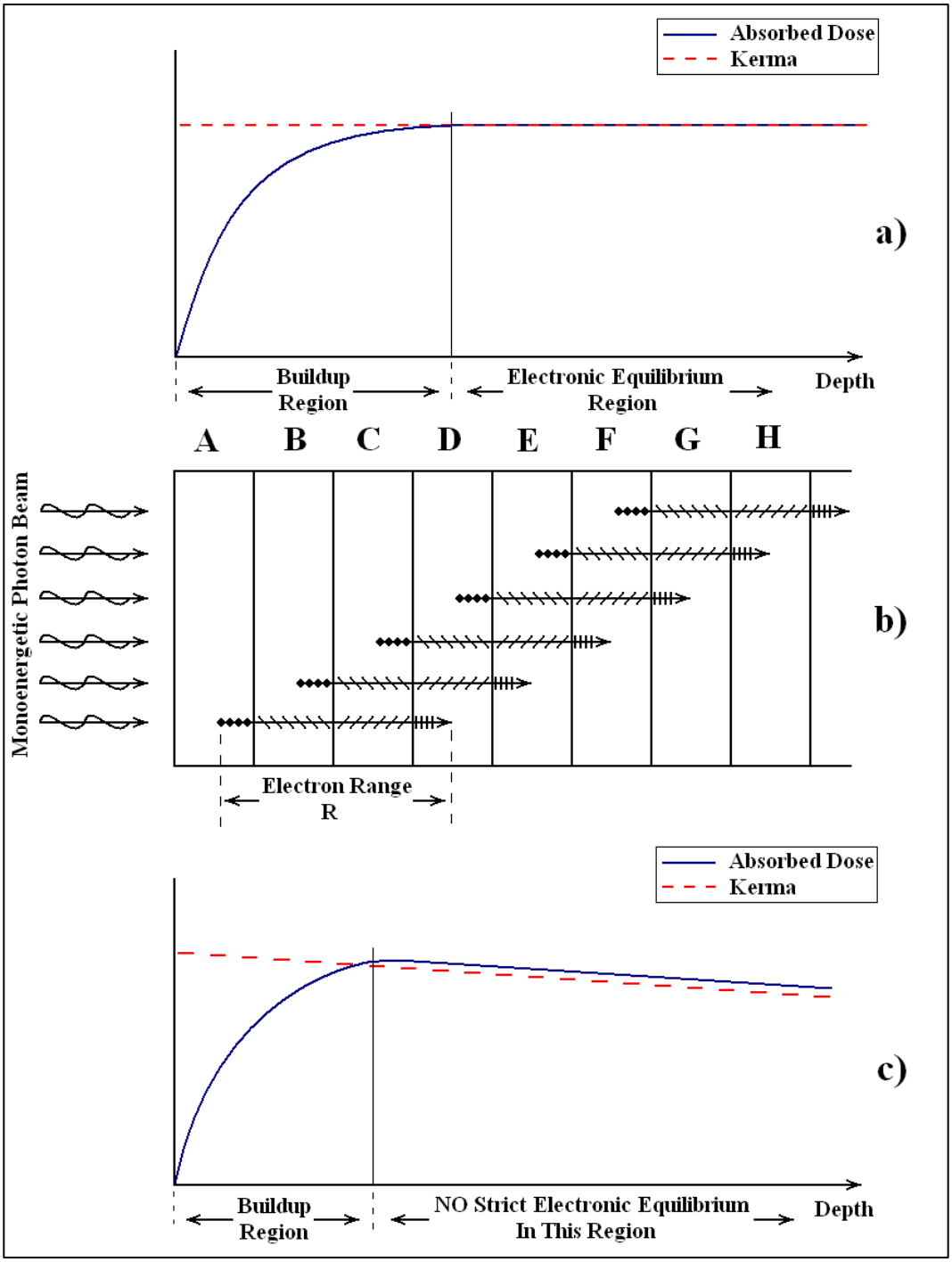


**Figure 2.6 - Schematic representation of electron ranges in medium depicting how charged particle equilibrium occurs and the relationship between *Kerma* and absorbed dose.**

## *2.2 Monte Carlo simulations:*

### 2.2.1 Basic Concepts

In general, Monte Carlo (MC) describes a class of numerical methods based on the use of random numbers, used to sample known probability distribution functions [Salvat, et al., 2009]. Applied to radiotherapy it provides a statistical model which yields the same information as the solution to the Boltzmann transport equation, without solving the Boltmann equation directly, that accurately describes and calculates the photon and electron transport through medium by considering their interactions with the atoms [Nahum, 2007]. Monte Carlo methods for particle transport are statistical methods which simulate a large number of particle tracks, called histories, and aggregate the quantities of interest, such as absorbed dose, particle fluence and net charge, to supply a statistical representation of a radiation process along with an associated statistical error. The particle history generally involves a sequence of free flights that end with an interaction where the particle changes direction, loses energy and, sometimes, produces secondary particles with their own tracks, which are also simulated.

#### 2.2.1.1 Sampling methods

In order to accurately model the Boltzmann equation using Monte Carlo methods, an interaction model must be developed. This model needs to accurately describe a set of differential cross sections (DCS) for all the relevant particle interactions. These DCS are then used to produce probability distribution functions (PDF) to be used for sampling. One of the most common methods used for sampling PDFs

in Monte Carlo is the inverse transform method. This method first requires a cumulative distribution function (CDF), calculated as:

$$CDF(x) = \int_{x_{min}}^{x} PDF\,(x')dx' \tag{2.12}$$

Where $x$ is a continuous random variable with values from $x_{min}$ to $x_{max}$. The CDF($x$) will be a non-decreasing function which will vary from 0 at $x_{min}$ to 1 at $x_{max}$. Then we introduce the transformation:

$$\xi = CDF(x) \tag{2.13}$$

Therefore ξ is a random variable in the interval [0, 1]. For a given value of ξ, the parameter x is calculated by taking the inverse of the CDF.

$$x = CDF^{-1}(\xi) \tag{2.14}$$

By using the random variable ξ, distributed randomly in the interval [0, 1], to generate values of $x$ in this manner, Eq. (2.14) assures that $x$ is randomly distributed according to PDF($x$). For complex PDFs where the inversion of the CDF using analytical methods is not feasible, the numerical inversion of the sampled CDF is generally performed [Nahum, 2007].

### 2.2.1.2 Radiation transport

Photon histories follow a set of rules based on the physical interaction processes in detail and generally will have the following steps: (1) Choose the starting parameters (position, energy, direction) by sampling the initially provided distribution of these parameters; (2) using the initial parameters of the photon and the cross-section particular to photon energy and the medium of interest, sample the mean free path distribution to calculate distance to first interaction and

transport photon to this location; (3) decide on the type of interaction based on their relative probabilities; (4) sample the appropriate cross-sections to decide the parameters (direction, energy, charge etc.) for newly generated particles and place them in secondary stack; (5) transport the scattered photon until it either reaches the cut-off energy or leaves the geometry; (6) transport secondary particles; (7) score the quantities requested for the region of interest; (8) repeat 1-7 until the required statistical accuracy is reached [Nahum, 2007].

Electron transport is managed by using a mixed condensed history method, as detailed simulation of all electrons generated would require extremely long simulation time per photon history, along with very large computational requirements. The assumption used by condensed history methods is that while electrons have a large number of interactions, relatively few of these interactions result in significant energy exchange or directional changes. Electron interactions with energy loss or directional change above threshold amounts are simulated explicitly, while all events below these thresholds are simulated in a condensed manner: (1) A hard event involving a change in energy and/or direction above the pre-chosen threshold is explicitly simulated. The energy and direction of the electron is calculated and it is moved a distance based on the random sampling of the mean free path PDF; (2) a single random-hinge event is simulated to account for the cumulative directional changes and energy losses due to the soft interactions occurring between the previous hard event and the next one. The electron changes its direction of movement according the sampling of the multiple

scattering distribution; (3) the electron is moved the rest of the distance to next hard event with its new direction.

### 2.2.2 PENELOPE

A portion of this work involves using Monte Carlo methods to simulate RIC using the Monte Carlo simulation program PENELOPE [Salvat, et al., 2009]. PENELOPE is a Monte Carlo simulation program capable of simulating coupled particle transport in various materials and in complex geometries described by the user. The program models radiation transport in media by using known interaction cross sections and statistical methods to track the paths and energy depositing events of individual particles passing through the media. The scattering model used contains differential cross sections to model all relevant interactions. The cross-sections of the scattering events are contained as either tabular data or analytical cross-section functions, depending on the interaction. Photons are simulated in a purely detailed manner by using all dominant processes including: Rayleigh scattering; photoelectric absorption; Compton scattering; and pair/triplet production. Electron and positrons are simulated using a mixed simulation approach. 'Hard' events are simulated in detail and 'soft' are simulated as multiple scattering events (i.e. condensed history). A hard event is an interaction where the particle loses more energy that a pre-defined cut-off. The simulated electron (positron) interactions are: elastic scattering, inelastic collisions, bremsstrahlung emission and positron annihilation.

The number of histories (n), in general, will determine the statistical accuracy and computational time of the simulations. Generally, the statistical

accuracy improves and computational requirements increase with increasing particle histories. Therefore, the number of histories is a compromise between the required statistical accuracy and the computational time. PENELOPE was used in these experiments in favour of other MC codes (e.g. EGSnrc) because it has excellent modelling of transport in the range of a few hundred eV to ~ 1GeV. It has a built in module which allows for the straightforward implementation of magnetic fields, and it is simple to program and use. The accurate modelling in the presence of the magnetic field was the most important factor in choosing to use PENELOPE. The module penEasy2010 was used in conjunction with PENELOPE since it allows the user to create simple steering programs and take advantage of some built-in tally functions. PenEasy simulations are controlled through the following four user specified parameters: $C_1$ defining the average angular deflection produced by multiple elastic scattering along a path length equal to the mean free path between consecutive hard elastic events, $C_2$ defining the maximum average fractional energy loss between consecutive hard elastic events, $W_{cc}$ representing the cutoff energy loss for hard inelastic collisions below this level energy soft collisions are simulated, and $W_{cr}$ the cutoff energy loss for hard bremsstrahlung emission.

## *2.3 Magnetic Resonance Imaging*

Since magnetic resonance imaging is an integral part of this work, a brief discussion of nuclear magnetic resonance (NMR) concepts is provided here.

### 2.3.1 Spin Physics

Many nuclei possess spin angular momentum, J, which obey the following quantum mechanical rules: (1) if both the number of protons and the number of neutrons are even, the spin is zero; (2) if the sum of protons and neutrons is odd, the nucleus has a half-integer spin. (1/2, 3/2, etc.); (3) if the number of protons and the number of neutrons are both odd, then the nucleus has an integer spin (1, 2, etc.). Nuclei which possess spin angular momentum also possess a magnetic moment, μ, directed along the axis of rotation and this is the key property of nuclei that manifests in the magnetic resonance experiment. The magnetic moment is related to the spin angular momentum through the gyromagnetic ratio, γ.

$$\vec{\mu} = \gamma \vec{J} \qquad \textbf{(2.15)}$$

The gyromagnetic ratio is a property of the nucleus and is quite varied, for instance the $^{1}H$ nucleus has a gyromagnetic ratio of 42.57 MHz/T, while $^{23}Na$ has a gyromagnetic ratio of 11.26 MHz/T. Due to its large gyromagnetic ratio and natural abundance, the $^{1}H$ is the nucleus predominantly used in MRI.

### 2.3.2 Torque and Precession

In general, the magnetic moments contained in a substance are oriented in random directions, with no preferred orientation. However, once an external magnetic field is applied, also called the main field $B_0$, the spins will experience a torque which attempts to align the direction of the magnetic moment with the direction of the applied field (Figure 2.7). Figure 2.7 is a simplification, in reality the spins will not be aligned perfectly with the main field, but will be slightly off

axis due to quantum mechanical reasons discussed below. The torque, $\tau$, experienced by the spins is given as follows:

$$\vec{\boldsymbol{\tau}} = \vec{\boldsymbol{\mu}} \times \vec{\mathbf{B}}_{\mathbf{0}} \tag{2.16}$$

And from the definition of torque:

$$\vec{\boldsymbol{\tau}} = \frac{\mathbf{d}\vec{\mathbf{J}}}{\mathbf{dt}} = \frac{\mathbf{1}}{\boldsymbol{\gamma}}\frac{\mathbf{d}\vec{\boldsymbol{\mu}}}{\mathbf{dt}} \tag{2.17}$$

Combining (2.16) and (2.17) yields:

$$\frac{d\vec{\mu}}{dt} = \gamma\left(\vec{\mu} \times \vec{B}_0\right) \tag{2.18}$$

The applied torque is perpendicular to both the magnetic moment and the applied field. The angle between the magnetic moment and the external magnetic field is constant and non-zero, resulting in precession of spins about $B_0$. The solution to equation (2.18) describes a precession in which the magnetic moment vector rotates around the applied magnetic field with frequency

$$\vec{\omega}_0 = \gamma\vec{B}_0 \tag{2.19}$$

This equation is called the Larmor equation, and $\omega_o$ is the Larmor frequency.

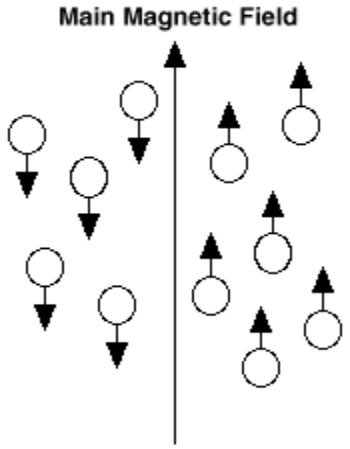


**Figure 2.7 - Magnetic Moments in an applied magnetic field. The moments will align parallel and anti-parallel to the main field direction.**

### 2.3.3 Quantum Mechanical Treatment of Magnetic Moment

The description of the magnetic moment thus far has been classical, and while useful, in order to understand many of the underpinnings of magnetic resonance we must look to Quantum Mechanics for a more complete description. We can first express the magnetic moment, $\vec{\mu}$, as

$$\vec{\mu} = \gamma\vec{J} = \gamma\hbar\vec{I} \quad \textbf{(2.20)}$$

where γ is the gyromagnetic ratio, ħ is Planck's constant divided by 2π, I is the spin operator, and ħI is the angular momentum of the nucleus [Wilman, et al., 2006]. In quantum mechanics the angular momentum has only discrete values in the z direction (z is defined as the direction of the main field $B_0$)

$$J_z = m\hbar \quad \textbf{(2.21)}$$

Where m = I, I-1, ..., -(I-1), -I yielding 2m+1 possible values for $I_z$. The spin quantum number I can have many different values but, in order to satisfy the quantization of the z component these values must be integer multiples of ½. In the presence of the applied magnetic field, the Hamiltonian of the system becomes

$$H = -\vec{\mu} \cdot \vec{B}_0 \quad \textbf{(2.22)}$$

In MRI it is usual for the $B_0$ field to be directed along the z axis, so the energy can be rewritten as

$$H = -\vec{\mu} \cdot \vec{B}_0 = -\gamma B_0 J_z = -\gamma m\hbar B_0 \quad \textbf{(2.23)}$$

For spin ½ nuclei, such as $^{1}H$ and $^{31}P$, there are 2 possible energy eigen-states, and hence two values for m,

$$E_{+} = -\frac{\gamma\hbar B_0}{2}, \qquad for\ m = \frac{1}{2}\ (spin\ up) \tag{2.24}$$

$$E_{-} = \frac{\gamma\hbar B_0}{2}, \qquad for\ m = -\frac{1}{2}\ (spin\ down) \tag{2.25}$$

The spin up nuclei will be aligned parallel to the applied field while the spin down nuclei will be aligned anti-parallel. The energy difference between the two states, $\gamma\hbar B_o$, indicates that there should be a difference in distribution between these two states when an external magnetic field is applied. Since the spin up state has a lower energy there will be an excess of spins in this state. Transitions can be induced between the two states by applying a radio frequency pulse that is equal to the energy difference between the two states, $\gamma\hbar B_o$. The energy of this pulse will be $\hbar\omega_0$, indicating the pulse must be delivered at the Larmor frequency as given by (2.19).

### 2.3.4 Statistical Thermodynamics and Magnetization

In 2.3.3 it was stated that, intuitively, there should be a difference in distribution between the two spin states because of the energy difference between them. The ratio of spins in these two states is governed by Maxwell-Boltzmann statistics,

$$\frac{N_{down}}{N_{up}} = e^{-\frac{\Delta E}{kT}} \tag{2.26}$$

Where $N_{down}$ and $N_{up}$ represent the number of spins in the spin down and spin up state, respectively, $\Delta E$ is the energy difference between the two spin states, $k$ is the Boltzmann constant and $T$ is temperature. This slight excess in spins in the lower energy state gives a bulk magnetization, $M_o$, which is defined as

$$\vec{M}_0 = n_i\langle\vec{\mu}\rangle \tag{2.27}$$

Where $n_i$ is the concentration of nuclei [Kuperman, 2000] and ‹μ› is the average magnetic moment. The component of μ along z will be either parallel or anti-parallel to the main magnetic field, and from (2.26) there will be an excess of spins in the parallel direction giving us a component of $M_o$ along the z axis. However, in the x-y plane, also called the transverse plane, the direction of the components of μ will be random and so when averaged, will be zero. Hence, the bulk magnetization will be in the z direction and is often referred to as longitudinal magnetization.

$$M_0 = M_z,\ M_x = M_y = 0$$

Now if (2.27) is evaluated using the Boltzmann probability, the result is the magnetization for spin ½ nuclei, $M_o$ [Wilman, et al., 2006]:

$$M_0 = \frac{N\gamma^2 \hbar B_0}{4kT} \qquad \textbf{(2.28)}$$

### 2.3.5 Radio frequency pulse and the rotating frame

The bulk magnetization, that is the basis for the magnetic resonance signal, is oriented in the direction of the applied main magnetic field (z direction). Because, as mentioned in § 2.3.4, the transverse components average to zero in the steady state, there is no measurable signal being produced by the sample. Therefore, to acquire a signal, the longitudinal magnetization, or at least part of it, must be flipped into the transverse plane. To accomplish this, an RF pulse that produces a time varying magnetic field, perpendicular to the main magnetic field, is applied at the Larmor frequency. This is accomplished using an RF coil with its axis

perpendicular to the $B_o$ field. The small perturbing field created by this RF pulse is called the $B_1$ field.

The effects of this pulse can be examined both classically and quantum mechanically. In the quantum mechanical view, the RF pulse at the Larmor frequency will cause spins in the lower state to jump to the higher energy state. The total longitudinal magnetization is thus reduced since the sample now has more spins aligned anti-parallel. This pulse will also cause a transient state of phase coherence in the x-y plane which provides a net transverse component of magnetization [Wilman, et al., 2006].

Classically, the effects of the RF pulse can be treated as a rotation due to the torque exerted by $M \times B_1$. To illustrate this point it is helpful to switch from the stationary laboratory frame, (x, y, z) to a frame which is rotating about the z axis at the Larmor frequency, (x',y',z). This formalism allows the treatment of both the bulk magnetization and the applied RF pulse as stationary vectors. It is therefore easier to see how the RF pulse will exert a torque on the bulk magnetization. For example, a pulse applied along the x' direction will exert a torque on the magnetization that will cause it to be rotated into the y' direction. The amount of magnetization which is 'flipped' into the transverse plane depends on the flip angle, α, which is defined as:

$$\alpha = \gamma B_1 t \qquad \textbf{(2.29)}$$

Where $t$ is the duration of the RF pulse. A 90 degree flip angle will rotate all of the longitudinal magnetization into the transverse plane, thus producing the most transverse magnetization.

### 2.3.6 Relaxation

Once rotated into the transverse plane, the magnetization vector will begin to precess around the z axis at the Larmor frequency. This new state is not the equilibrium state so, naturally, the magnetization will slowly recover to the equilibrium state, i.e. along the z axis. For this to occur we need the transverse magnetization to decay and the longitudinal magnetization to recover. These two processes are governed by the Bloch equations, named after Felix Bloch who was one of the co-developers of NMR, which are as follows [Wilman, et al., 2006; Kuperman, 2000]:

$$\frac{dM_z}{dt} = \frac{(M_0 - M_z)}{T_1} \tag{2.30}$$

$$\frac{dM_{xy}}{dt} = -\frac{M_{xy}}{T_2} \tag{2.31}$$

where $M_z$ and $M_{xy}$ are the longitudinal and transverse components of the magnetization, respectively, and $T_1$ and $T_2$ are time constants that are characteristic of the sample being used. The aforementioned equations have the following solutions:

$$M_z = M_0 + (M_z(0) - M_0)e^{-\frac{t}{T_1}} \tag{2.32}$$

$$M_{xy} = M_{xy}(0)e^{-\frac{t}{T_2}} \tag{2.33}$$

#### 2.3.6.1 Spin Lattice Relaxation ($T_1$)

$T_1$ is called the spin-lattice relaxation constant and governs longitudinal magnetization recovery. It is a measure of how quickly the absorbed RF energy is re-emitted into the surrounding material, or lattice, thus allowing $M_z$ to recover.

$T_1$ is defined as the time necessary for 63% or (1-1/e) of the longitudinal magnetization to recover.

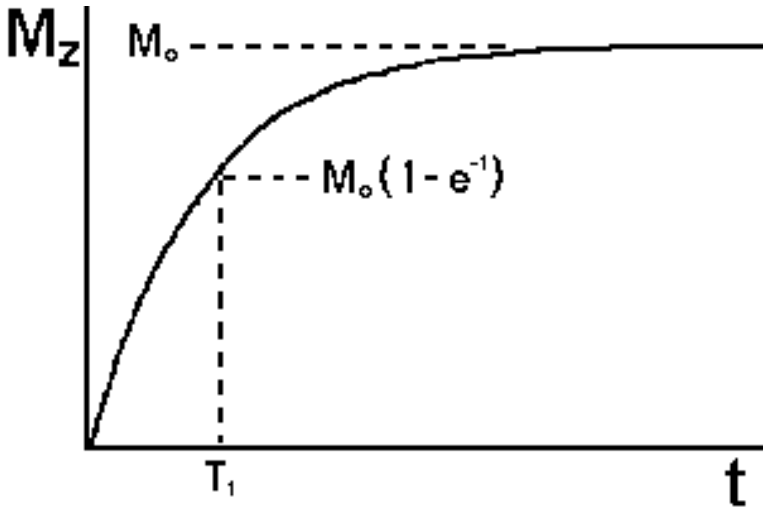


**Figure 2.8 - Spin-Lattice ($T_1$) Relaxation Recovery Curve**

### 2.3.6.2 Spin-Spin Relaxation ($T_2$)

$T_2$ is called the spin-spin relaxation time constant and it governs the decay of transverse magnetization. This occurs due to the interaction between the fields of individual spins. Energy transfer occurs between adjacent spins, so phase coherence is gradually lost due to differing precession frequencies and transverse magnetization decays. $T_2$ is defined as the time necessary for the transverse magnetization to decay to 1/e or 37% of its initial value. It is important to note that because the $T_1$ processes affect transverse magnetization in addition to spin interactions, $T_1 \geq T_2$.

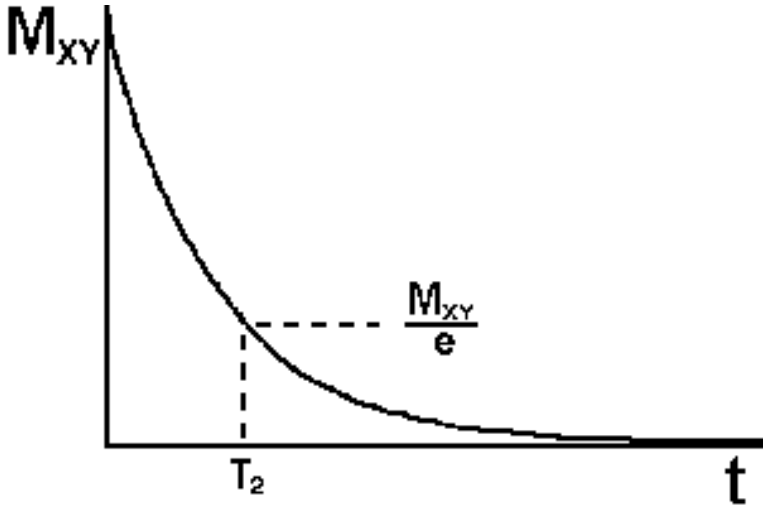


**Figure 2.9 - Spin-Spin ($T_2$) Relaxation Decay Curve**

### 2.3.6.3 $T_2$* and the Free Induction Decay

When the transverse magnetization is precessing around the z axis it creates an oscillating magnetic field which in turn creates an oscillating voltage at the Larmor frequency in the receiver RF coil. In many MRI experiments the receiver coil is usually the same coil used to apply the $B_1$ excitation pulse. This signal represents the transverse magnetization and is called free induction decay (FID) (Figure 2.10).

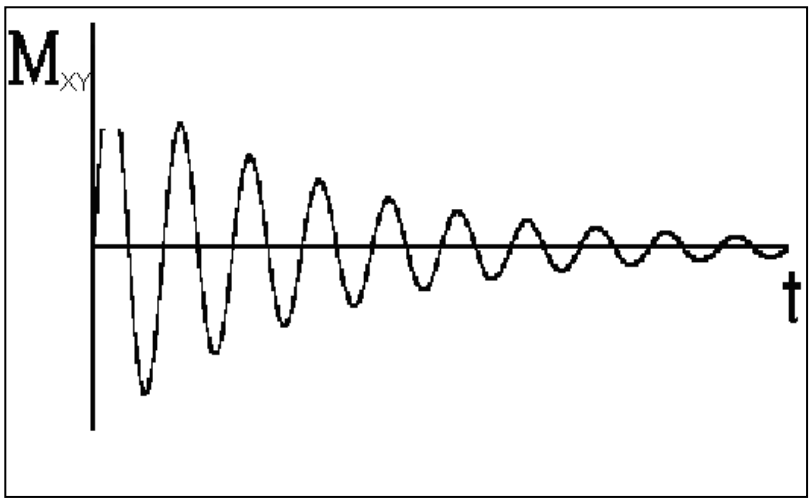


**Figure 2.10 - Typical free induction decay (FID) signal**

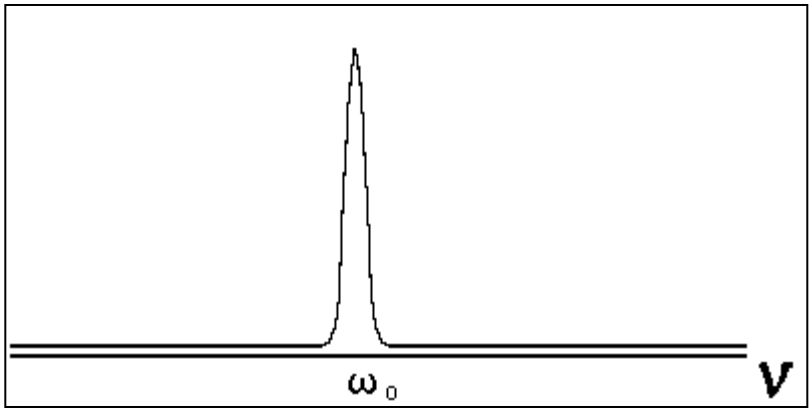


**Figure 2.11 - Fourier Transform of FID**

Intuitively this FID should decay at a rate governed by $T_2$ but in practice this is not what is seen. In reality, the $B_0$ field contains some inhomogeneity that it is represented by

$$B_{0,actual} = B_0 + \Delta B_0 \quad \textbf{(2.34)}$$

Therefore,

$$\frac{1}{T_2^*} = \frac{1}{T_2} + \gamma \Delta B_0 \quad \textbf{(2.35)}$$

Where $T_2$* is the effective relaxation constant for the free induction decay. Because the field inhomogeneities will cause more rapid de-phasing of spins, $T_2$* will be less than $T_2$, except in the case of a perfectly homogeneous $B_o$ field, in which case $T_2$* = $T_2$. The $T_2$* decay constant can be measured directly from the FID curve, provided it is mono-exponential, while it takes a more intricate experiment to measure $T_2$. The acquired FID can be transformed through a Fourier transform, discussed in 2.3.7, into a frequency spectrum like that seen in Figure 2.11.

### 2.3.7 The Fourier Transform

In MRI, image reconstruction relies heavily on the use of Fourier transforms to switch between the time domain and the frequency domain. These two domains are related through the following Fourier transform pair [Wilman, et al., 2006]

$$S(\omega) = \int s(t) e^{-i\omega t} dt \quad \textbf{(2.36)}$$

$$s(t) = \frac{1}{2\pi} \int S(\omega) e^{i\omega t} d\omega \quad \textbf{(2.37)}$$

Where s(t) represents the measured MR signal in the time domain and S(ω) is its Fourier transform. In section 2.3.8 it will be shown that in MRI this relationship gives us a density weighted image through the inverse Fourier Transform of the k-space signal.

### 2.3.8 Spatial encoding, Gradients and K-space

Previous sections have shown that it is possible to generate and detect an MR signal in certain materials, and, through the use of Fourier transforms, see the frequency spectrum of this signal. The discussion is now extended to spatial encoding to obtain MR imaging. In order to do this, some spatial information will need to be embedded in the acquired signal.

One way to spatially encode the acquired data is through the use of magnetic field gradients. These gradients will cause a shift in the local $B_o$ field and thus change the precessional frequency of spins in that area. Gradients are defined in the following way,

$$G_x = \frac{\partial B_0}{\partial x}, G_y = \frac{\partial B_0}{\partial y}, G_z = \frac{\partial B_0}{\partial z} \quad \textbf{(2.38)}$$

It should be noted that although these gradients are labeled with x, y, z they are still changing the $B_o$ field in the z direction. So equation (2.19) is now not only a function of the main magnetic field, but also of the field created by the gradients. In general the expression for $B_o$ becomes:

$$B_{total} = B_0 + \vec{G} \cdot \vec{r} \quad \textbf{(2.39)}$$

If the x direction is used as an example, the expression for (2.19) becomes

$$\omega(x) = \omega_0 + \gamma G_x x \quad \textbf{(2.40)}$$

Taking an isochromat, a position of common frequency, from a specific x position and looking at its signal evolution, it will be

$$S(t) \approx e^{[i\gamma(B_0 + xG_x)t]} \quad \textbf{(2.41)}$$

In the imaging sample there will be a large number of isochromats with a proton density that varies with position, ρ(x). Superimposing all of these isochromats to get the signal for the whole sample yields the following expression,

$$S(t) = \int \rho(x) e^{i\gamma B_0 t}\, e^{i\gamma x G_x t} dx \quad \textbf{(2.42)}$$

The first exponential term will be present in all isochromats, so the signal is demodulated to remove this high frequency term. The following substitution is now made,

$$k_x = \frac{\gamma G_x t}{2\pi} \quad \textbf{(2.43)}$$

In this case $t = t_p$, the encoding time of the experiment. This reciprocal Fourier space is called k-space. After these two steps, equation (2.42) becomes,

$$S(k_x) = \int \rho(x) e^{i2\pi k_x x} dx \quad \textbf{(2.44)}$$

This is a Fourier relationship with the inverse transformation being,

$$\rho(x) = \int S(k_x) e^{-i2\pi k_x x} dk_x \quad \textbf{(2.45)}$$

In the above treatment relaxation effects have been ignored in order to describe the general situation. In reality the signal will be weighted by the imaging parameters and by the relaxation times of the sample.

### 2.3.9 The k-space origin

From equation (2.44) it may not be immediately obvious as to whether there is one k-space point which is more important than the others. But upon inspection we can see that some additional interest should be given to the k-space origin, $k_x = k_y = k_z = 0$. At this point (2.44) becomes

$$S(0) = \int \rho(x) dx \quad \textbf{(2.46)}$$

This result is quite powerful as the right hand side of the equation is the total volume of the sample in image space. This means, in an imaging sense, that the intensity of the signal at the k-space origin is equal to the overall amount of signal in image space. The k-space origin is thus the most important point in a sampling regime and care must be taken to have minimal signal attenuation due to sampling effects when acquiring this point [Kuperman, 2000; Wilman, et al., 2006].

### 2.3.10 Frequency and Phase encoding

From equation (2.43) it is evident that k-space can be sampled either by varying the encoding time, $t_p$, or by varying the gradient amplitude. The former case, when t is the running variable, is called frequency encoding. The result is the evolution of different frequencies, caused by the constant gradients, as a function of time. This type of sampling is the most common in clinical applications in

which the relaxation times are long, in particular $T_2$ relaxation. A large number of points on the decay curve can be sampled before the signal is lost. If instead the gradient strength is the running variable and the encoding time constant, the method is called phase encoding.

### 2.3.11 Field of View

The field of view defines the size of the object in the MR image and is a function of the k-space step size and as such is also a function of the encoding time and the gradient strength [Wilman, et al., 2006],

$$FOV = \frac{1}{\Delta k} = \left[\frac{2\pi}{\gamma G \Delta t_p}\right]_{frequency} = \left[\frac{2\pi}{\gamma \Delta G t_p}\right]_{phase} \quad \textbf{(2.47)}$$

### 2.3.12 Contrast mechanisms and imaging sequences

There are several contrast mechanisms that are used for MR imaging, three of which were mentioned in section 2.3.6, namely $T_1$, $T_2$ and $T_2^*$. The way these, and other, contrast mechanisms are exploited by MRI is generally through the choice of the imaging sequence and of the parameters (e.g. timing, gradient strengths etc.) of that sequence. An imaging sequence is simply a combination of RF excitation pulses, the application of varying gradient strengths and the acquisition of the MR signal. There is a multitude of imaging sequences available to the MR user but for the purposes of illustration the gradient echo sequence is shown in Figure 2.12; the image shows the relative timings of each of the gradient pulses along with the RF excitation pulse and finally the acquired signal.

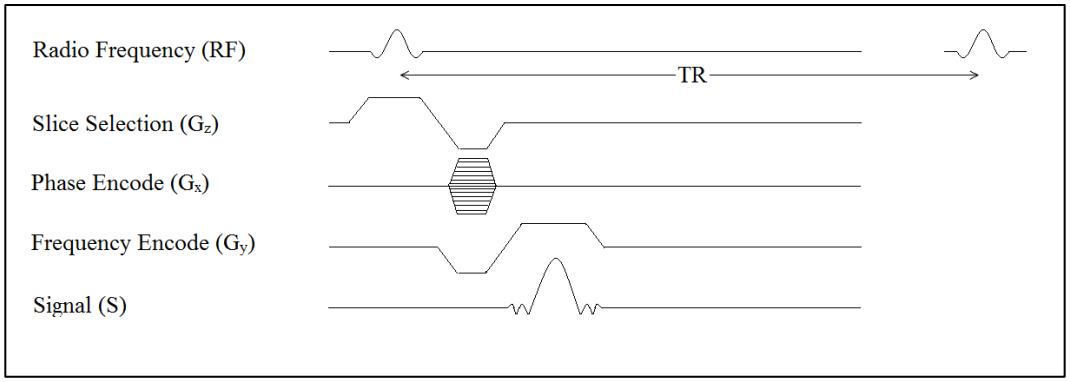


**Figure 2.12 - Gradient Echo sequence showing the radio frequency excitation pulse, slice select gradient, phase encode gradient, frequency encode gradient and the MR signal. Parameters at the same horizontal position occur simultaneously.**

### 2.3.13 Signal-to-Noise Ratio

In chapters 4 and 5 the signal-to-noise ratio (SNR) will be used as a measure of image quality so it will be useful to define it here. As the name suggests, the SNR of an image is defined as the ratio of the mean image intensity in a chosen region of interest to the square root of the noise variance (i.e. the standard deviation of the noise). The SNR is a measure of image quality, with a higher SNR being desirable. In principle, it depends on many factors including, but not limited to, main magnetic field strength, type and characteristics of RF coils, imaging parameters and selected pulse sequence. However, in this work we will look at SNR degradation caused by RIC, holding the above mentioned factors constant.

$$SNR = \frac{mean\ intensity}{\sqrt{noise\ variance}} \quad \textbf{(2.48)}$$

## *2.4 References*

Abdel-Rahman, W., Seuntjens, J. P., Verhaegen, F., & Podgorsak, E. B. (2006). Radiation induced currents in parallel plate ionization chambers: Measurement

and Monte Carlo simulation for megavoltage photon and electron beams. *Medical Physics , 33* (9), 3094-3104.

Degenhart, H. J., & Schlosser, W. (1961). Transient effects of pulsed nuclear radiation on electronic parts and materials. *IRE Transactions on Component Parts*, 124-128.

ICRU85. (2011). *Fundamental quantities and units for ionizing radiation (revised).* Oxford University Press.

Johns, H. E., & Cunningham, J. R. (1983). *The physics of radiology* (4th ed.). Springfield, Illinois, U.S.A.: Charles C Thomas.

Johns, H. E., Aspin, N., & Baker, R. G. (1958). Currents induced in the dielectrics of ionization chambers through the action of high energy radiation. *Radiation Research , 9*, 573-588.

Kuperman, V. L. (2000). *Magnetic Resonance Imaging: Physical Principles and Applications.* San Diego: Academic Press.

Meyer, R. A., Bouquet, F. L., & Alger, R. S. (1956). Radiation induced conductivity in Polyethylene and Teflon. *Journal of Applied Physics , 27* (9), 1012-1018.

Nahum, A. (2007). *Handbook of radiotherapy physics: theory and practice.* (A. N. P. Mayles, Ed.) Boca Raton, Florida, U.S.A.: Taylor and Francis Group.

Salvat, F., Fernandez-Varea, J., & Sempau, J. (2009). *PENELOPE-2008, A code system for Monte Carlo simulation of electron and photon transport.* Barcelona: OECD Nuclear Energy Agency.

Sato, F., Tanaka, T., Kagawa, T., & Iida, T. (2004). Impedance measurements of thin film ceramics under ion beam irradiation. *Journal of Nuclear Materials , 329-333*, 1034-1037.

Wilman, A., & Beaulieu, C. (2006). *Course notes for BME 564*

# 3 Radiation induced currents in MRI RF coils: Preliminary measurements and observations

*A version of this chapter has been published: B. Burke, B. G. Fallone and S. Rathee "Radiation induced currents in MRI RF coils: application to linac/MRI integration," Phys. Med. Biol.* ***55****, 735-746 (2010)*

## *3.1 Introduction*

Since the premise of linac-MRI integration is based on simultaneous irradiation and MRI data acquisition, and since MRI forms an image from the signals induced in RF coils, the RIC induced in the MRI RF coils could be detrimental to the SNR in MRI and introduce image artefacts. High SNR and high quality, artefact-free images are necessary for the success of real-time image guidance. It is therefore imperative that RIC in MRI RF coils be investigated. The objective of this chapter is to report on the measurement of the instantaneous RIC in two different MRI RF coils exposed to linac's pulsed radiation, to examine the frequency characteristics of the RIC and to determine some of the fundamental characteristics of RIC.

## *3.2 Materials and Methods*

### 3.2.1 Dependence of RIC on RF coil and microwave power source

Linear accelerators produce RF noise through the pulsing of the power modulator supplying power to the klystron or magnetron. The RF noise from these clinical linacs was shown to be present everywhere in the patient treatment vault [Burke,

et al., 2009]. If not properly shielded the RF noise will completely dominate the RIC signal measured in RF coils, as shown in Figure 3.1. The experimental setup is shown schematically in Figure 3.2. The RF coil was placed on a wooden stand inside a Faraday type RF cage (Model FC-10, LBA Technologies, Greenville NC) to shield the RIC measurements from unwanted RF noise produced by the clinical linacs [Burke, et al., 2009].

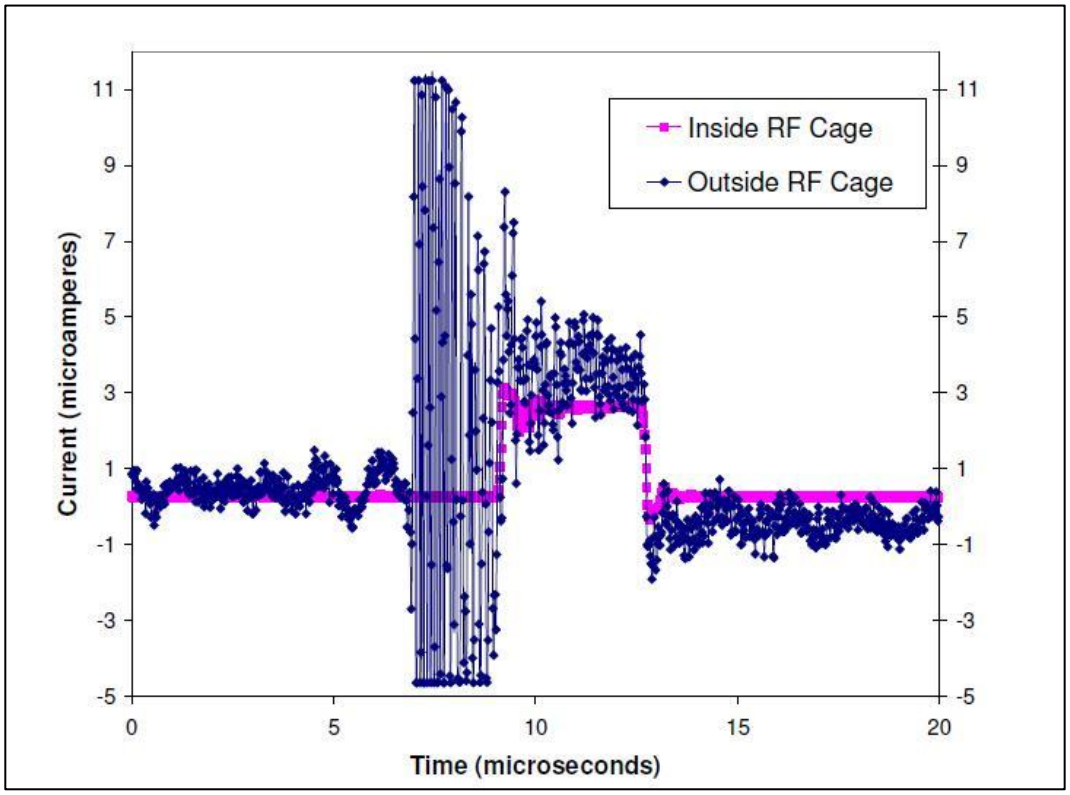


**Figure 3.1- RIC signal measured inside (pink) and outside (blue) an RF cage. It is evident that the RF noise dominates the measured signal without the RF cage (blue) and that the high frequency RF noise is effectively removed from the measured signal when the RF cage is used (pink). Note: the magnitude of the RF noise spikes are clipped due to the window used.**

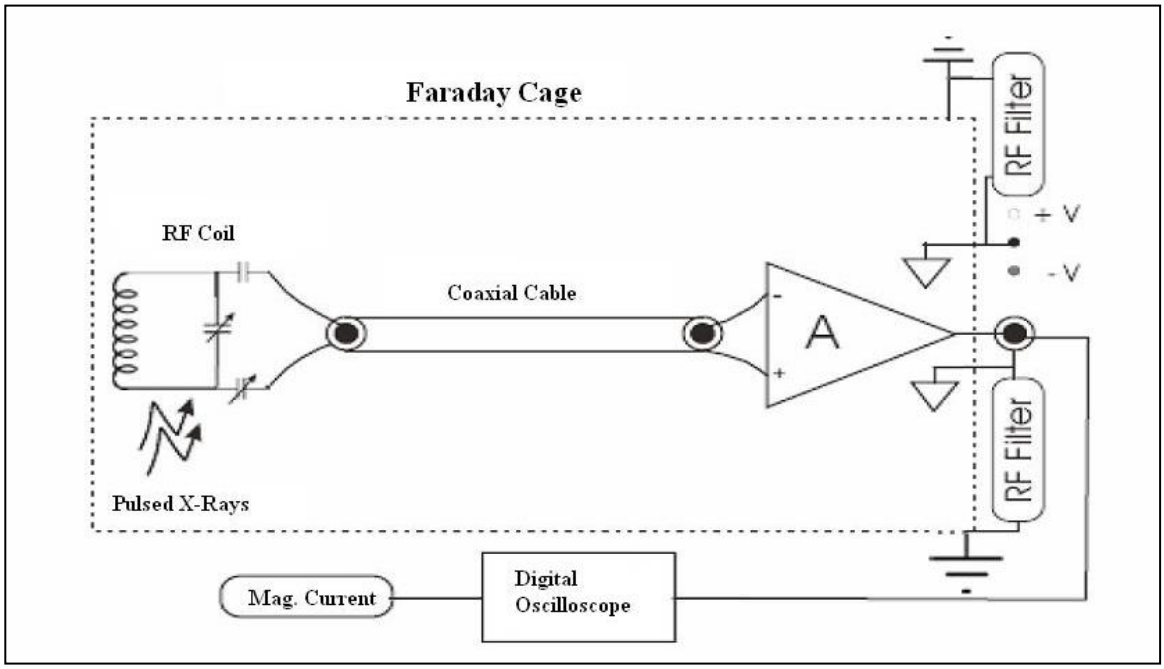


**Figure 3.2 - Schematic representation of RF coil inside Faraday cage (dotted line). The pulsed radiation beam is focused on the RF coil. The radiation induced current is amplified and then detected by a digital oscilloscope, which is triggered by the linac magnetron/klystron current.**

Two different coils were used (Figure 3.3) to examine what difference, if any, the coil design had on RIC. A CAT Solenoid coil (National Research Council Canada) has copper strips as the windings with a resonant frequency at ~8.5 MHz. It has an inner diameter of 9.5 cm, a length of 11.7 cm and 5 continuous windings of thin, 1.2 cm wide copper sheet. The second coil was a black solenoid coil (National Research Council Canada) with 10.0 cm inner diameter and 12.0 cm length, and it is made of 0.64 cm diameter hollow copper pipe. Five concentric rings are connected in series to provide a solenoid structure. A capacitor connects each concentric ring to the next. An inductive matching network (a copper ring with an 820 pF capacitor) is employed to connect the resonator with an active transmit/receive (T/R) switch incorporated with the coil. The tuning range for

black solenoid coil is from 9.2 MHz up to 9.4 MHz. These coils were designed for a 0.2 T (CAT) and 0.22 T (black solenoid) magnets, respectively, and both have an impedance of 50 Ω at resonance. The CAT coil is receive only coil, while the black solenoid coil is a transmit/receive coil.

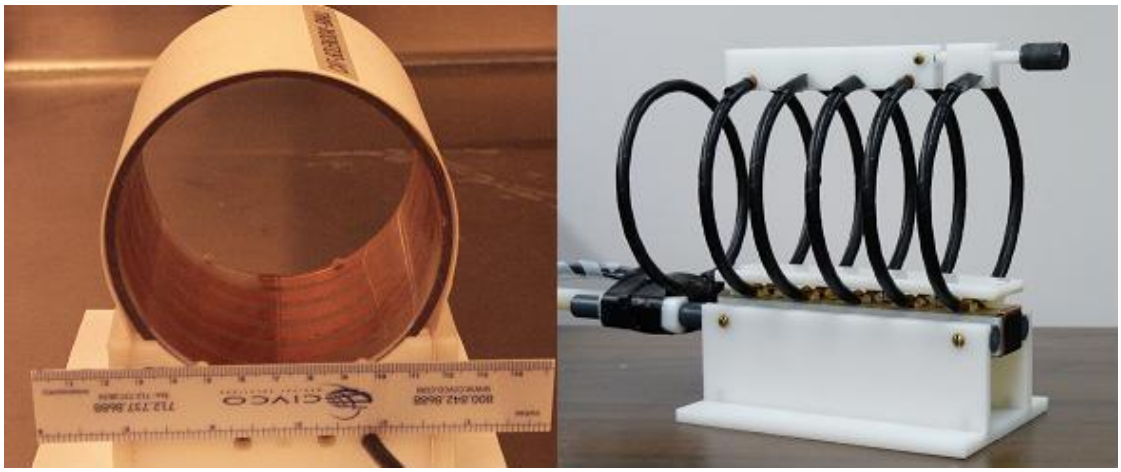

**Figure 3.3 - CAT solenoid coil (left) and black solenoid coil (right). The strips of copper winding can be seen in the bore of the CAT coil, while the black coil has windings made from cylindrical copper pipe.**

The coils in the RF cage were connected to a high speed, low current amplifier (Model 59-179, Edmund Optics, Germany), with a 50 Ω input impedance, via coaxial cable. All the measurements were made with a nominal gain setting of $10^5$ V/A and a nominal bandwidth of 10 MHz. The amplifier was not irradiated. The power supply and amplifier output connections were brought to the exterior of the RF cage through RF filters. A coaxial cable from the exterior of the RF cage connected the amplifier output to an oscilloscope (Model DSO6104A, Agilent Technologies, Santa Clara, CA) which measured the induced current. The RF cage was then placed on the treatment couch of the linac and exposed to pulsed radiation to induce current in the RF coil. The center of the coil was placed at approximately 115 cm from the radiation source and the field size was chosen to cover the entire coil.

Two different linacs were used: a Varian 600C and a Varian Clinac 23iX (Varian Medical Systems, Palo Alto, CA), being powered by a magnetron microwave source and a klystron microwave source, respectively. These two linacs were used to see if any differences in RIC would arise due to the difference in the RF power source. The magnetron is an oscillator and requires some time after the high voltage pulse in order to produce RF with adequate power [Karzmark, et al., 1993]. This leads to a slower rise time of the radiation pulse than from the klystron powered linac. The klystron, on the other hand, amplifies the low power microwaves signals by drawing power from the electrons injected by the electron gun [Karzmark, et al., 1993]. There is less delay between the electron injection and the production of high power microwave power. This leads to quick rise times and a stable klystron current. No large differences in the magnitude or the RIC were expected between the two systems, but the slight difference in linac pulse shapes could lead to some significant differences in frequency spectrum of the RIC signal. A nominal 6 MV x-ray beam was used for irradiation in all experiments with an approximate dose of 0.04 cGy/pulse at 100 cm from the source. The signal voltage waveforms, sampled at 2 GHz and triggered using the magnetron/klystron current (available as a test signal at the linac console), were transferred from the oscilloscope to a PC using a Keithley KUSB 488 GPIB interface (Keithley Instruments Inc, Cleveland, OH) implemented with the software program DADiSP (DSP Development Corporation, Newton, MA). The 2 GHz sampling frequency was the oscilloscope default that is not variable. This high sampling rate provides little benefit to the

measured frequency spectrum of RIC since the amplifier bandwidth extends only to 10 MHz. The frequency spectra of the measured signals were then calculated using DADiSP as follows:

$$S(f) = \sqrt{\frac{\sum_{i=1}^{N} \left| DFT_i\left(s(t)\right) \right|^2}{N}} \quad \textbf{(3.1)}$$

Where *DFT* is the discrete Fourier transform, *s(t)* is the time-dependent voltage waveform, *N* is the number of signal acquisitions (1000), and *S(f)* is the final frequency spectrum. Since the bandwidth selected for the current amplifier at the specified gain setting was 10 MHz, any frequencies above 10 MHz were ignored in the spectral data. The measured frequency response of the current amplifier, *G(f)*, was used to correct the measured power spectrum to obtain appropriate current spectral density values, *I(f)*.

$$I(f) = \frac{S(f)}{G(f)} \quad \textbf{(3.2)}$$

Using the methods just described, four different measurement scenarios will be presented using each of the two MRI RF coils exposed to radiation by each of the two linacs.

### 3.2.2 Characterization of RIC

Further experiments were performed to determine some characteristics of the RIC such as: isolating the coil component responsible for the RIC, its dependence on the dose rate and the effect of adding buildup material. These three experiments were performed on the CAT coil alone using the same setup as described above. The CAT coil was favoured over the black coil because of its continuous coil winding and simpler electronic circuitry. Also, the shape of the RIC curve is

similar to the expected shape of the radiation pulse in the case of the CAT coil which makes the interpretation of experimental data simpler.

To isolate the source of the RIC, the coil/cage setup was placed as close to the linac treatment head as possible. A 2.5 cm wide beam, whose length was sufficient to cover the coil diameter, was stepped along the length of the coil. At each step, the RIC was measured. A measurement was also taken with the entire coil in the linac beam for comparison purposes. The linac used for this experiment was the Varian 600C producing a nominal 6 MV x-ray beam. A 10 μs acquisition window was used to display the oscilloscope traces.

The effect of the dose rate on the RIC was determined by varying the distance between the RF coil and the radiation source. This was done because, for patient safety reasons, the instantaneous dose rate (dose per pulse) on clinical linacs is generally not changed, which could be accomplished by varying the microwave input power, electron gun current to change the injected electrons etc. For these RIC measurements, the linac average dose rate (MU/min) is not the quantity of interest. The dose per pulse of the linac will determine the magnitude of the RIC in the measured pulses. The dose per pulse can easily be varied within a limited range by varying the distance of coil from the source. The distance was incremented by 5 cm steps from an initial source-to-coil distance of 67.5 cm to a final source-to-coil distance of 107.5 cm. At each distance the radiation beam covered the entire coil. Once acquired, an average signal was obtained at each distance by taking the mean of the uniform portion of the RIC curves, and this

was then plotted against the inverse square of source-to-coil distance. The linac used for the experiment was the Varian 600C, using a nominal 6 MV x-ray beam.

Finally, the effect of wax buildup on the RIC was examined by placing the coil in the linac beam without any buildup and then with wax buildup placed outside and inside the coil (Figure 3.4). This experiment was performed on a Varian Clinac 23iX in a nominal 6 MV x-ray beam and was undertaken to see if wax buildup could be used to reduce the RIC signal, which would then suggest that electronic disequilibrium in the coil conductor is the cause of RIC. A more detailed look at the effects of buildup on the RIC is presented in Chapter 4.

**Figure 3.4 - CAT coil with wax buildup applied**

## *3.3 Results*

### 3.3.1 Dependence of RIC on RF coil and microwave power source

The measured RIC data as a function of time are displayed in Figure 3.5 and Figure 3.6. The displayed RIC curves are frame averaged for display purposes only, while the individual acquisitions were used in the spectral analysis described

in section 3.2. All figures have an identical x-axis span of 20 μs, but the y-axes have been adjusted for display. Figure 3.5 shows the measured RIC for the CAT and black solenoid coils, when exposed to the pulsed radiation of the Varian 600C, magnetron-powered linac. There are clear differences between the RIC pulse shapes in the two coils. The CAT coil displays an RIC curve that has approximately the same duration as the magnetron current pulse and the linac radiation pulse (~ 5 μs). The black solenoid coil shows a more gradual increase and decrease in RIC, its duration is longer that than of the linac radiation pulse (~ 10 μs), measured from the first appearance of signal (~ 6 μs) until the signal returns to zero (~ 16 μs). Figure 3.6 shows the RIC curves for the CAT and black solenoid coils, measured when exposed to the pulsed radiation of the Varian 23iX, klystron-powered linac. Again, the CAT coil shows a RIC curve whose pulse length is approximately the same as the linac radiation pulse, while the black solenoid coil again shows a RIC curve which is very different from that of the CAT coil. The RIC of the black solenoid coil measured on the klystron unit (Figure 3.6) is consistent in shape with the RIC curve measured on the magnetron unit (Figure 3.5).

The results of the spectral analysis described in section 3.2 are shown in Figure 3.7 and Figure 3.8. Figure 3.7 and Figure 3.8 are the root-mean-squared (RMS) spectral densities corresponding to the cases shown in Figure 3.5 and Figure 3.6, respectively. All of these figures are displayed from 0 to 10 MHz and plotted on a vertical log scale with the same range to allow for direct comparison.

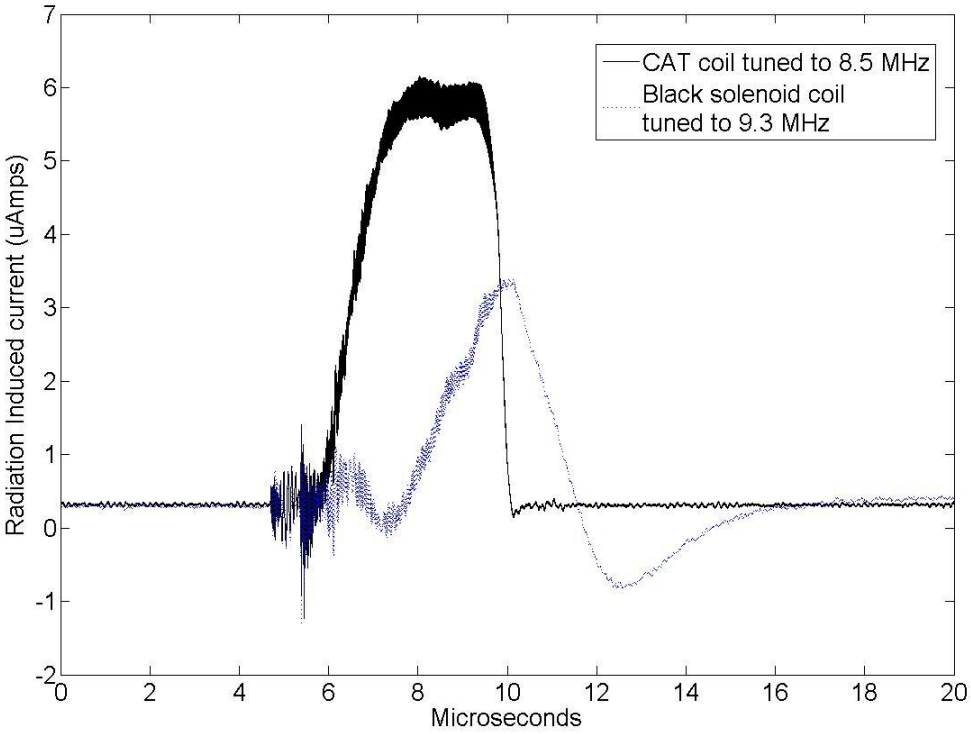


**Figure 3.5 - Frame averaged oscilloscope trace of CAT coil RIC measured on Varian 600C linac.**

.

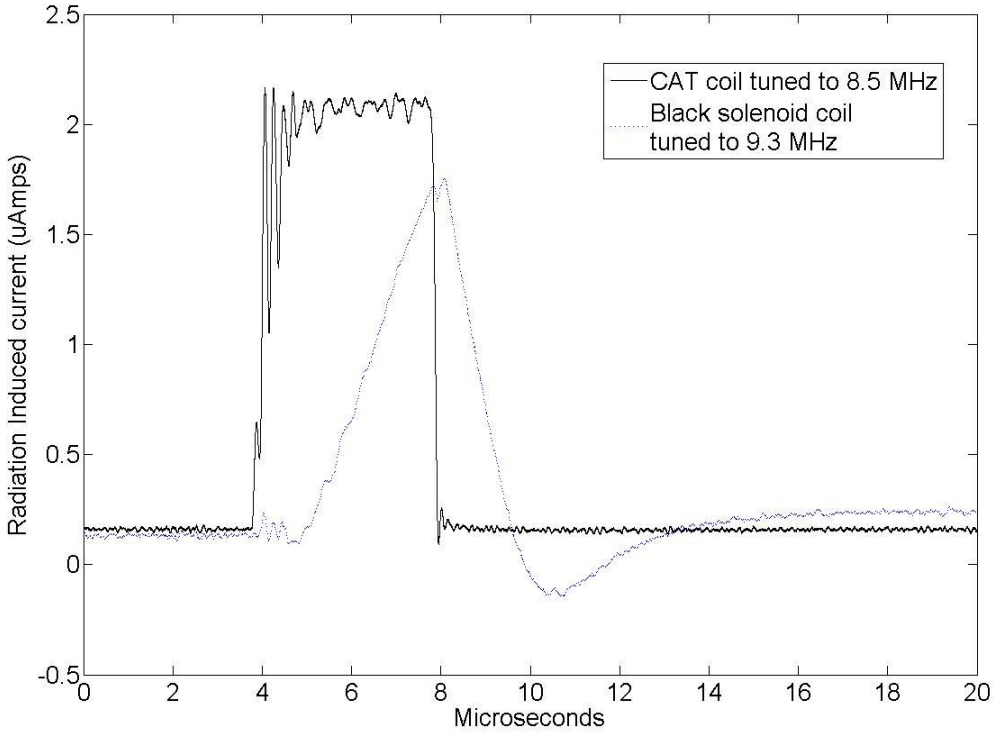


**Figure 3.6 - Frame averaged oscilloscope trace of CAT coil RIC measured on Varian Clinac 23iX.**

Inspection of the figures shows that all 4 scenarios have a maximum RIC component around 0.05 MHz (1/(20μs)). As expected, there are significant differences between the RIC spectra of the CAT and the black solenoid coils. Figure 3.7 shows that the CAT coil has an oscillating decrease in RIC from DC to approximately 4 MHz then has a steady increase from approximately 4 MHz to 7.5 MHz, followed by a sudden drop to a minimum near the coil resonant frequency. Figure 3.7 also shows that the black solenoid coil has a dissimilar response; it decreases steadily, aside from a small increase around 6.5 MHz, from DC until it has a maximum around the coil resonant frequency of 9.3 MHz. Figure 3.8 shows a similar oscillating decrease from DC to 4 MHz in the CAT coil, but the oscillations extend all the way out to 6.5 MHz in this case. Figure 3.8 also

shows that the increase that occurs at 4 MHz is much smaller in span compared to that in Figure 3.7, but again there is a minimum around the coil resonant frequency. Finally, Figure 3.8 shows the black solenoid coil again has a very steady decrease in RIC from DC all the way out to the maximum near coil resonant frequency.

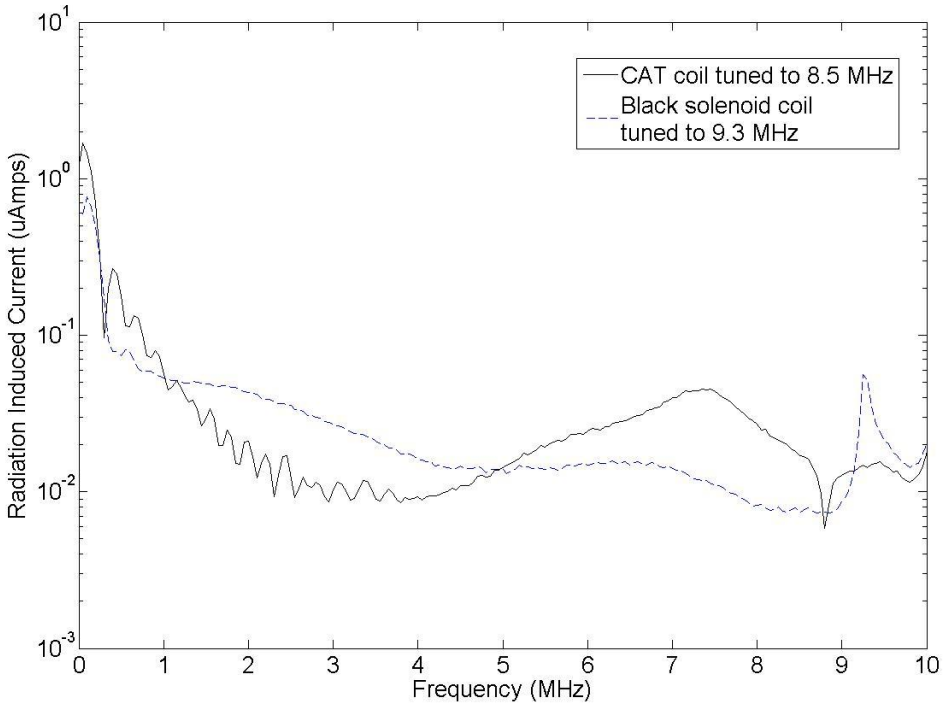


**Figure 3.7 - Frequency spectrum of CAT and black solenoid coils RIC measured on Varian 600C linac, calculated as the RMS magnitude of the DFT.**

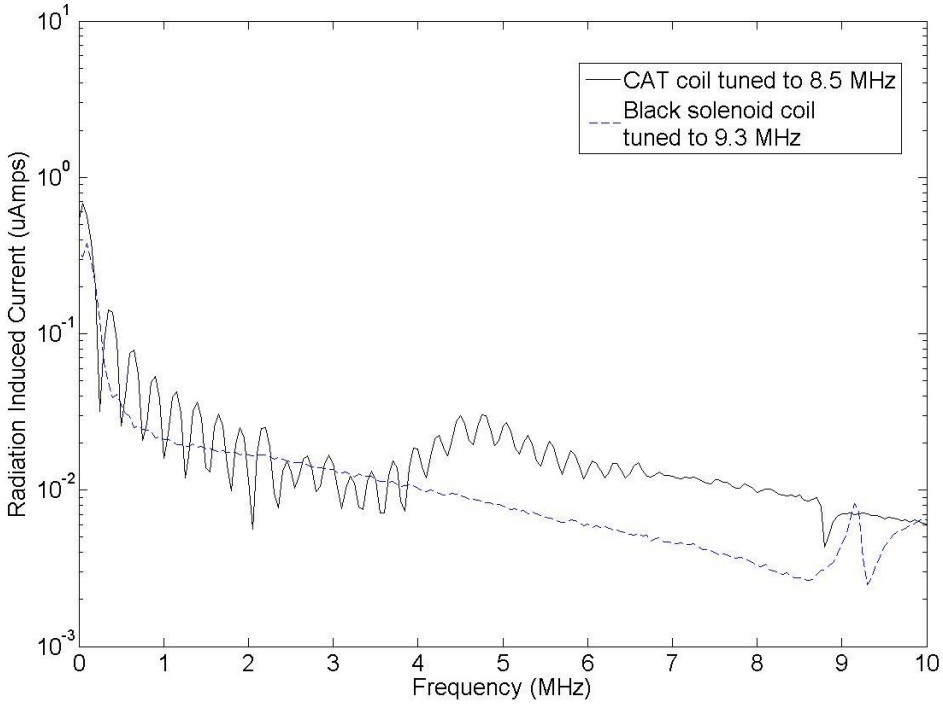


**Figure 3.8 - Frequency spectrum of CAT and black solenoid coils RIC measured on Varian Clinac 23iX, calculated as the RMS magnitude of the DFT.**

### 3.3.2 Characterization of RIC

The results of the experiments described in section 3.2.2 are shown in Figure 3.9 to Figure 3.11. Figure 3.9 shows clear evidence that the major source of the RIC is the copper windings of the RF coil. When the small beam is focused on part of the copper winding a much smaller current is induced compared to when the entire coil is irradiated. Also, when the beam is not incident on the copper windings there is a small negative current induced, likely caused by some small scatter from the aluminum RF cage. During the irradiation the RF cage, the coil and the wooden stand are all exposed to the radiation beam. When the beam is not striking the coil it is still striking the other structures, in particular the top and bottom of the aluminum cage, which can lead to scattered electrons coming to

rest in the coil, thus resulting in a negatively charged coil which will result in a small negative current.

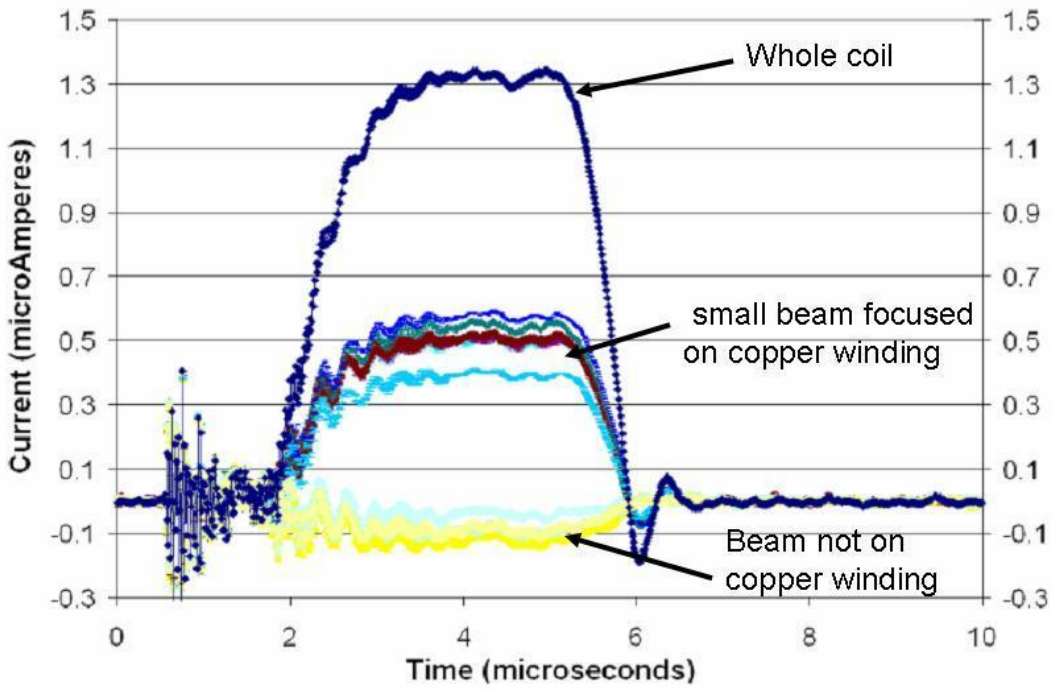


**Figure 3.9 - Isolation of copper winding as source of radiation induced current. Magnitude of the RIC pulse is larger when the entire coil is irradiated compared to only 2.5 cm width. A very small current of opposite polarity occurs when the copper winding is not directly irradiated**

Figure 3.10 shows the effect of dose rate on the RIC. The average current was calculated as the mean of the uniform portion of the RIC curves. Figure 3.10 shows a steady decrease in RIC as the separation is incrementally increased. Note that the reference distance in the Figure represents the largest separation distance, 107.5 cm, mentioned in section 3.2.2., so moving to the right on the x-axis represents moving the coil closer to the radiation source. Figure 3.10 shows a very linear relationship between the inverse squared distance and the average induced current. The data clearly show that the current induced in the coil is due to radiation since the photon radiation emitted from the target in the linac will show an inverse squared decrease with distance from the source.

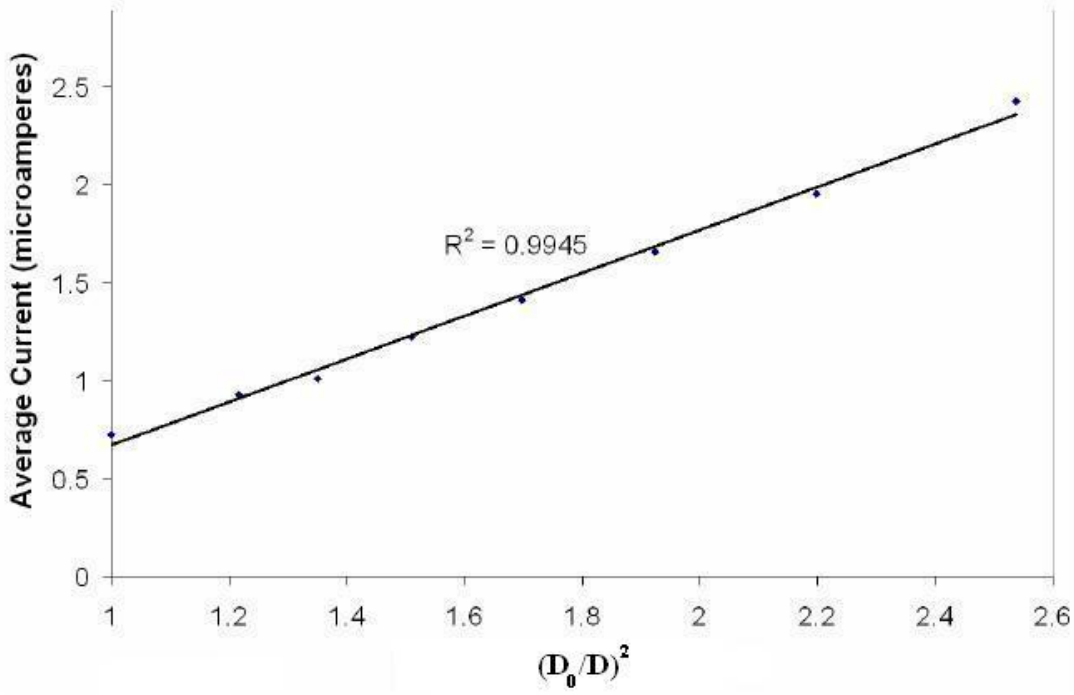


**Figure 3.10 - Mean current from uniform portion of RIC traces at various distances from the source plotted against the inverse squared distance. The error bars are of the same size as the plotted dots. $D_0$ is the reference distance (107.5 cm) and D is the distance between the coil and radiation source.**

The addition of wax buildup to the CAT coil had the effect of reducing the magnitude of the RIC (Figure 3.11). It is important to note that although the magnitude of the RIC was decreased, it was not eliminated.

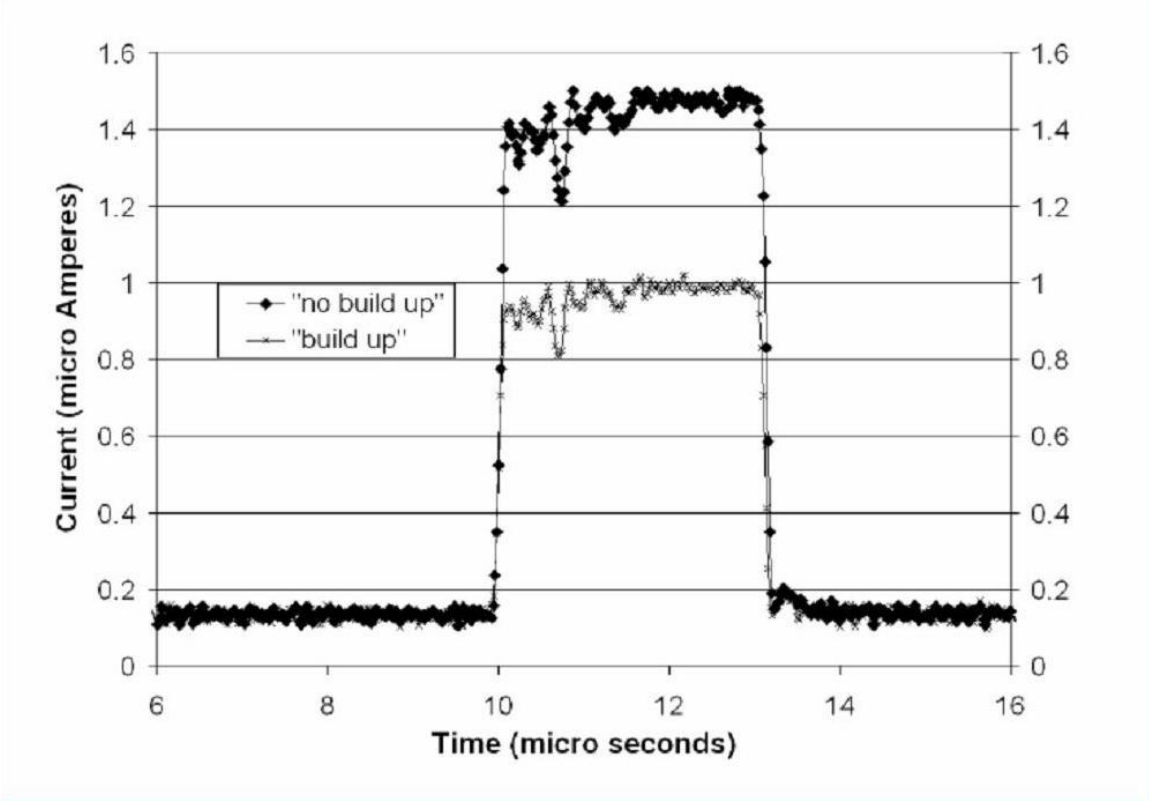


**Figure 3.11 - Effect of wax buildup on radiation induced current. The magnitude of RIC pulse is reduced due to the buildup indicating electronic disequilibrium as the possible mechanism of RIC.**

## *3.4 Discussion*

Examining the results presented in Figure 3.5 through Figure 3.8 there is a definite, measurable RIC present when MRI RF coils are exposed to the pulsed radiation of a linac. These curves are a preliminary indication that the photon beam can induce current in the conductor of the RF coil as the RF noise was completely eliminated by the RF cage. The presence of this effect is independent of the coil used, evident from the presence of RIC in both coils. It is also independent of the microwave power source of the linac, whether magnetron or klystron, evident from RIC measured on both linacs.

However, the time based characteristics (i.e. RIC signal shape) are not independent of these factors. There is a very obvious difference between the RIC

in the CAT and the black solenoid coils (Figure 3.5 and Figure 3.6). The RIC in the CAT coil is very similar in duration to the magnetron (Figure 3.5) and klystron (Figure 3.6) current pulses, while the RIC in the black solenoid coil has a very distinct shape and duration, which does not correspond to the magnetron and klystron current pulses. A plausible cause for the different shapes of the RIC curves may be the difference in electronic circuitry present in the two coils. The CAT coil is a receive-only coil with simple matching and tuning circuitry containing only the inductive and capacitive circuit elements. There is a smaller number of capacitors in this coil and these are generally outside the radiation beam in the experiments. The black solenoid coil is a transmit/receive (T/R) coil and as such has a more complicated circuitry. The black coil also has capacitors in between each coil winding (as stated in § 3.2) and these could be storing charge or simply modifying the shape of the RIC, thus causing the shape seen in Figure 3.5 and Figure 3.6. These capacitors are always in the radiation beam during irradiation. Certain circuit elements could be more radiation sensitive than others, including the T/R switch. The T/R switch circuit in the black solenoid coil could be modifying the shape of the RIC. This hypothesis can be tested by removing the transmit/receive switch circuit from the coil. This was not done as the coil was borrowed and could not be dismantled.

There are also some small, qualitative differences observed between the RIC generated by the magnetron-powered and the klystron-powered linacs. The largest difference seen (Figure 3.5 and Figure 3.6) when comparing these curves is that the klystron linac RIC pulse has faster rise and fall times compared to the

magnetron linac, as described in § 3.2.1. The effects of these linac-based differences are likely insignificant as the RIC is still present in both cases and needs to be addressed regardless of its shape.

Next, the frequency characteristics of the RIC were examined in Figure 3.7 and Figure 3.8. As expected, based on the initial shapes of the RIC curves, there are qualitative differences seen between the spectra seen for the CAT and the black solenoid coils that were mentioned in section 3.3.1. Again, these differences could be caused by the circuitry of the coils and there is some evidence in these figures that supports this hypothesis. Namely, there are distinct features in the spectra for both coils near their resonant frequencies. The CAT coil shows a decrease in signal near 8.5 MHz in the spectra from both linacs, while the black solenoid coil shows an increase in signal near its resonant frequency of 9.3 MHz for both linacs (Figure 3.7 and Figure 3.8). The reason for the opposite trends in the two coils is not known at this time.

It would have been interesting to speculate on the impact of RIC on the received signals in MRI. However, the MRI signal is highly variable and depends upon several factors including the Larmor frequency, applied $B_1$ field strength and the available magnetization in the sample. Moreover, the amount of voltage presented by the RIC to the input of pre-amplifier in the signal acquisition chain depends upon the frequency spectrum of the RIC and the frequency dependent input impedance of the pre-amplifier.

It should also be noted that the frequency analysis was performed to examine the frequencies present in the RIC for our specific experiments.

Theoretically, only the signals around the Larmor frequency (42.6 MHz/T for Hydrogen) are important in MRI. However, the experimental signal acquisition chain is complex involving pre-amplification, variable gain amplification, analog and digital filtering, heterodyne mixing and digitization. Therefore, the impact of RIC on the images will depend upon both magnetic field strength and the particular configuration of the data acquisition chain. Moreover, the magnitude and spectrum of the RIC is also dependent upon the dose rate of the radiation producing device. Thus, it is easier to explore the effect of RIC on the SNR in MR images experimentally which is the topic of future investigation (Chapter 5).

Finally, some experiments were performed to characterize the RIC, as described in the results section, § 3.3.2. These results indicated that the copper winding of the RF coil is the main source of RIC, the RIC is linearly dependent on dose rate and the RIC is diminished, but not eliminated, with the application of wax buildup. It should be noted that the wax buildup did not surround the outer and inner circumferences of the coils. This may be the reason that the RIC was not completely eliminated. These results suggest that the probable mechanism for this current is an electronic disequilibrium in the copper windings of the RF coils. If electronic equilibrium could be established within the RF coil windings without detriment to the coil's function, then it is possible that the RIC could be eliminated. This could be achieved by placing copper as the build up and backscattering material in the coil, insulated from the coil winding. Further investigation of RIC and electronic equilibrium are being carried out in flat copper strips using measurements and Monte Carlo simulation. Using Monte

Carlo simulation, the difference in the net charge entering and leaving a scoring region, i.e. a flat copper strips or a circular winding of real coil, is calculated which is related to the radiation induced current [Abdel-Rahman, et al., 2006].

## 3.5 Conclusions and Future Work

The results show that although the specific characteristics of RIC may change with the type of MRI RF coil and type of linac, the effect is still present and needs to be investigated and eliminated. The copper windings of the coil were isolated as the main source of RIC. A linear dependence of RIC on dose rate was seen. Wax buildup decreased the magnitude of the measured RIC, but did not eliminate it. The results support the hypothesis that the RIC seen in MRI RF coils is due to an electronic disequilibrium in the copper windings of the coil and that RIC may be eliminated if equilibrium could be established.

## 3.6 References

Abdel-Rahman, W., Seuntjens, J. P., Verhaegen, F., & Podgorsak, E. B. (2006). Radiation induced currents in parallel plate ionization chambers: Measurement and Monte Carlo simulation for megavoltage photon and electron beams. *Medical Physics , 33* (9), 3094-3104.

Burke, B., Lamey, M., Rathee, S., Murray, B., & Fallone, B. (2009). Radio frequency noise from clinical linear accelerators. *Physics in Medicine and Biology, 54*, 2483-2492.

Karzmark, C. J., Nunan, C. S., & Tanabe, E. (1993). *Medical Electron Accelerators.* New York: McGraw-Hill.

# 4 Radiation induced current in the RF coils of integrated Linac-MR systems: the effect of buildup and magnetic field

*A version of this chapter has been published: B. Burke, A. Ghila, B. G. Fallone and S. Rathee "Radiation induced current in the RF coils of integrated linac-MR systems: The effect of buildup and magnetic field," Med. Phys.* ***39****, 5004-5014 (2012)*

## *4.1 Introduction*

RIC in RF coils was hypothesized to arise from the ejection of Compton electrons from the RF coil's metal windings, leading to an electronic disequilibrium in the windings [Burke, et al., 2010]. Based on this hypothesis a method was devised that uses buildup material, placed on the metal conductor, in order to restore electronic equilibrium in the conductors thereby reducing the RIC. The following considerations are important: the buildup and the RF coil conductor materials should have a similar density, and a sufficient thickness of buildup must be placed on top of the conductor. These two conditions will ensure an adequate number of electrons that are ejected from the buildup will stop in the RF coil conductor. The electrons coming to rest in the conductor then balance, in terms of electronic charge, those being ejected directly from the coil conductor.

In this study we will: (1) present and validate a Monte Carlo script written to calculate the RIC in metal conductors, (2) use the Monte Carlo script to compare results performed on a planar measurement system by A. Ghila and (3) use the Monte Carlo script to examine the effects of magnetic fields on both the planar conductor and cylindrical coil geometries.

## *4.2 Background*

### 4.2.1 Effect of RIC on Signal to Noise Ratio in MRI

The presence of RIC, or any other extraneous currents, can degrade the signal-to-noise ratio (SNR) in the MR images. Since real-time imaging with linac-MR systems will involve the use of fast imaging sequences, characterized by a lower image SNR, any further sources of SNR degradation are undesirable. In our preliminary investigation, we have observed a measurable SNR loss of 11% between images taken with (linac dose rate of 250 Monitor Units (MU) per minute) and without radiation, as seen Figure 4.1. Images in Figure 4.1 do not show any visible artefact in the MR image obtained in the presence of radiation; however, RIC related streaks are visible in the associated raw (k-space) data, as shown in Figure 4.2. It should be clearly identified that the streaks in k-space are only produced when radiation is incident on the RF coil as the k-space lines disappear when the radiation is blocked even though the linac's beam is still active. Figure 4.1 and Figure 4.2 provide the motivation for this work as the loss in SNR due to the presence of the extraneous signal in the k-space data is undesirable, especially for the SNR challenged, fast imaging sequences required for the real-time imaging. The linac-MRI system used is that described by Fallone et al and the schematics can be found in their paper [Fallone, et al., 2009]. It is also described in detail in § 5.2.

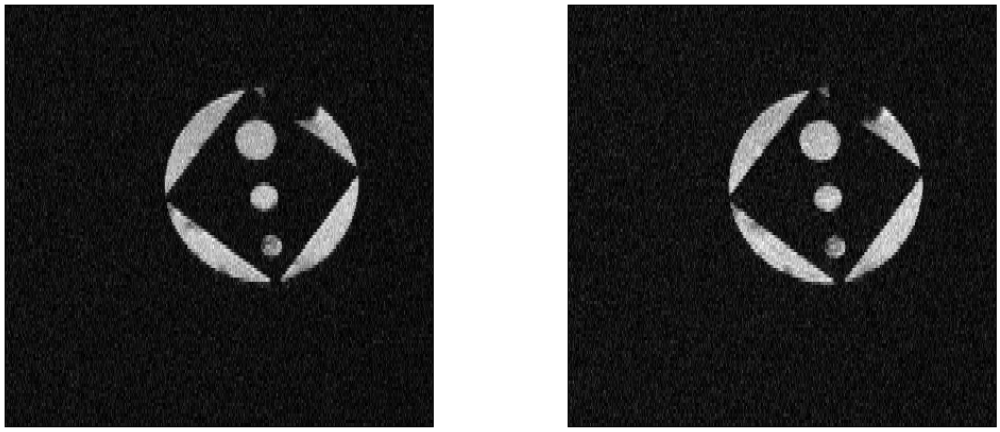


**Figure 4.1- Sample MR Images acquired on Linac-MR system. Images acquired with (a) no radiation beam and (b) with linac producing radiation at rate of 250 MU/min. There is a 11% reduction in SNR in the image obtained with radiation.**

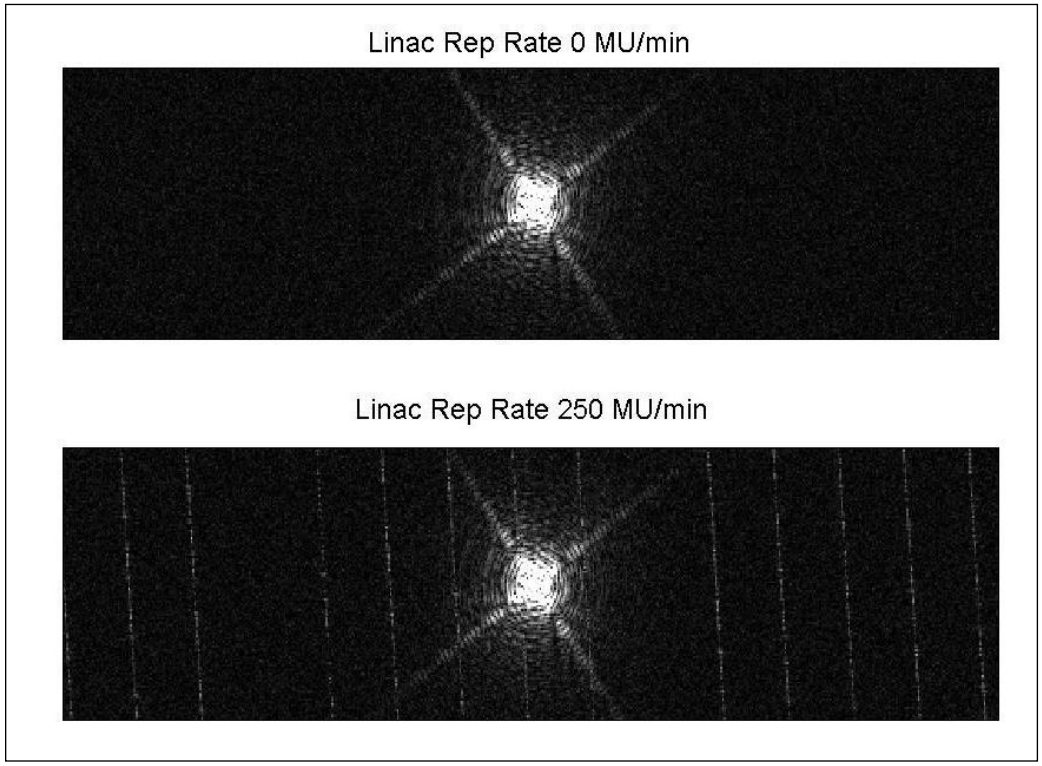


**Figure 4.2 - K-space data for images shown in Figure 4.1. The top image data was acquired with no radiation and the bottom image data was acquired with the linac producing radiation at 250 MU/min. The window and level in the image has been adjusted to make the RIC induced streaks clearly visible. The missing streaks in the regular pattern are due to the dropping of pulses by the linac.**

### 4.2.2 Radiation Effect or Radio Frequency Interference

Several important questions arise regarding the observed interference signal. The fundamental question, i.e. "is the signal caused by irradiation of coil conductor or RF interference?", has been investigated thoroughly in our previous, and this, work. In the work presented in Chapter 3, we used a well designed, commercial RF cage (Model FC-10, LBA Technologies, Greenville, NC), with up to 70dB RF isolation, that housed the coil being irradiated. The observed signal in RF coil inside the RF cage was a well formed pulse whose amplitude followed the well known inverse square law as the coil was systematically moved away from the radiation source. The pulse amplitude was thus linearly proportional to radiation dose rate (Figure 3.10), which would not be the case if this signal was RF noise, as Burke *et al* [Burke, et al., 2009] showed that the RF noise is essentially constant everywhere within the linac vault (See Figure 5 in [Burke, et al., 2009]). For the preliminary k-space data presented here, a lead block was placed in the radiation beam path to completely attenuate the radiation from reaching the RF coil. This block was located far away from the coil, did not form any electrical connection with the linac, MRI or RF cage and would not provide any RF shielding. Lamey *et al* showed (see Figure 9 in [Lamey, et al., 2010a]) that if not properly shielded, the RF noise is visible in the k-space data even when the radiation beam is blocked from reaching the RF coil with the same lead block; however, when the RF is properly shielded there was no interference signal present (See Figures 5 & 7 in [Lamey, et al., 2010a]). The same work exhaustively examined the effectiveness of the RF shielding of the linac-MR

prototype. In particular, Figure 2 by Lamey *et al* shows there is very little RF noise present inside the RF cage. Also, our previous work showed that the majority of the RF noise in linear accelerators emanates from the pulsed power modulator system. In the linac-MR prototype, the modulator is located externally to the RF cage in an adjacent room [Lamey, et al., 2010a]. This ensures that all the RF noise due to the high voltage switching in the modulator is located external to the RF cage around linac-MR prototype, and all of the signals that are fed through the RF cage are filtered to remove any transmitted RF noise [Lamey, et al., 2010a]. Therefore, the observed extraneous signal in the k-space data is caused by irradiation of the RF coil and not by RF interference.

The second important question is related to process by which the RIC interference enters the k-space data. Generally, the RF energy in the excited MRI sample lies in the frequency band around the Larmor frequency (~9.3 MHz for linac-MR prototype). This energy induces RF signal in the coil which is amplified by a broadband pre-amplifier. In our previous work, we determined the power spectral density of RIC signal up to 10 MHz (See Figure 3.7 and Figure 3.8). The RIC signal was measured by an amplifier with a nominal bandwidth of 10 MHz and sampled at 2 GHz, thus, the measured power spectral density represents un-aliased frequency spectrum. The data indicated a broadband presence of RIC interference including the range around the Larmor frequency. The presence of broadband frequencies arises from the fact that the RIC signal is a time limited pulse (< 5 μs with fast rise and fall time, See Figure 3.5 and Figure 3.6), whose Fourier transform will contain many frequencies. These figures also affirm the

notion that the signal is created by radiation as the pulse shape conforms to the timing pulse of the linac.

Finally, the fact that a ~5 μs radiation pulse falls into a single point in k-space warrants further explanation (see Figure 4.2). In the simplest spectrometer, the output signal of the pre-amplifier is generally heterodyned with the pure sinusoidal signal at the Larmor frequency in order to convert it into the low frequency range before sampling. In our experiments, the free-induction decay (FID) is sampled with a sampling interval of 100 μs (sampling frequency = 10 kHz for a bandwidth of ± 5 kHz), thus the radiation pulse can at the most be seen in one sample of the FID. In other words, because the RIC signal is much shorter than the MR sampling interval, the RIC pulses are seen as impulses in k-space, each contained in one k-space point.

## *4.3 Methods and Materials*

### 4.3.1 Monte Carlo RIC simulation algorithm: description and validation

#### 4.3.1.1 Description of the algorithm

All simulations were carried out using the PENELOPE-2008 Monte Carlo simulation program [Salvat, et al., 2009] using the penEasy (2010) steering program. None of the tallies included in penEasy were suitable for calculating the RIC so a custom script for calculating the RIC was written for use with penEasy.

Using PENELOPE's ability to determine geometrical boundary crossings and its tracking of the current material at each step along the particle track, a script was written following the algorithm shown below in Figure 4.3. Within the simulation, the electron's current region and material is compared to its prior region and material each time the particle crosses a geometric boundary. Distinct geometric regions are assigned to the buildup, detector and backscatter materials. PENELOPE uses numerical indexes to identify the materials from the input file, so the RIC script designates a specific material index to be the detection material – much in the same way several of the other penEasy tallies work – and this material is not used for any other geometric region. Therefore, even if the buildup and detector were composed of the same physical material they will remain distinct to the simulation via their different material indexes, thus assuring the simulation accurately computes the RIC. If the electron crosses a geometric boundary into the detector material but its prior material was not the detector, then it is assumed to have entered into the detector. If the electron is not in the detector material after crossing a boundary but its prior region was the detector, then it is assumed to have left the detector. The script thus counts the number of electrons entering and leaving the volume of interest and determines the net charge gained or lost. This charge can then be compared to RIC measurements.

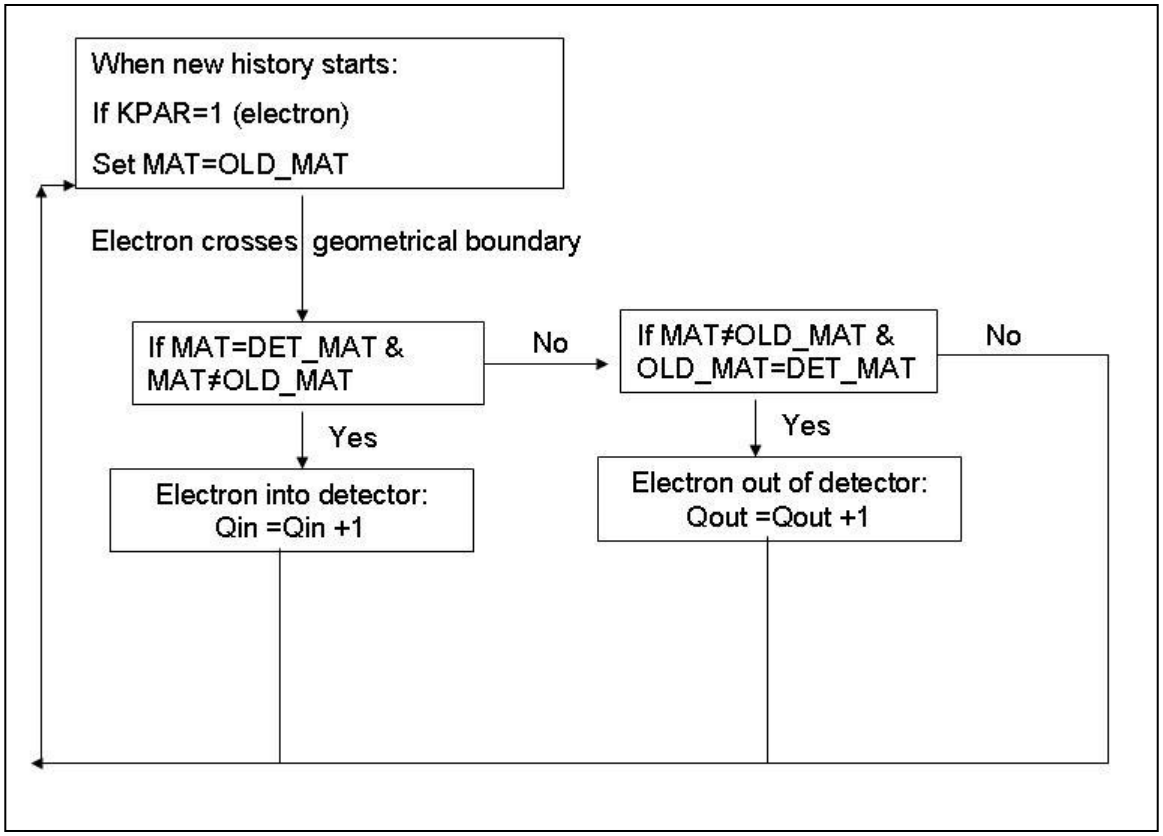


**Figure 4.3 - Generic algorithm for PENELOPE RIC script: Mat is a variable used by Penelope to track the material in which the simulated particle currently resides. Det_Mat represents the material in the input file, defined as the detector; it is not used for any other geometric region. Old_mat is a variable introduced to store the previous material along the particle transport track. It is used for the comparisons shown in the figure. Qin is a counter of electrons originating outside the detector volume and entering in the detector volume. Qout is a counter of electrons originating inside the detector volume and then being ejected from it. The last step in the algorithm is to subtract Qin from Qout to determine the net loss of charge in the detector.**

In addition to storing the accumulated charge in, $Q_{in}$, charge out, $Q_{out}$, and net charge, $Q_{net}$, the simulation also stores the accumulation of $Q_{in}^2$, $Q_{out}^2$ and $Q_{net}^2$ for error calculation purposes. The errors are calculated for each counted variable using a simple standard deviation formula, shown here:

$$\varepsilon_{\bar{Q}_i} = \sqrt{\frac{1}{N-1}\left(\frac{Q_i^2}{N} - (\bar{Q}_i)^2\right)} \qquad \textbf{(4.1)}$$

Where Qi represents each of the three counted variables ($Q_{in}$, $Q_{out}$ and $Q_{net}$), $Q_i^2$ represents the squared value associated with each counter and $\overline{Q}_i$ is the counted variable normalized by the number of histories, N.

PenEasy simulations are controlled through the following 4 parameters: $C_1$ defining the average angular deflection produced by multiple elastic scattering along a path length equal to the mean free path between consecutive hard elastic events, $C_2$ defining the maximum average fractional energy loss between consecutive hard elastic events, $W_{cc}$ representing the cutoff energy loss for hard inelastic collisions, below this energy level soft collisions are simulated, and $W_{cr}$ the cutoff energy loss for hard bremsstrahlung emission. These parameters were set to the following values in all simulations shown herein: $C_1 = C_2 = 0.1$, $W_{cc}$ = 100 keV and $W_{cr}$ = 10 keV. These values were chosen because they provided good simulation efficiency and altering the values had little effect on the results. For example, setting $C_1 = C_2 = 0$, $W_{cc} = 0$ and $W_{cr} = -100$ forces a purely detailed simulation and this did not produce appreciable differences in the normalized RIC simulations.

The radiation sources in various simulations were the phase-space files generated by modeling the 6 MV beam of a Varian 600C linac [St. Aubin, et al., 2010b]. The generated phase-space files were validated by comparing the simulated and measured percentage depth dose curves and profiles in water [St. Aubin, et al., 2010b]. The phase space file used contained approximately 13 million particles comprised mainly of photons (99 %). This number of particles provided adequate simulation accuracy without prolonging simulation time.

### 4.3.1.2 Validation of RIC Monte Carlo algorithm

The simulation algorithm was tested by comparing it to the measurement scenario described in section 4.3.2.1.1, with a few modifications to the measurements. The Monte Carlo simulation of RIC does not account for any charge collected from the ionization of the residual air present in the measurements between the buildup and the detector. This effect has to be minimized in the measurements in order to properly compare them to the simulation results. To accomplish this both the buildup and the backscatter plates were first biased at 10V and then the experiment was repeated with the bias voltage changed to -10 V. In these two situations ionizations would either add or subtract from the RIC, depending on the detector collecting either positive charge (buildup and backscatter at +10V) or negative charge (buildup and backscatter at -10 V). The RIC amplitude was then calculated using:

$$RIC = \frac{M_+ + M_-}{2} \quad \textbf{(4.2)}$$

Where $M_+$ and $M_-$ were the detector's voltage signals measured for the positive and negative polarities, respectively. Simulations were performed at increasing buildup thicknesses, in 0.5 mm increments, to attempt to reduce or remove the RIC from the coils. Both the measured and simulated RIC were normalized to their respective maximum amplitudes occurring without buildup, and the resulting relative RIC values for the increasing buildup thicknesses were compared.

### 4.3.2 Confirmation of buildup method for RIC removal

All measurements in this section were designed and performed by A. Ghila, another graduate student in our research group, they were then used to compare with the simulations which are the focus of this chapter. The methods used by A. Ghila will be presented in order to provide the reader with the information necessary to understand the comparisons of measurements and simulations to come.

A planar measurement system was devised to test the effectiveness of using buildup material to remove RIC from RF coil conductors. The schematic representation of the main experimental setup is shown in Figure 4.4. Plates of copper and aluminum were used as surrogates for the conductive windings of an RF coil. Copper is by far the most commonly used conductor in MR coils, but aluminum has also been shown to be suitable [Rieke, et al., 2005]. The RIC in these plates (henceforth called detectors) was measured and then buildup material was applied in an attempt to reduce or completely remove the RIC from the plate detectors. The whole setup was placed inside a Faraday RF Cage (Model FC-10, LBA Technologies, Greenville, NC) to remove any RF noise emanating from the linac's magnetron [Burke, et al., 2009; Lamey, et al., 2010a]. The detector was connected to a high speed low current amplifier (59-179 Edmund Optics) and all the measurements were taken with a nominal amplifier gain setting of $10^5 VA^{-1}$. The radiation beam was focused on the detector through the RF cage, and the amplifier was not irradiated. The power supply and amplifier output connections were brought outside the RF cage through RF filters. A coaxial cable connected

the amplifier output to an Agilent (Agilent Technologies Inc., Santa Clara, USA) DSO6104A digital oscilloscope, being triggered by the linac's magnetron pulses. The input impedance of the oscilloscope was set to 50 Ohms for all the measurements to match the amplifier's output impedance. The acquired time-dependent signal voltage (i.e. signal trace) was transferred from the oscilloscope to the PC and recorded, using a Keithley KUSB 488 GPIB interface (Keithley Instruments Inc., Cleveland, OH) implemented with the software program DADiSP (DSP Development Corporation, Newton, MA).

The detectors were supported on a stack of material called backscatter plates (See Figure 4.5). All experiments were conducted in the 6MV photon beam from a 600C (Varian Medical Systems, Palo Alto, CA) linear accelerator. The radiation field size was 7.5x7.5 $cm^2$ at the surface of the detector, and the distance from the linac's radiation source to the top surface (i.e. SSD) of the backscatter plates was 123.7cm.

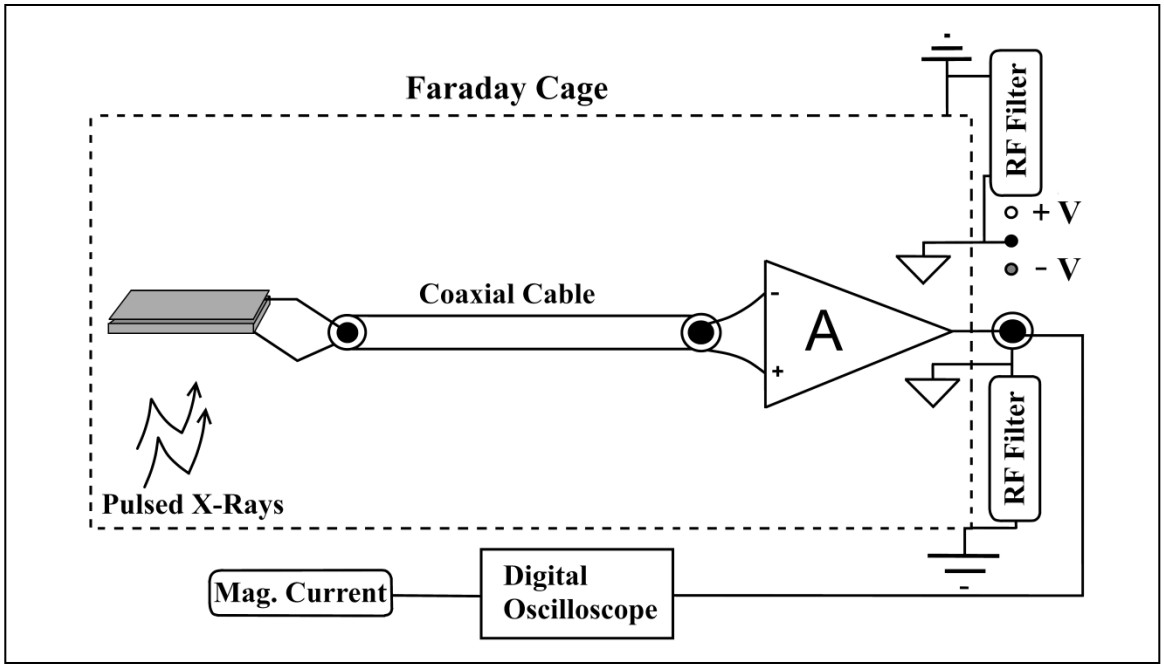


**Figure 4.4 - - Schematic representation of a metal plate detector inside the Faraday cage (dotted line). The linac's pulsed radiation beam is focused on the detector. The RIC is then amplified and detected by a digital oscilloscope being triggered by the linac's magnetron pulses.**

For each measurement of RIC, approximately one hundred oscilloscope waveforms were recorded and averaged to give a time-dependent voltage signal. The RIC amplitude was determined by taking the mean of the uniform portion of the time-dependent voltage signal and subtracting the mean magnitude of the background. The experimental uncertainty in the measured RIC was calculated by taking the standard deviation in background subtracted RIC amplitudes of 100 individual waveforms.

Each of the simulation geometries was designed to precisely reproduce the measurement geometries shown in Figure 4.5a and b; this allowed for accurate comparison of the simulations and measurements. The simulated geometries contained all of the physical structures (Aluminum RF cage, detector, buildup) but none of the electrical structures (cables, amplifier, etc.) because PENELOPE

simulates radiation transport and does not simulate electrical effects. Again, simulations were performed at increasing buildup thicknesses, in 0.5 mm increments, to attempt to reduce or remove the RIC from the coils. The simulations were normalized to the maximum RIC value, i.e. the value without buildup.

#### 4.3.2.1 Detector-buildup combinations

For a given detector-buildup combination, the mean RIC was measured as a function of increasing buildup thickness. Pulsed radiation from the linac also ejects electrons from the buildup material creating a net positive charge. The net positive charge results in a short-lived electrostatic field that may polarize the detector plate. As mentioned before, the measured RIC results from the loss of electrons from the detector plate. Since the electrostatic field may prevent some of the very low energy electrons set in motion in the buildup from reaching the detector, the measured RIC amplitude would be larger than expected for a given buildup thickness. Therefore the buildup was grounded in each of the following experiments.

##### *4.3.2.1.1 Copper detector/copper buildup*

This experiment was performed to verify whether the RIC can be completely removed by establishing complete electronic equilibrium in the detector by using identical buildup material. Moreover, RF coils generally use copper as their conductor material. As shown in Figure 4.5, the detector was a copper sheet, 0.12 mm thick, wrapped on both sides with 3M Tartan 1710 Vinyl Electrical Tape to

electrically insulate it from the rest of the setup. A 2 cm thick stack of copper plates provided the backscatter material. The backscatter copper was in direct contact with the bottom of the RF cage and was thus grounded.

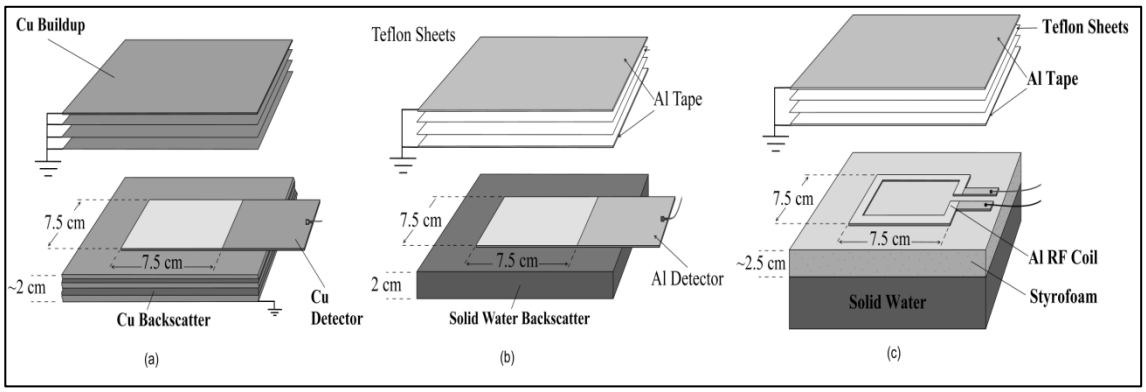


**Figure 4.5 - Schematics of the (a) copper detector/copper buildup measurement setup, (b) aluminum detector/Teflon buildup measurement setup, and (c) aluminum surface coil setup for RIC measurements. The styrofoam represents an air gap between the surface coil and the solid water serving as a patient surrogate. The irradiated portion of the detectors in (a) and (b) is 7.5 x 7.5 cm$^2$. The detectors are electrically insulated from both the backscatter and buildup materials. The copper buildup and backscatter materials in (a) are grounded. The Teflon buildup sheets in (b) and (c) have grounded aluminum tape applied to the top and bottom of the stack.**

#### *4.3.2.1.2 Aluminum detector/Teflon buildup*

The reduction of RIC was also evaluated in aluminum conductor with Teflon buildup (Figure 4.5b), as Teflon has similar density to that of aluminum ($\rho_{Al}$ = 2.7 g/cm$^3$, $\rho_{Teflon}$ = 2.2 g/cm$^3$). Teflon buildup can be incorporated within the housing that supports the coil conductor in practical RF coils. In this case, the detector was an aluminum plate, 0.54 mm thick, insulated on both sides with electrical tape. The backscatter was provided by a 2 cm thick slab of solid water to approximate the tissue that would be present with an actual surface coil. The top and bottom surfaces of the Teflon sheet stack used as buildup were grounded using a ~ 0.06 mm thick aluminum tape.

#### *4.3.2.1.3 Copper detector/Teflon buildup*

Finally, the aluminum detector used in section 4.3.2.1.2 was replaced with the copper detector from section 4.3.2.1.1 to evaluate the RIC reduction in a case where the buildup density is substantially different from that of the detector.

### 4.3.3 Cylindrical coil geometry simulations

These simulations were performed to examine the effectiveness of RIC removal in a non-planar geometry. Since many MRI RF coils are cylindrical, such as solenoid coils, a cylindrical geometry was chosen. The coil design used in the simulation is an approximation of the CAT solenoid coil described by Burke et al [Burke, et al., 2010]. The coil is comprised of 5 copper windings that are 12 mm wide and 0.1 mm thick and separated by 5 mm gaps (Figure 4.6b). In the simulations the copper windings were replaced by aluminum, because in the planar measurements the aluminum conductor/Teflon buildup combination provided the greatest RIC reduction. The Teflon buildup material is only applied to the outside of the coil as seen in Figure 4.6. Simulations were performed at increasing buildup thicknesses, in 0.5 mm increments, to attempt to reduce or remove the RIC from the coils. The phasespace file was recycled 4 times to provide better statistics as fewer interactions were occurring in these coil geometries.

#### 4.3.3.1 Effect of air gaps between patient and RF coil on RIC removal.

Four different ‘patient’ configurations were used to examine the effect of air gaps between the coil and water (tissue surrogate) (Figure 4.6): (1) no air gap, so the

water cylinder is in direct contact with the coil winding's inner surface (Figure 4.6a); (2) and (3) both had a uniform air gap surrounding the entire water phantom, simulating a uniform air gap between the coil and the patient (Figure 4.6b) – (2) used a 1 cm uniform air gap and (3) used a 2 cm uniform air gap – and; (4) a gap that is 1 cm at the top edge and decreases radially from top to bottom to simulate the tissue sag that can occur when a patient lies down (Figure 4.6c). The 6 MV beam was incident on the coil vertically downward. Figure 4.6 was generated using the "g3view" software included with PENELOPE.

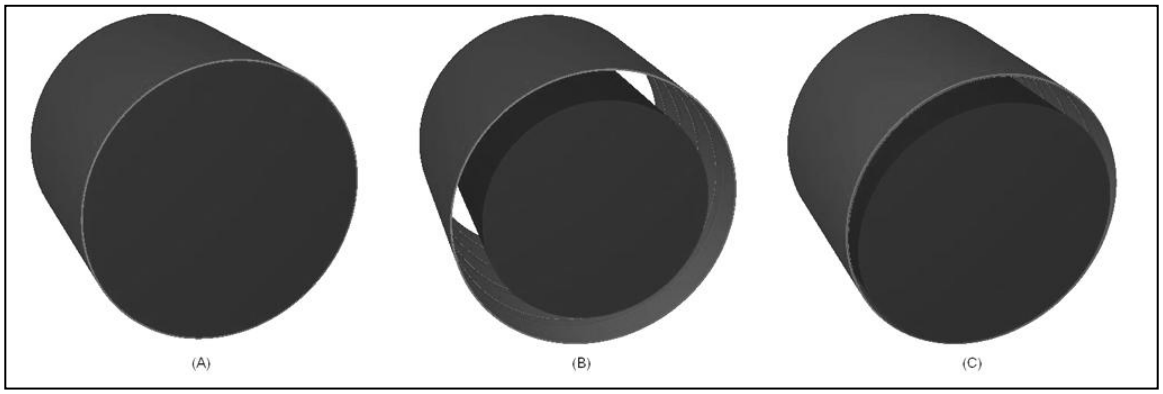


**Figure 4.6 - Phantom geometries used for coil simulations: (A) No air gap between water phantom and coil, (B) a uniform air gap between the water phantom and the RF coil (1cm gap shown) and (C) an air gap which begins at 1cm at the top of the phantom and decreases to zero at the bottom of the phantom to simulate patient sag.**

### 4.3.4 Monte Carlo simulation of magnetic field effects on RIC

With respect to an integrated linac-MR system, the RF coils will be in a constant magnetic field which may alter the RIC by altering the movement of charged particles. The effect of magnetic fields was calculated by immersing the phantoms in a uniform magnetic field. A total of six scenarios involving two magnetic field orientations (parallel and perpendicular to the photon beam direction) and three magnetic field strengths (0.5, 1.0 and 1.5 Tesla) were simulated. The three planar geometries from § 4.3.2.1 and the cylindrical coil geometries of Figure 4.6 were

used, but the coil geometry with the 2cm uniform gap was omitted because of the similarity in results to the 1cm uniform gap. The phase space file of the beam was the same as in the previous simulations.

### 4.3.5 Aluminum surface coil with Teflon buildup

To experimentally validate the buildup method on a more realistic geometry, a simple aluminum surface coil was constructed. Figure 4.5c shows the measurement setup used for investigating the RIC reduction in this aluminum surface coil using Teflon buildup. The aluminum surface coil was cut from a 1.6 mm thick aluminum plate. The coil's resonant frequency and its impedance at resonance were determined to be ~ 8.85 MHz, and 43 Ω, respectively. Backscatter material was 2.5 cm of Styrofoam placed on top of 7 cm of solid water. This was used to simulate an air gap between the coil and the patient. The measurement setup is the same as that described in section 4.3.2.1, with the exception of the SSD for these measurements being 116.2 cm. The data was acquired by A. Ghila, but is presented herein because of its implications to this work.

### 4.3.6 Proof of concept: imaging with buildup applied

The linac-MRI system used in these experiments is that described by Fallone *et al* [Fallone, et al., 2009]. The RF coil used in this imaging experiment was a solenoid coil with 14 turns of copper wire. The wire is wound onto the outside of a plastic cylinder with inner and outer diameters of 28.0 mm and 32.5 mm, respectively. The total outer diameter of the coil, including the copper windings is approximately 36.3 mm. The phantom was an acrylic rectangular cube,

15.95x15.95x25.4 $mm^3$, with 3 holes of diameters 2.52, 3.45 and 4.78 mm drilled into it. The cube was then placed in a 22.5 mm diameter tube and filled with a 10mM solution of $CuSO_4$. This arrangement fills the holes in the cube with the $CuSO_4$ creating three circular signal regions in the MRI image (Seen in Figure 4.1 above). The coil's active components are outside the volume of the solenoid and placed outside the radiation beam. Currently we do not have the ability to construct a specialized RF coil with the buildup material incorporated into the design, so for this proof of concept experiment a cylindrical Teflon buildup was constructed in-house to fit around the solenoid coil. The buildup consists of two halves of a hollow Teflon cylinder of 18.5 mm thickness; put together they form an annulus which is placed around the solenoid coil. The inner diameter of the annulus is approximately 37 mm.

A standard gradient echo sequence was used in all experiments. Images were firstly obtained with the linac not producing radiation. The same imaging was then repeated with the linac producing radiation at 250 monitor units per minute (MU/min, i.e. the dose rate). These two scenarios were performed with and without the presence of buildup, yielding four imaging conditions. Five images were taken in each condition to assure reproducibility and to provide statistical information. The resulting images were then analyzed by calculating the SNR of the image. The SNR was calculated by taking the mean of the signal divided by the standard deviation of the background noise. For each of the 4 imaging conditions the mean and standard deviation of the five SNR values were calculated.

## *4.4 RESULTS*

### 4.4.1 Monte Carlo simulation algorithm validation

Results of comparing the measurements and simulations described in section 4.3.1.2 are shown in Figure 4.7. The measured data were calculated using equation (4.2) to reduce the effect of air ionizations. The simulated data agreed very well with the measured data, thus validating the accuracy of the simulation algorithm.

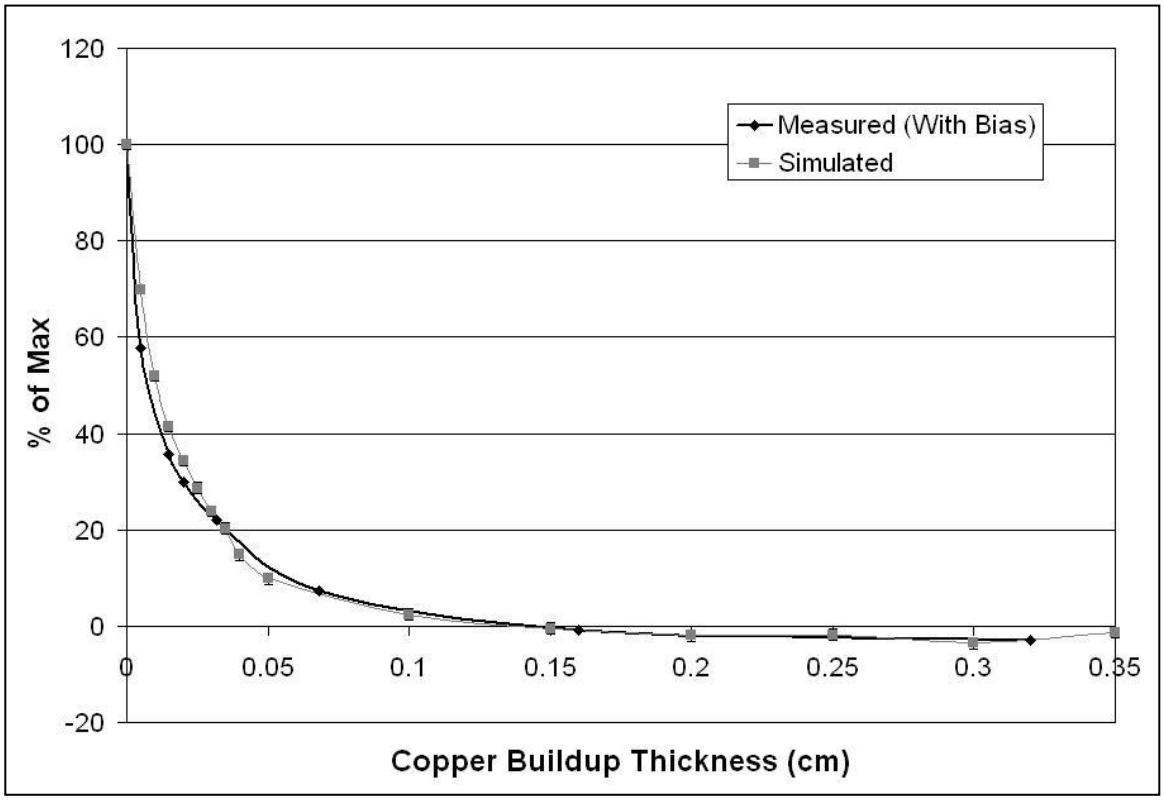


**Figure 4.7 - Validation of Monte Carlo RIC algorithm through comparison of measurements and simulations. The measured data were acquired with the buildup and backscatter biased at ± 10V. Both the measured and simulated data are normalized at zero buildup thickness.**

### 4.4.2 Confirmation of buildup method for RIC removal

#### 4.4.2.1 Detector-buildup combinations

The results for the measurements described in sections 4.3.2.1.1, 4.3.2.1.2 and 4.3.2.1.3 are shown in Figure 4.8. The experimental uncertainty in the measured RIC, in most cases, was smaller than the size of the markers, so the error bars are not visible. The corresponding simulated RIC reduction curves are shown in Figure 4.9. Both measured and simulated curves follow very similar trends for all detector/buildup combinations. Figure 4.8 and Figure 4.9 clearly show that by using buildup, thus establishing electronic equilibrium in the detector plates, the RIC can be completely removed if the buildup and detector materials are identical. This occurs for the case of the copper detector/copper buildup scenario where the RIC amplitude is reduced to zero. The RIC for the copper detector/copper buildup case falls below zero values beyond a certain buildup thickness. The measurements and simulations were not directly compared in these figures because these measurements did not use the dual biased detector approach to reduce the effect of air ionizations, so there are inherent differences in the setups which would lead to unfair comparison.

In fact, the buildup and back scatter are placed at zero volts while the detector is floating at the amplifier's input. This appears to cause some of negative charges produced within the small air gaps to be collected by the detector. The negative RIC is nearly reduced to zero value when using the dual bias method (section 4.4.1).

Using 1.2 cm of Teflon buildup the RIC in the aluminum detector is reduced by approximately 90% in the measurements and approximately 95% in simulations, while using the same amount of Teflon with the copper detector the RIC is reduced by approximately 80% in the measurements and approximately 85% in the simulations.

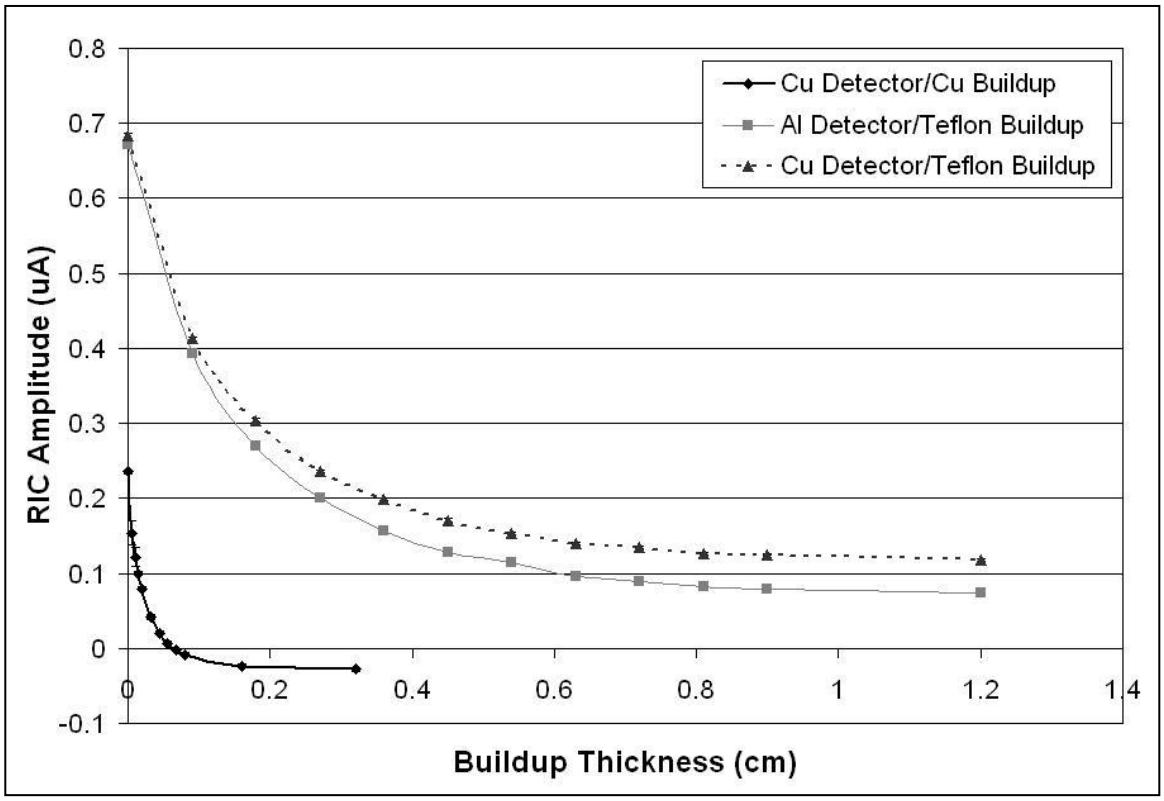


**Figure 4.8 - Measurement results for the reduction of RIC with buildup in the various detector/buildup combinations.**

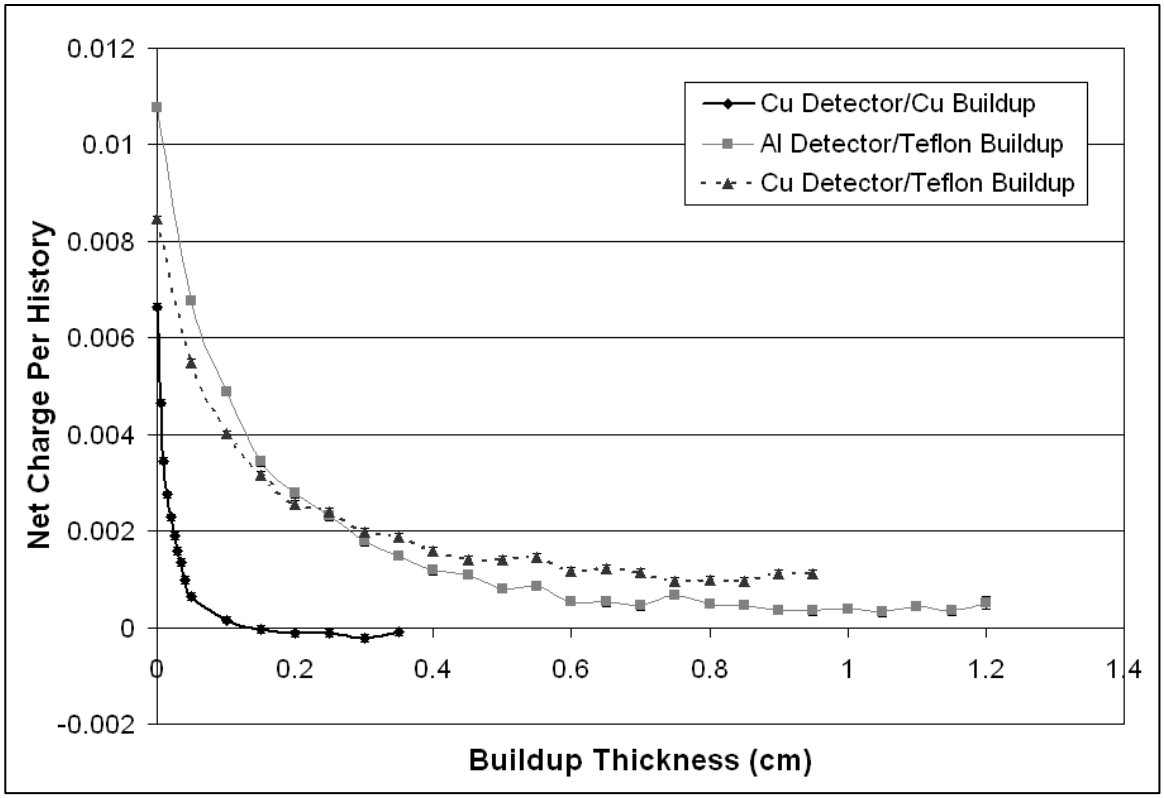


**Figure 4.9 - Simulation results for the reduction of RIC with buildup for the various detector/buildup combinations used.**

### 4.4.3 Cylindrical coil geometry simulations: effect of air gaps

These simulations examined the efficacy of buildup for RIC reduction in cylindrical geometries. Three different phantom geometries that used Teflon buildup were illustrated in Figure 4.6 while the case for Figure 4.6b was repeated with a 2 cm uniform air gap. The simulations results are shown in Figure 4.10 as the net charge retained in the coil conductor per simulation history. The air gaps between the RF coil and the water phantom have two main effects: firstly, air gaps increase the RIC amplitude of the bare coil and secondly, the effectiveness of the buildup in reducing RIC is severely compromised. These two effects are more severe when the air gap uniformly surrounds the phantom. In this situation, the RIC amplitude is slightly larger for 2 cm than 1 cm air gap. When the air gap

between the coil and the phantom decreases from top to bottom, these two effects are somewhat reduced but the RIC does not reach negligible levels even for really thick buildup. The buildup method is still highly effective when there are no air gaps between the coil and phantom, reducing the initial RIC amplitude by ~ 85%.

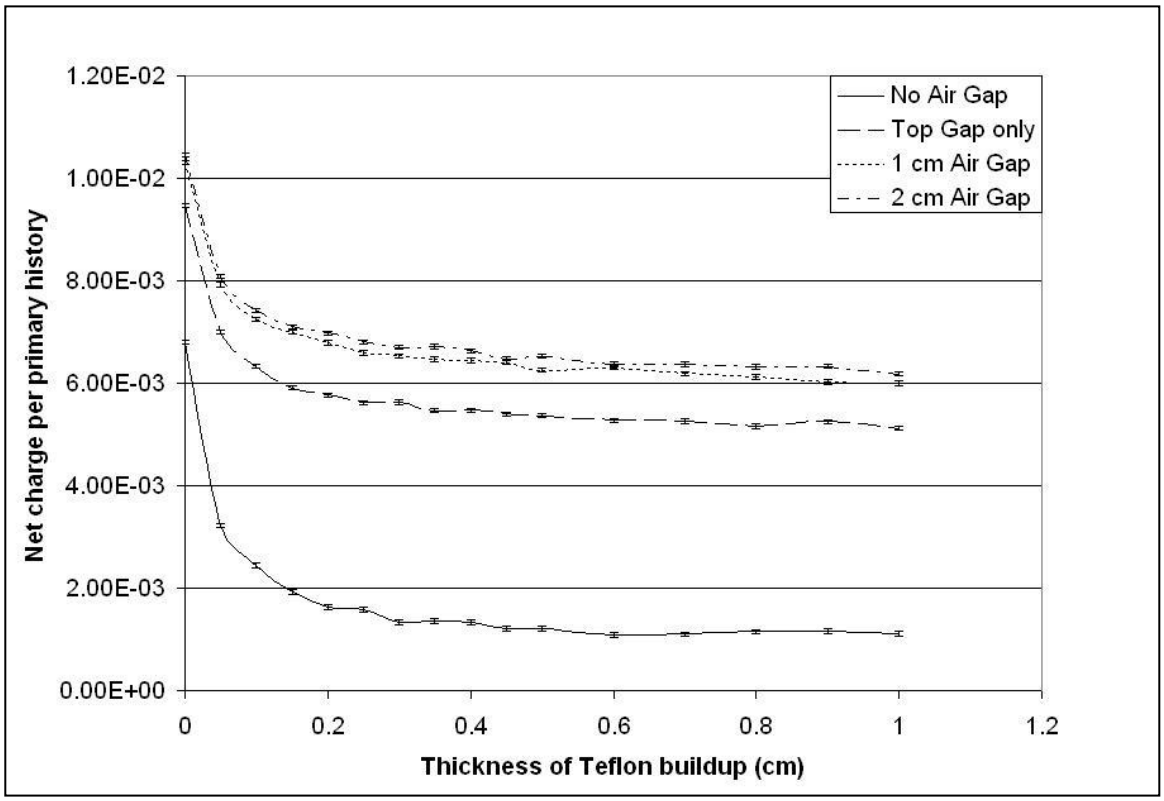


**Figure 4.10 - Monte Carlo simulation of RIC reduction through the use of Teflon buildup in a cylindrical RF coil. Four different scenarios were examined: (1) no air gap between the coil and the phantom, (2) air gap decreases from top to bottom of the phantom, (3) a uniform 1 cm air gap surrounding the phantom and (4) a uniform 2 cm air gap surrounding the phantom**

### 4.4.4 Monte Carlo simulation of magnetic field effects on RIC

#### 4.4.4.1 Planar Geometry

The RIC simulation for planar conductor and buildup geometry in uniform magnetic field are shown in Figure 4.11. Overall behaviour of the RIC as a function of increasing buildup thickness is similar to the case of no magnetic

field, in both magnetic field orientations. In the 0.5 T perpendicular magnetic field case, the RIC is nearly the same as in the case of no magnetic field. However, as the magnetic field in this orientation is increased, the RIC is reduced compared to the case of no magnetic field. The magnitude of RIC is the smallest for the 1.5 T perpendicular magnetic field case. For parallel magnetic field, the effect of field strength is not significant. In this case, the RIC amplitude is uniformly decreased by approximately 10% regardless of the field strength. Overall the presence of magnetic field does not severely alter the effectiveness of the buildup method of RIC reduction in planar coil conductors. The detector size (7.5 x 7.5 $cm^2$) is smaller than the area of the buildup plates and the backscatter materials. This creates a thin air gap between the buildup and the backscatter plates that lies outside the detector area. This thin air gap may be responsible for the small magnetic field effects that are observed in the simulated RIC.

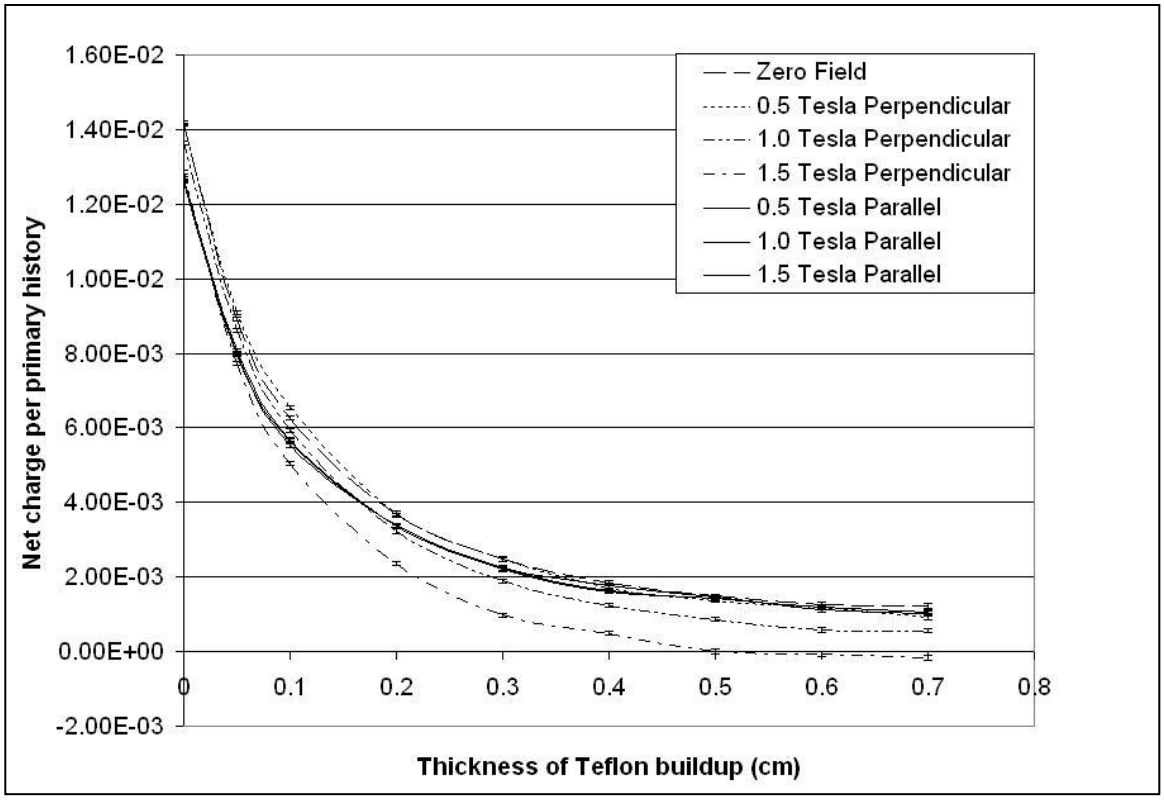


**Figure 4.11 - The RIC simulation results for the planar geometry in the presence of parallel and perpendicular orientation of uniform magnetic fields. In each orientation of magnetic field, three values of uniform magnetic field are simulated to examine the effect of magnetic field strength on the reduction of RIC in an aluminum detector by Teflon buildup**

### 4.4.4.2 Cylindrical coil geometry

The RIC simulation results using the solenoid coil geometry of Figure 4.6 in the presence of parallel and perpendicular uniform magnetic fields of varying strengths are shown in Figure 4.12. In the coil geometry with no air gap between the coil and water (Figure 4.6a), we see essentially no change in the behavior of RIC as a function of Teflon thickness from the zero magnetic field case, aside from some small fluctuations at the initial amplitude (Figure 4.12a). The absence of any air gap in this geometry means the ejected electrons from the detector are always travelling in either Teflon or water medium. Since the electron path length

is so much smaller in medium, these small paths will not be significantly altered by the presence of a magnetic field.

When there is a uniform, 1 cm air annulus between the coil and the water (Figure 4.6b), the initial, zero buildup thickness RIC values are larger in the presence of magnetic fields, and approach a higher minimum value than the no air gap case (Figure 4.12b) – similar to the effects seen without the presence of magnetic field. There may be a small magnetic field effect in the range of 0.1 to 0.4 cm Teflon thicknesses. In this range, the RIC in the presence of magnetic field is slightly larger than the case without magnetic field. There appears to be little effect due to magnetic field strength and direction at the minimum value of RIC which is obtained at higher thicknesses of the Teflon buildup. The effect of magnetic field may be more pronounced for larger air gaps in the range of 0.1cm to 0.4 cm thickness of Teflon, although larger air gaps may be undesirable from an MR-imaging perspective.

In the third coil geometry (Figure 4.6c) where the air gap is only present between the top portion of the coil and water, the RIC trend is similar to that seen in the previous case; however, the minimum value of the RIC obtained at large thickness of Teflon buildup is lower in this case (Figure 4.12). It should be noted that the trends observed in Figure 4.12 are similar to those observed in Figure 4.10 for the case of no magnetic field. Thus the presence of a magnetic field, irrespective of the direction and the strength of the magnetic field, does not produce noticeable differences in the RIC.

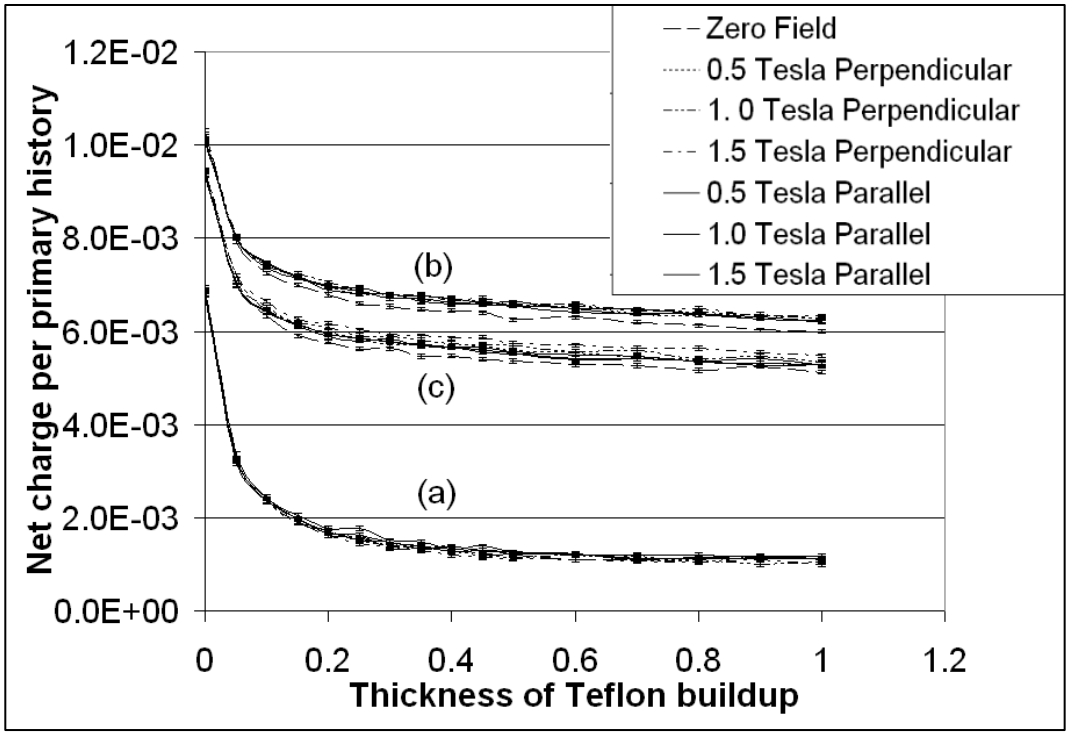


**Figure 4.12 -- The results of RIC simulation in the presence of parallel and perpendicular magnetic fields as a function of thickness of Teflon buildup. The (a), (b), and (c) labels refer to the three coil geometries described in Figure 4.6.**

### 4.4.5 Aluminum surface coil with Teflon buildup

Figure 4.13 shows that reducing the RIC in an aluminum surface coil with the application of Teflon buildup is effective. The RIC amplitude is reduced by 92% of its original value using only 0.9 cm of Teflon buildup. The initial RIC amplitude is small compared to the planar detector measurements using aluminum for a detector (Figure 4.8) due to the surface coil's smaller irradiated surface area.

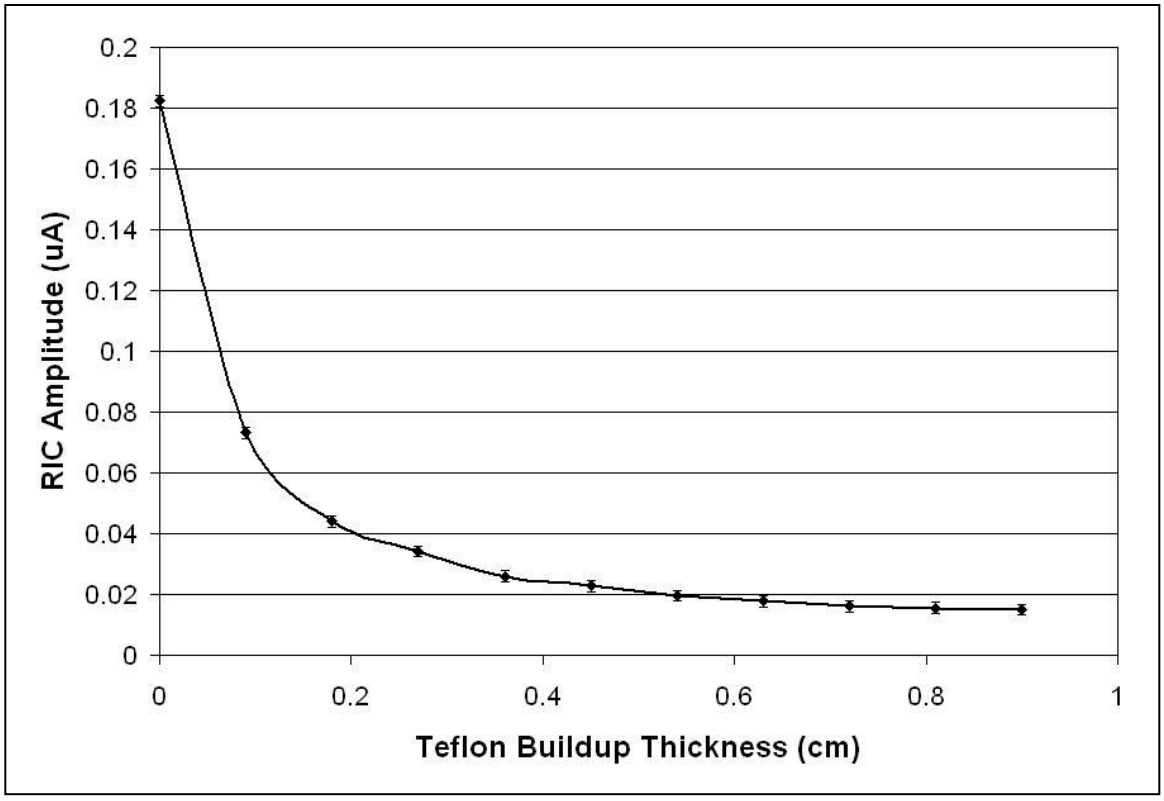


**Figure 4.13 - Reduction of RIC in an aluminum surface coil through the application of Teflon buildup. The initial RIC amplitude is reduced by 92% with 0.9 cm of Teflon.**

### 4.4.6 Proof of concept: imaging with buildup applied

Because the addition of the Teflon buildup changes the loading of the RF coil, and hence the tuning, matching and shimming, the cases of buildup and no buildup without radiation must be compared to their respective radiation on conditions. To accomplish this, for each case, i.e., buildup and no buildup, the SNR calculated for the images acquired in the presence of the radiation beam are presented as the percentage of the original SNR in the images acquired with no radiation present. In the case with no buildup the percentage of the non-radiation SNR is 89%, representing an 11% loss in SNR due to RIC. In the case where the buildup is present, the percentage of non-radiation SNR increases to 95%, representing only a 5% loss in SNR. This shows that 55% of the SNR lost was recovered through

the use of the Teflon buildup material. The k-space data for the two imaging scenarios taken with the radiation striking the RF coil are presented, using the same window and level settings, in Figure 4.14. The intensity of the lines in the k-space was not eliminated but was reduced by using the rudimentary and non-ideal buildup (Figure 4.14). While the visual difference in the line intensities seen in Figure 4.14 is subtle, the SNR recovery shows the buildup was effective.

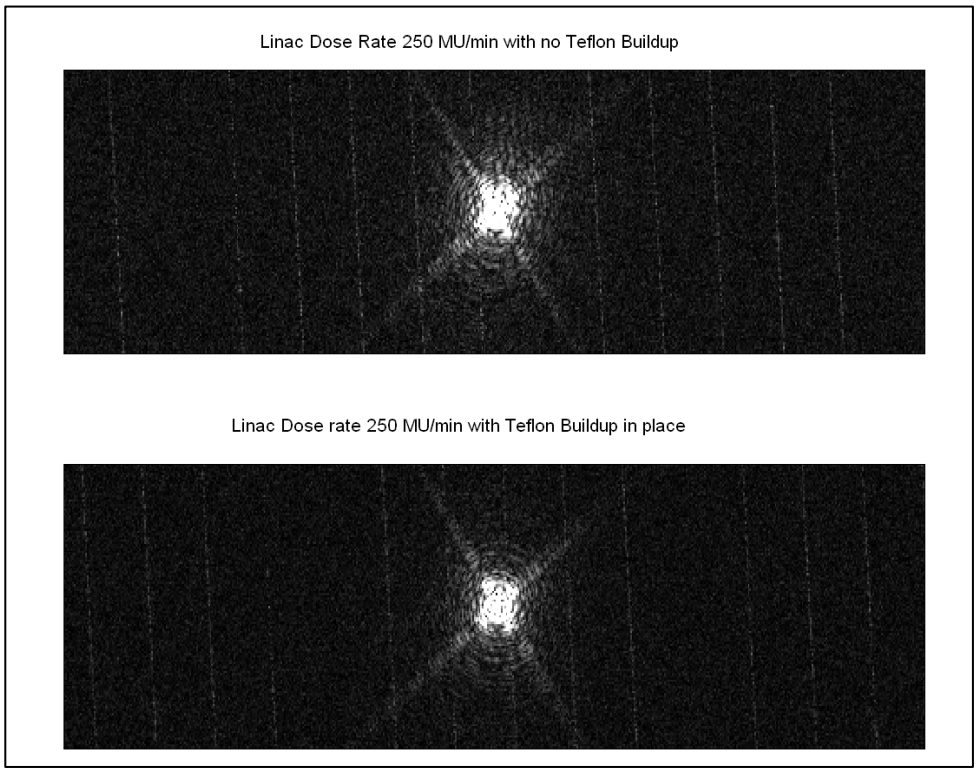


**Figure 4.14 - K-space data for images acquired with the linac producing radiation at 250 MU/min and incident upon the coil with no buildup (top image) and with Teflon buildup in place (bottom image). The same window and level was used to display each image.**

## *4.5 Discussion*

Monte Carlo simulations are very useful to study the RIC effect in the cylindrical coils. However, the implementation of RIC calculation in Monte Carlo needed verification similar to the one shown in Figure 4.7. The amplitude of both the

measurements and the simulations is reduced to zero at the same thickness of copper buildup of ~0.15 cm. Assuming the water buildup depth of 1.5 cm for the 6 MV spectrum, and copper density of 8.9 g/cm$^3$, 0.15 cm thick copper appears reasonable to establish electronic equilibrium based on density scaling. The small negative values of the RIC beyond 0.15 cm copper thickness, indicating slightly more electrons entering than leaving the conductor, are indicative of the quasi-electronic equilibrium that exists beyond the 0.15 cm copper thickness, i.e. interacting beam fluence is slightly lower in the detector than in the identical thickness of buildup immediately above the detector.

We measured and simulated the RIC in an experimental setup that comprises a planar geometry for the detector and buildup in order to understand its origin. As the thickness of applied buildup increases, the RIC amplitude decreases; thus indicating electronic disequilibrium in the detector as the cause of RIC. Electronic equilibrium was only truly obtained in the copper detector with copper buildup measurements, so the RIC amplitude was only reduced to zero for this case (Figure 4.8 and Figure 4.9). To establish electronic equilibrium a sufficient number of low energy electrons must be ejected from the buildup and be stopped in the detector, in order to replace the electrons ejected from the detector. If the density of the buildup is substantially different than that of the detector, electronic equilibrium will never be established at any buildup thickness; this is seen in the copper detector and Teflon buildup measurements, where the RIC amplitude is reduced to a non-zero value of about 20% of the initial measured RIC amplitude (Figure 4.8) and 15% of the initial simulated RIC

amplitude (Figure 4.9). When the density difference between the detector and buildup is smaller, as seen in the aluminum detector/Teflon buildup scenario, a greater reduction in the RIC can be achieved; the RIC amplitude is reduced to 10% of its measured initial value (Figure 4.8) and 5% of its simulated initial value (Figure 4.9). It is expected that the reductions of RIC seen in the three scenarios shown in Figure 4.8 and Figure 4.9 will all be sufficient to largely eliminate the SNR loss seen in the MR images shown in § 4.2.1. However, the copper or aluminum buildup material is impractical since it will act as an RF shield for the transmitter coil, and could have problems related to eddy currents. Therefore, covering the conductor of the receive RF coils with an insulator of sufficiently close density to the conductor is a good choice to achieve effective reduction in the RIC.

The early simulations examining the four cylindrical coil geometries shown in Figure 4.6 illustrate the importance of minimizing the air gap between the coil and the patient in order for buildup to effectively reduce RIC (Figure 4.10). This condition is easily satisfied when surface coils are used as they will sit directly on the patient; however, the solenoid and birdcage coils that are often used with typical solenoid, superconducting MRI scanners are not usually in direct contact with the patient and RIC could be problematic in these cases. There are a few solutions to this problem: a small amount of solid water or some other plastic could be placed on the bottom side of the coil conductor, between the coil and patient, to act as a backscatter medium thus helping to maintain electronic equilibrium in the coil; another suitable solution may involve the use of a

Helmholtz-style RF coil in which the two coils are placed outside the radiation field, thus producing no RIC. Synchronization between the radiation pulses and image sequence such that the read gradient is consistently outside the radiation pulse may also be used; however, it may increase MR imaging times and that may not be useful in practice.

The effect of magnitude and direction of the magnetic field on the RIC of planar coils (Figure 4.11) have small differences between the parallel and perpendicular orientation of the magnetic field. In the parallel magnetic field, the amplitude of the RIC in the planar conductors is reduced uniformly by about 10% compared to zero magnetic field case. The 0.5 Tesla perpendicular field strength simulation showed very little difference compared to the zero-field simulation; however, the 1.0 Tesla perpendicular field showed a quicker decrease in RIC with applied buildup and also decreased to a smaller minimum value compared to the zero-field and parallel field cases. Finally, with a 1.5 Tesla perpendicular field the RIC was reduced even more quickly (i.e. with less buildup material) and was completely removed (i.e. decreased to zero), when compared to the zero-field simulation. The results suggest that the amount of buildup necessary with magnetic fields present is similar to zero-field amount, except possibly at high perpendicular magnetic fields where there is a modest decrease in buildup required. Overall, the magnetic field should not reduce the effectiveness of applying buildup to minimize RIC effects in planar RF coil geometries, such as surface coils.

In cylindrical geometries the most important factor remains the air gaps between the coils and the patient. The effect of varying the direction and strength of magnetic fields on RIC reduction in these geometries is minimal compared to the effect of introducing air gaps between the coil and patient. There was a slight reduction, seen in Figure 4.12c, in the effectiveness of RIC reduction seen when an asymmetric air gap was placed between the top of the coil and the top of the water volume (Figure 4.6c) and a strong (1.5 Tesla) perpendicular field was applied. However, the difference between the 1.5 Tesla perpendicular field and the zero-field simulation for this coil geometry is much less than the effect of introducing the asymmetric air gap to begin with (Figure 4.10). It is interesting to speculate that the magnetic field effects may be more noticeable if the air gaps between the coil and the patient is increased. In these cases, the RIC behavior around 0.1cm to 0.4 cm buidup thickness may become more dependent on the direction and the magnitude of the magnetic field.

Figure 4.13 indicates that Teflon is a suitable material for reducing RIC in coils with an aluminum conductor, as the initial RIC amplitude was reduced by 92% using 0.9 cm of Teflon buildup. It should be noted that the backscatter material (Styrofoam plus solid water) was not the same as the aluminum detector material in this case, but this had little effect on the RIC reduction. Of all the materials studied, aluminum for the coil conductor and Teflon for the buildup appear to be the best suited for reducing RIC to negligible levels in RF coils.

A simple imaging experiment using an in-house constructed buildup showed that some of the SNR lost due to RIC can be recovered by applying

buildup to the RF coil. Using a very basic buildup we were able to recover 55% of the SNR lost.

## V. CONCLUSIONS

This investigation demonstrates that the RIC can be reduced with the appropriate combination of coil conductor and buildup. Our results indicate that about 1 cm of Teflon wrapped around an aluminum RF coil would essentially eliminate radiation induced currents in the coil. This method of RIC removal can effectively be applied to practical RF coil geometries and the presence of magnetic fields. In cylindrical coil geometries, the air gap is more important than the presence of the magnetic field. In planar geometries the amount of buildup material required to achieve adequate RIC reduction is similar to that required with no field present. The RIC simulation is a useful tool for practical coil design where radiation effects must be considered.

Future work will involve building RF coils with buildup for use on our prototype linac-MR. Also, the dosimetric effects of having RF coils including buildup in the beam path need to be investigated. As an alternative to the buildup RIC removal method, another method using image post-processing is being investigated, which would remove the RIC artefact from the MR data.

## REFERENCES

Burke, B., Fallone, B., & Rathee, S. (2010). Radiation induced currents in MRI RF coils: application to linac/MRI integration. *Physics in Medicine and Biology, 55*, 735-746.

Burke, B., Lamey, M., Rathee, S., Murray, B., & Fallone, B. (2009). Radio frequency noise from clinical linear accelerators. *Physics in Medicine and Biology, 54*, 2483-2492.

Fallone, B., Murray, B., Rathee, S., Stanescu, T., Steciw, S., Vidakovic, S., et al. (2009). First MR images obtained during megavoltage photon irradiation from a prototype integrated linac-MR system. *Medical Physics, 36* (6), 2084-2088.

Gross, B. (1980). *Radiation-induced charge storage and polarization effects.* (G. M. Sessler, Ed.) Berlin Heidelberg New York: Spinger-Verlag.

Lamey, M., Burke, B., Blosser, E., Rathee, S., De Zanche, N., & Fallone, B. (2010a). Radio frequency shielding for a linac-MRI system. *Physics in Medicine and Biology , 55*, 995-1006.

Rieke, V., Ganguly, A., Daniel, B. L., Scott, G., Pauly, J. M., Fahrig, R., et al. (2005). X-ray compatible radiofrequency coil for magnetic resonance imaging. *Magnetic Resonance in Medicine ,* 1409-1414.

Salvat, F., Fernandez-Varea, J., & Sempau, J. (2009). *PENELOPE-2008, A code system for Monte Carlo simulation of electron and photon transport.* Barcelona: OECD Nuclear Energy Agency.

Sessler, G. M. (1980). *Topics in applied physics volume 33: Electrets.* (G. M. Sessler, Ed.) Berlin Heidelberg New York: Spinger-Verlag.

St. Aubin, J., Steciw, S., & Fallone, B. (2010b). An integrated 6 MV linear accelerator model from electron gun to dose in a water tank. *Medical Physics , 37*, 2279-2288.

# 5 Effect of radiation induced current on the quality of MR images in an integrated linac-MR system

*A version of this chapter has been published: B. Burke, K. Wachowicz, B. G. Fallone and S. Rathee "Effect of radiation induced current on the quality of MR images in an integrated Linac-MR system," Med. Phys.* ***39****, 6139-6147 (2012)*

## *5.1 Introduction*

Our research group has integrated a linear accelerator (linac) with a magnetic resonance imaging (MRI) system [Fallone, et al., 2007; Fallone, et al., 2009]. This system will provide real-time, intra-fractional images [Yun, et al., 2012] with tumour specific contrast to allow significant reductions in margins for the planning target volume. As a result, both improved normal tissue sparing and dose escalation to the tumour will be possible, which are expected to improve treatment outcomes.

The RF coils used in MR imaging are exposed to the pulsed radiation of the linac in the integrated linac-MR system. This has been shown to result in instantaneous currents being induced in the MR coils – called radiation induced current (RIC) [Burke, et al., 2010]. These extraneous currents have the potential to adversely affect MR imaging by distorting the RF signal being measured by the RF coils. Our more recent results have shown that the RIC signal in RF coils can be reduced with the application of appropriate buildup material to the coils (§ 4). This buildup method was effective with planar or cylindrical coil geometries and was unhindered by the presence of magnetic fields. This work explores another method for RIC removal that does not involve altering the RF coils, but instead

uses image processing techniques. Recently published work by Yun *et al* discuss the importance of imaging signal-to-noise (SNR) for real-time tumour tracking [Yun, et al., 2012] and this provides the motivation for the use of a post-processing algorithm to recover some of the SNR lost due to RIC.

In this work, we image phantoms in the linac-MR system in the presence of pulsed radiation from the linear accelerator. These experiments clearly demonstrate the presence of RIC in the MRI raw data, i.e. k-space. The purpose of this work is to: (a) visualize the RIC in MRI raw data and determine its effect on the MR image quality, specifically the SNR (b) examine the effect of linac dose rate, in monitor units (MU) per minute, on the SNR degradation caused by the RIC, (c) examine the RIC effect on different MRI sequences, (d) examine the effect of altering the MRI sequence timing, specifically the repetition time (TR), on the visual appearance of the RIC in MRI raw data, and (e) use post processing methods to remove the unwanted RIC signal from the MR images.

## *5.2 Materials and Methods*

The linac-MRI system used in these experiments is that described by Fallone *et al* [Fallone, et al., 2009] and shown schematically in Figure 5.1. The system is comprised of a 0.22 Tesla bi-planar magnet from MRI Tech Co. (Winnipeg, MB, Canada) and a 6 MV linear accelerator with its beam directed to the imaging volume of the magnet. The x-ray beam direction is perpendicular to both the main magnetic field and the superior-inferior orientation of the patient. The maximum gradient strength of the MR system is specified as 40 mT/m and the MR system is controlled using a TMX NRC console (National Research

Council of Canada, Institute of Biodiagnostics, Winnipeg, MB, Canada). The console software is Python-based (Python Software Foundation, Hampton, NH, www.python.org) to allow full user control of the development and modification of pulse sequences. Analogic (Analogic Corporation, Peabody, MA) AN8295 gradient coil amplifiers and AN 8110 3 kW RF power amplifiers are used.

The linac components are composed of salvaged parts from a decommissioned magnetron-based Varian 600C system, which include the straight-through waveguide (without bending magnet). The distance of the linac target to the magnet center is 80 cm. Presently, the MV x-ray beam has primary collimators and the final prototype design will include secondary collimators and the multileaf collimator (MLC) [Fallone, et al., 2009].

Two RF coils were used in the imaging experiments. The first was a small, ~3 cm diameter solenoid coil with 14 turns of wire. The tuning and impedance matching of this coil is accomplished by variable capacitances and it contains an integrated pin-diode transmit/receive switch. All active components are outside the volume of the solenoid such that these can be placed outside the radiation beam. The second coil was a 10 cm diameter solenoid coil containing 5 concentric rings made of 0.64 cm diameter copper pipe. The tuning of the coil is accomplished by a variable capacitance while the impedance matching is accomplished with a variable inductor. As with the smaller coil, this coil contains an integrated pin-diode transmit/receive switch with the active components residing outside the solenoid volume. Both coils were constructed by NRC and resonate nominally at the appropriate frequency of 9.3 MHz for the 0.22T MRI.

The phantom used in the smaller coil was an acrylic rectangular cube, 15.95x15.95x25.4 $mm^3$, with 3 holes of diameters 2.52, 3.45 and 4.78 mm drilled into it. The cube was then placed in a 22.5 mm diameter tube and filled with a 10mM solution of $CuSO_4$. This arrangement fills the holes in the cube with the $CuSO_4$ creating three circular signal regions in the MRI image [Fallone, et al., 2009]. The phantom used in the 10 cm diameter coil consisted of four tubes of 27 mm diameter filled with a solution of 61.6 mM NaCl and 7.8 mM $CuS0_4$. The tubes were stacked into a 2x2 matrix arrangement and held together with an adhesive tape. This arrangement again created four circular signal regions in the MRI image [Lamey, et al., 2010a].

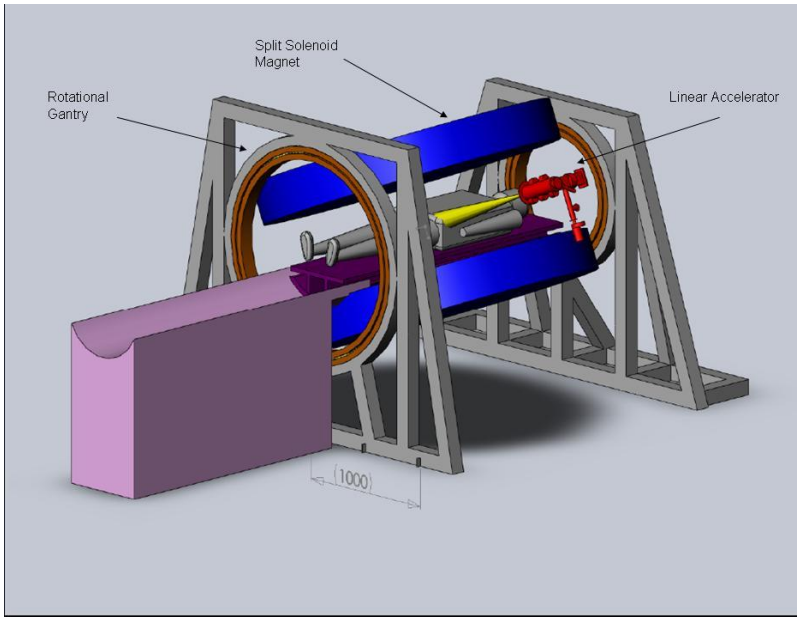


**Figure 5.1 - Schematic diagram of linac-MR system showing the split solenoid MR magnet (blue), the linear accelerator (red) and the rotational gantry (grey)**

### 5.2.1 Effect of RIC and linear accelerator dose rate on MR images

This experiment was designed to determine the effect of RIC on the SNR in MRI images including the impact of the linac dose rate. A standard gradient echo sequence was used in all experiments. For the phantom in the smaller coil the imaging parameters were as follows: slice thickness – 5 mm; acquisition size – 512 (read) x 128 (phase); field of view (FOV) – 50 x 50 $mm^2$; repetition time (TR) – 300 ms; echo-time (TE) – 35 ms; flip angle – 60°; no signal averaging. For the phantom used in the larger coil the imaging parameters were as follows: Slice thickness – 3.5 mm; acquisition size – 256 (read) x 128 (phase); FOV – 100 x 100 $mm^2$; TR – 300 ms; TE – 35 ms; flip angle - 90°; no signal averaging. For the small coil, 512 points in the read direction was chosen for easy visualization of the RIC artefact; more points in the read direction means a longer acquisition window, which in turn leads to more radiation pulses being present during signal acquisition. The flip angles were chosen to provide maximum signal in both cases.

Images of both phantoms were initially obtained with the linac not producing radiation. The same imaging was then repeated with the linac producing radiation at 50, 100, 150, 200, 250 monitor units per minute (MU/min, i.e. the dose rate). The imaging experiments in the presence of the radiation beam were further divided into two parts. In the first experiment, the radiation was directly incident on the RF coils. In the second experiment, a lead block was placed in the beam path to completely attenuate the radiation from reaching the

RF coil. This was done to ensure that any effect seen in the MR images was caused only by the direct irradiation of the coils, resulting in RIC in the coil, and not due to any residual RF noise. The residual RF noise, if it exists, will still reach the coil even if the x-ray beam was completely attenuated by the lead block. The method and effect of RF shielding for this system has been previously described [Lamey, et al., 2010a]. This means that a total of 11 (beam off, beam on at five different dose rates, beam on but blocked at the same five dose rates) different imaging conditions were examined for each phantom and coil combination.

Five images were taken in each condition to assure reproducibility and to provide statistical information. The resulting images were then analyzed firstly by calculating the SNR of the image and secondly, by examining the k-space data associated with each image, using appropriate window and level, to visualize the RIC artefact (See Figure 5.5). The SNR was calculated by taking the mean of the signal divided by the standard deviation of the background noise. For each of the 11 imaging conditions the mean and standard deviation of the five SNR values were calculated.

### 5.2.2 Dependence of RIC artefact on imaging sequence

The effect of the MR imaging sequence on the RIC artefact was examined by repeating the imaging experiments from section 5.2.1, using a spin echo sequence and a balanced steady-state free precession (bSSFP) sequence instead of the gradient echo sequence used in 5.2.1. This was done to see if the SNR loss shown for the gradient echo sequence would also be seen in other sequences. The

small coil described above was used for both sequences. SNR was calculated as in 5.2.1.

The imaging parameters for the spin echo sequence were: slice thickness – 5 mm; acquisition size – 256 (read) x 128 (phase); FOV – 50 x 50 $mm^2$; TR – 300 ms; TE – 30 ms; no signal averaging; flip angle 90°. The imaging parameters for the bSSFP sequence were: slice thickness – 5 mm; acquisition size – 128 (read) x 128 (phase); FOV – 50 x 50 $mm^2$; TR – 18 ms; no signal averaging; flip angle - 60°.

### 5.2.3 Dependence of RIC artefact on imaging parameter TR

The next imaging experiment was done by keeping the linac dose rate constant at 250 MU/min and the imaging parameters identical to those in section 5.2.1, except for the repetition time, TR, which was changed. These experiments were only performed with the smaller coil and the gradient echo sequence was used. Images were acquired at TR values of: 299, 299.8, 299.9, 300, 300.1, 300.2, 301, 302, 303, 304 and 305 milliseconds. This investigation examined the relationship between the RIC artefact and the MR sequence timing. The SNR and k-space data were again examined.

### 5.2.4 Removal of RIC artefact from MR data using post-processing

Finally, the software program MATLAB (The MathWorks, Inc., Natick, MA) was used as a post-processing tool in an attempt to remove the RIC artefact from the image k-space data and restore some of the SNR lost due to RIC. The

algorithm is similar in application to an adaptive filter used to removed speckle noise from synthetic aperture radar images as discussed by Russ [Russ, 2002, p. 165], which uses a neighbourhood comparison of pixel brightness, with a threshold based on the average and standard deviation, and replaces those above the threshold with a weighted average value of the neighbourhood.

The algorithm searches pixel by pixel for anomalous signal spikes in k-space and then removes them. These spikes are found by searching the k-space data for pixels with intensities above a global threshold value; the global threshold value was the average background plus three standard deviations. The average background and standard deviation are determined from a group of pixels near the edge of the k-space image (thus ensuring that it is background).

Once an anomalous pixel is found, its magnitude is then compared to the mean pixel magnitude in the local neighbourhood surrounding the pixel to determine whether the pixel resides in a background region (i.e. towards the edges of k-space) or in a signal region (near the centre of k-space). If the pixel's value is larger than the local average (plus 3 standard deviations) then the anomalous pixel lies in the background regions, otherwise it lies in the signal region. In other words, in order for the pixel to be replaced, its intensity has to be larger than both the global threshold and local average before it is replaced. The number of pixels in the local neighbourhood used for comparison in this work was the 5x5 square centered on the point of interest. If the algorithm determines that the anomalous pixel is in a background region, the pixel value is changed to that of the average

background. If the algorithm instead determines that the anomalous pixel is in a signal region, then no action is taken.

It is obvious that this algorithm will not eliminate all RIC spikes from the k-space data, as it will not be able to discern between RIC signal and the MR signal near the center of k-space. However, this may be acceptable as the RIC spikes near the center of k-space have a minimal effect on SNR because the spikes are sparsely distributed compared to the MR signal. Also, the magnitude of the RIC noise spikes is small compared to the MR signal near the center of k-space. The MR image was reconstructed from the processed k-space data. The SNR was then re-calculated and compared to the original values.

.

## *5.3 RESULTS*

### 5.3.1 Effect of RIC and linac dose rate on MR images

The first three columns of Table 5-1 and Table 5-2 show the SNR values calculated for each imaging condition described in section 5.2.1for the phantoms imaged with the 10 cm and 3 cm coils, respectively. When the lead block stops the radiation from reaching the coil, the SNR stays relatively constant with linac dose rate for both coils; however, when the lead block is removed and the RF coils are irradiated there is a loss in SNR. Furthermore, the loss in SNR increases as the linac dose rate increases. A graphical representation of the data in Table 5-2 is shown in Figure 5.2.

**Table 5-1 - SNR for images acquired with 10 cm coil using a Gradient Echo sequence. SNR was calculated by taking the mean of the signal in the**

**magnitude image divided by the standard deviation of the noise in the real image.**

| Linac dose rate (MU/min) | Radiation beam blocked by lead block | Radiation beam incident upon MRI RF coil | After RIC noise is removed |
|---|---|---|---|
| 0 | 18.2 ± 0.2 | - | |
| 50 | 18.0 ± 0.4 | 17.7 ± 0.1 | 17.9 ± 0.1 |
| 100 | 17.8 ± 0.3 | 17.4 ± 0.3 | 17.8 ± 0.2 |
| 150 | 18.2 ± 0.3 | 16.9 ± 0.2 | 17.3 ± 0.2 |
| 200 | 17.8 ± 0.1 | 16.5 ± 0.2 | 17.2 ± 0.3 |
| 250 | 17.8 ± 0.1 | 16.2 ± 0.3 | 17.0 ± 0.5 |

**Table 5-2 - SNR for images acquired with 3 cm coil using a Gradient Echo sequence. SNR was calculated by taking the mean of the signal in the magnitude image divided by the standard deviation of the noise in the real image.**

| Linac dose rate (MU/min) | Radiation beam blocked by lead block | Radiation beam incident upon MRI RF coil | After RIC noise is removed |
|---|---|---|---|
| 0 | 19.7 ± 0.3 | - | |
| 50 | 19.5 ± 0.4 | 18.7 ± 0.3 | 19.1 ± 0.4 |
| 100 | 19.5 ± 0.3 | 18.0 ± 0.3 | 19.0 ± 0.2 |
| 150 | 19.5 ± 0.4 | 17.7 ± 0.4 | 19.0 ± 0.3 |
| 200 | 19.3 ± 0.2 | 17.0 ± 0.1 | 18.7 ± 0.3 |
| 250 | 19.1 ± 0.4 | 16.9 ± 0.3 | 18.7 ± 0.4 |

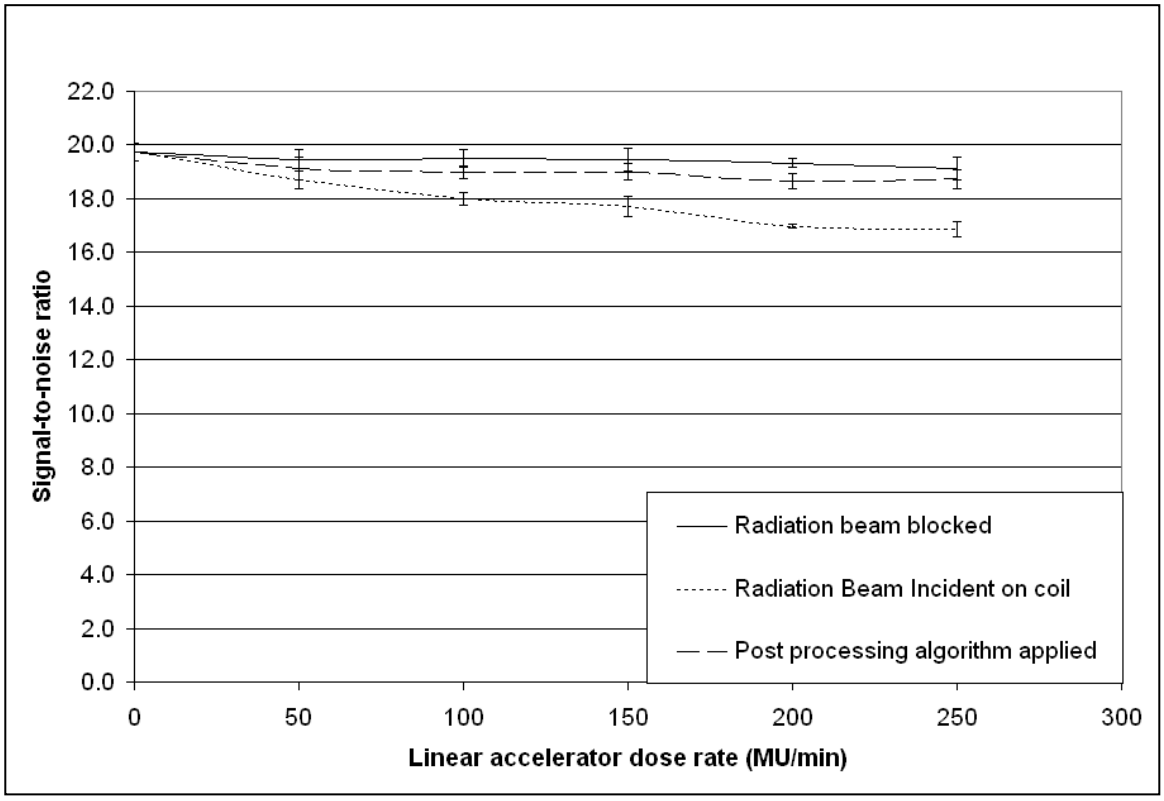


**Figure 5.2 - Signal to Noise ratio loss due to RIC in 3 cm Solenoid coil. The solid line shows the SNR when the radiation beam is blocked, the dotted line shows the SNR loss when the radiation beam is incident on the RF coil, and the dashed line shows the SNR after the use of a post-processing algorithm.**

The other objective of the experiments described in section 5.2.1 was to visualize the RIC artefact. As mentioned above, the k-space data was examined to accomplish this goal. To illustrate the need to examine the k-space data rather than the image itself we can look to Figure 5.3 and Figure 5.4. The two images shown in Figure 5.3and Figure 5.4 were taken with the 10 cm and 3 cm solenoid coil, respectively, with linac dose rates of 0 and 250 MU/min. Visual inspection alone does not show any artefact due to RIC, although the previous analysis shows a loss in SNR. Figure 5.5 shows the k-space data corresponding to the images in Figure 5.4. In the top panel, the k-space without radiation is shown. In

the bottom panel, the k-space data is shown for the case when the linac producing radiation at 250 MU/min that reaches the coil un-attenuated. The middle panel shows the k-space data from an image taken with a 250 MU/min dose rate where the beam was blocked from reaching the RF coil. Each k-space image has the same window and level applied for consistency. Here the RIC artefact is clearly visible in the k-space data of the image taken with a 250 MU/min linac dose rate, but is not visible in the other two k-space data sets. It is clear based on Figure 5.5 that the vertical lines in k-space are due to the RIC as they are only present when the linac is producing radiation and its beam is incident on the RF coil.

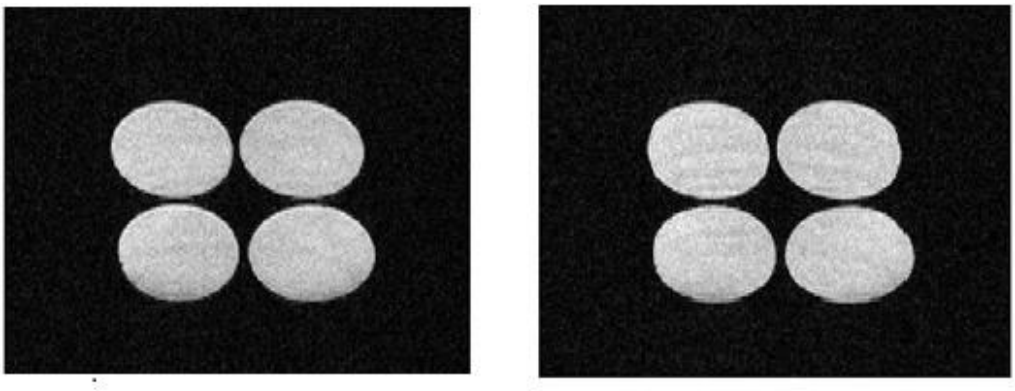

**Figure 5.3 - Sample images acquired with 10 cm solenoid coil. The images were acquired with the linac not producing radiation (left) and with linac producing radiation and RF coil unblocked at 250 MU/min (right). The RIC artefact is not visible.**

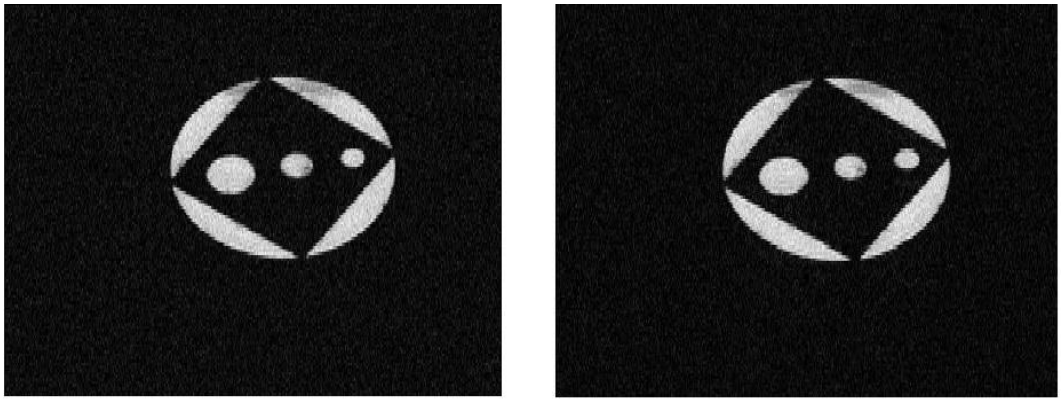

**Figure 5.4 - Sample images acquired with 3 cm solenoid coil. The images were acquired with the linac not producing radiation (left) and with linac producing radiation and RF coil unblocked at 250 MU/min (right). The RIC artefact is not visible.**

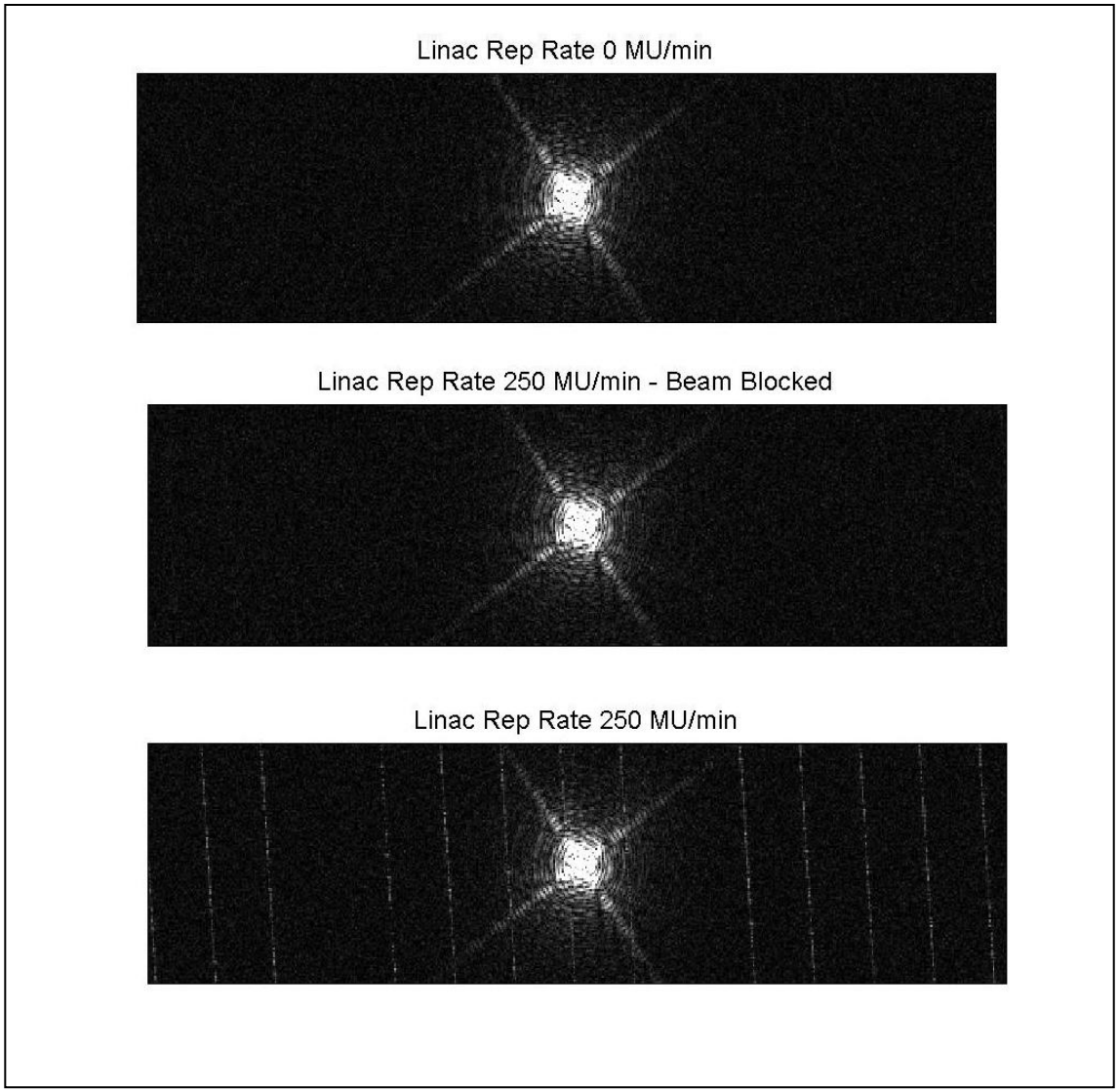


**Figure 5.5 - - K-space data from images acquired with linac dose rates of 0 and 250 MU/min. The top image was acquired with the radiation not pulsing. The middle image was acquired with a linac dose rate of 250 MU/min but the radiation beam was blocked from reaching the coil; it shows no RIC effects. The bottom image was acquired with a linac dose rate of 250 MU/min and the radiation beam incident on the RF coil; it clearly shows the RIC artefact, which presents itself as near vertical lines in k-space.**

### 5.3.2 Dependence of RIC artefact on imaging sequence

Table 5-3 and Table 5-4 contain the calculated SNR values for the imaging experiments using a spin echo and bSSFP sequences, respectively. Again when the radiation beam is stopped by a lead block the SNR remains essentially

constant at all linac dose rates. When the radiation beam is incident on the RF coil, there is a loss in SNR that increases with increasing dose rate.

**Table 5-3 - SNR for images acquired with 3cm coil using a Spin Echo Sequence. SNR was calculated by taking the mean of the signal in the magnitude image divided by the standard deviation of the noise in the real image.**

| Linac dose rate (MU/min) | Radiation beam blocked by lead block | Radiation beam incident upon MRI RF coil | After RIC noise is removed |
|---|---|---|---|
| 0 | 19.8 ± 0.3 | - | |
| 50 | 19.9 ± 0.3 | 19.2 ± 0.6 | 19.8 ± 0.4 |
| 100 | 19.7 ± 0.2 | 17.9 ± 0.6 | 19.3 ± 0.4 |
| 150 | 19.6 ± 0.4 | 17.4 ± 0.5 | 19.0 ± 0.6 |
| 200 | 19.4 ± 0.4 | 16.7 ± 0.7 | 18.8 ± 0.3 |
| 250 | 19.8 ± 0.3 | 16.3 ± 0.5 | 18.7 ± 0.4 |

**Table 5-4 - SNR for images acquired with 3 cm coil using a bSSFP sequence. SNR was calculated by taking the mean of the signal in the magnitude image divided by the standard deviation of the noise in the real image.**

| Linac dose rate (MU/min) | Radiation beam blocked by lead block | Radiation beam incident upon MRI RF coil | After RIC noise is removed |
|---|---|---|---|
| 0 | 20.2 ± 0.8 | - | |
| 50 | 20.1 ± 0.7 | 19.6 ± 0.2 | 20.1 ± 0.3 |
| 100 | 19.8 ± 0.7 | 19.4 ± 0.4 | 20.3 ± 0.6 |
| 150 | 20.1 ± 0.5 | 18.5 ± 0.6 | 19.6 ± 0.8 |

| | | | |
|---|---|---|---|
| 200 | 20.0 ± 0.5 | 16.9 ± 0.7 | 18.0 ± 1.1 |
| 250 | 19.9 ± 0.6 | 16.5 ± 0.4 | 17.8 ± 0.5 |

### 5.3.3 Dependence of RIC artefact on imaging parameter TR

The set of imaging experiments described in section 5.2.3 were designed to see differences in the RIC artefact, visible in k-space, when the imaging repetition time, TR, was changed. It should be stressed that the loss of SNR as a function of dose rate remained unaltered for all values of TR investigated. Figure 5.6 shows some representative images of the k-space data for the TR values specified in 5.2.3. It is immediately obvious that even a small change, 0.1 or 0.2 ms, in TR results in a large change in the k-space distribution of the RIC artefact. If the TR is changed from 300 to 299.8 or 300.1 ms, the slope of the lines seen in k-space changes dramatically and more lines are seen; 12 lines are seen in top image of Figure 5.6 (TR – 300 ms), while 14 are seen in the middle image (TR – 300.1 ms). When the TR is changed by larger amounts (i.e. 1 ms and up) the RIC appears as random background spikes, seen in the bottom image of Figure 5.6 (TR – 301 ms); a closer inspection shows that the random spikes are still regularly spaced on each read encode line (horizontal line). Aside from the SNR loss, the various k-space artefact patterns had no discernible effects in image space. This appearance of k-space spikes due to RIC is easily explained by examining the timing between the linear accelerator and the imaging sequence as discussed in Section 5.4.

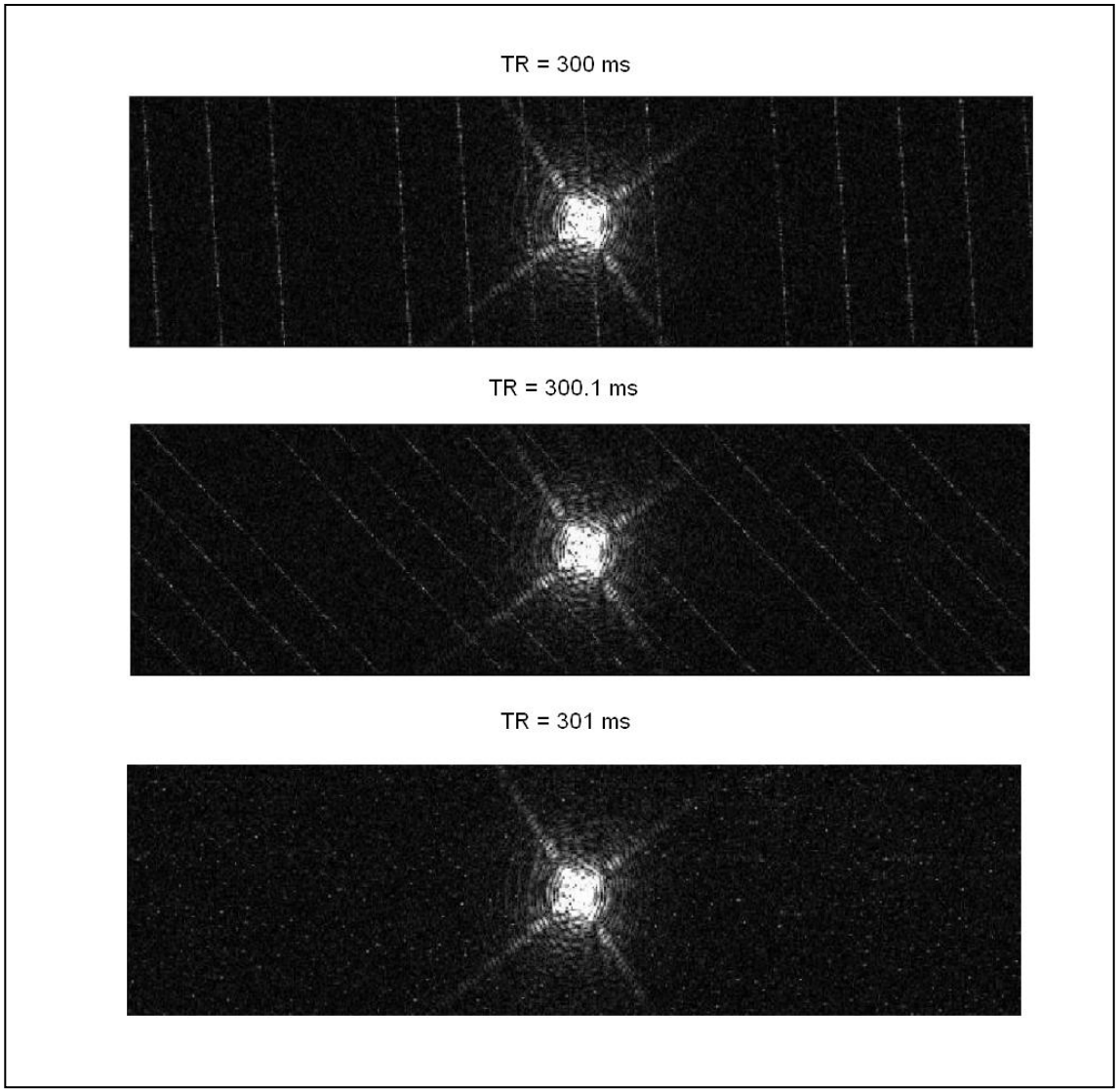


**Figure 5.6 - K-space data for gradient echo images taken with the 3 cm solenoid coil with TR = 300, 300.1 and 301 ms with a linac dose rate of 250 MU/min and the radiation beam incident on the RF coil. In the top image, TR=300 ms, the linac pulses an integer number (54) of times during this TR so the lines seen in k-space due to RIC are nearly vertical. In the middle image, TR=300.1 ms, there are no longer an integer number of linac pulses during this TR, resulting in timing shifts between successive horizontal (read encode) lines in k-space. Therefore, the lines seen in k-space due to RIC are now slanted from left to right. In the bottom image, TR = 301 ms, the shift between RIC noise pixels in subsequent horizontal (read encode) lines in k-space is now so large that the RIC artefact appears to be random; however, closer inspection shows that it is still regularly spaced on each read encode line.**

### 5.3.4 Removal of RIC artefact from MR data using post-processing

The results of the post-processing algorithm can be seen qualitatively in Figure 5.7 and quantitatively in the final column of Table 5-1, Table 5-2, Table

5-3, and Table 5-4. Figure 5.7 shows the same k-space image, acquired with the 10 cm coil, before and after the algorithm is applied. It is evident that the majority of the RIC artefact has been removed from the k-space data. Table 5-1 throughTable 5-4 show that image SNR can be recovered by using the post-processing algorithm. In all cases, but particularly at higher dose rates (200 and 250 MU/min), there is a useful gain in SNR when the data are processed to remove the RIC noise.

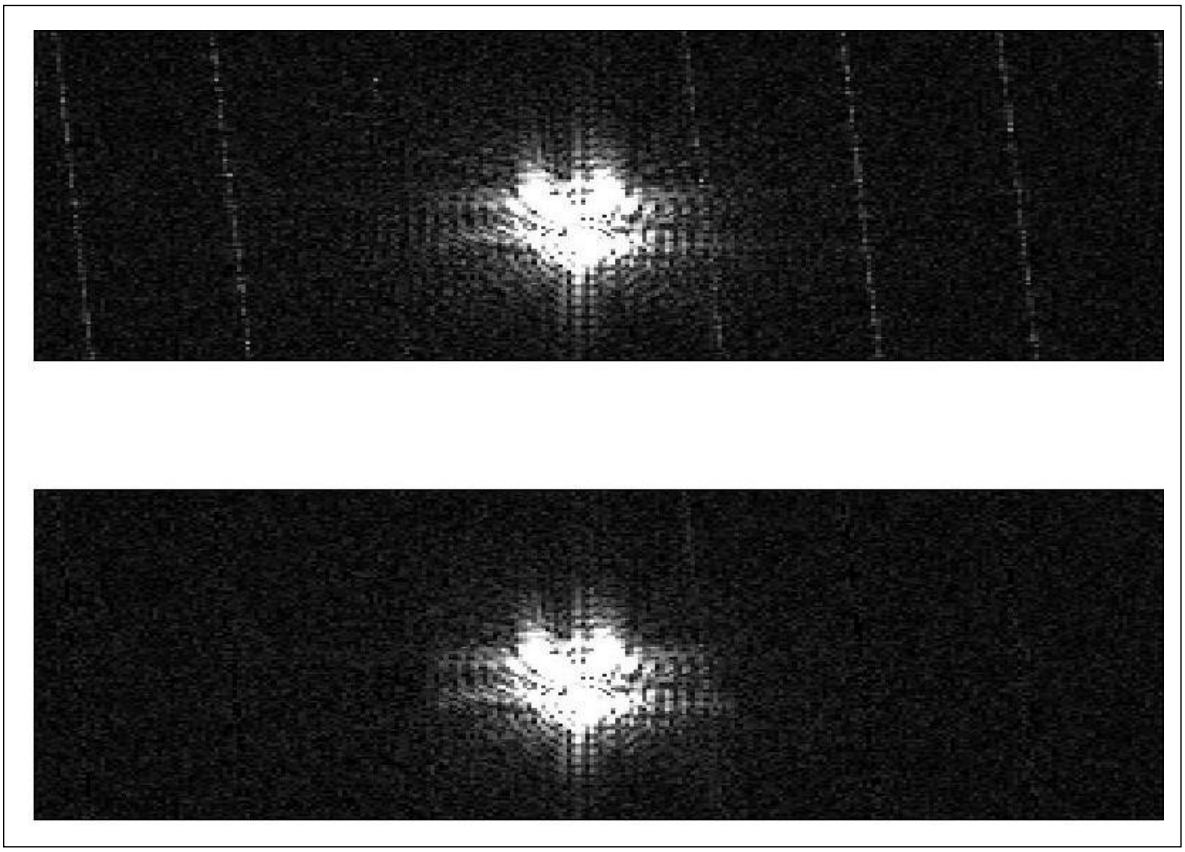

**Figure 5.7 - K-space data from 256x128 gradient echo image acquired with 10 cm coil. TR = 300 ms, linac dose rate = 250 MU/min. Top image is original k-space data and bottom image is k-space data after RIC removal algorithm has been applied. The RIC noise is effectively removed from the k-space data and SNR is recovered. SNR of top image = 16.2, SNR of bottom image = 17.3**

## 5.4 Discussion

The images in Figure 5.3 and Figure 5.4 show that the effect of RIC in MR imaging is not always visually obvious, i.e. the loss in SNR reported in Table 5-1, Table 5-2, Table 5-3, and Table 5-4 is not easily noticed in the images. When instead, the k-space data is examined visually (Figure 5.5) the RIC related noise spikes are immediately obvious. Since these spikes are only present when the linac is producing radiation and the beam is incident on the RF coil, these must be caused by RIC. Table 5-1 throughTable 5-4 also illustrate the dependence of the artefact on the linac dose rate. As the dose rate increases, the SNR of the corresponding images is increasingly degraded. Though not shown, the number of lines seen in k-space also increases with increasing linac dose rate. It is expected as the linac nominally pulses at 180 Hz, but will drop pulses in order to achieve the desired dose rates; thus, the 50 MU/min rate will have approximately 5 times fewer pulses per minute than the 250 MU/min rate. The increasing number of lines seen in k-space at higher dose rates will increase the overall image noise, thus decreasing the SNR as seen in Table 5-1 throughTable 5-4. This investigation is limited to a dose rate of 250 MU/min due to the limits of the Varian 600C linac. If the linac dose rate is further increased by increasing the pulse repetition frequency, as in the high energy linacs that pulse at 360 Hz, then the SNR degradation at higher dose rates is likely to increase. Also, our previous investigation [Burke, et al., 2010] demonstrated that the RIC amplitude increases proportionally with the irradiated area of RF coil. Thus, the RIC induced degradation of SNR may be different in human sized coils. The largest SNR loss

from ~20 to ~16 is not visually discernible in these small images; however, the importance of SNR should be looked at in the context of real-time imaging with respect to auto-detection of tumour needed for tracking [Yun, et al., 2012].

The SNR loss seen with increasing linac dose rate appears to be largely independent of MR imaging sequence. The SNR loss at 250 MU/min, compared to no radiation, for the gradient echo, spin echo and bSSFP sequences are ~ 15 %, 18 % and 18 %, respectively. It was initially expected that the bSSFP sequence might be less affected by the RIC since its acquisition time is very short and less RIC spikes would be present in the MR data. However, in this fast sequence the magnitude of the MR signal is smaller compared to the other two sequences. This smaller signal means that the magnitude of the RIC signal is comparatively larger in this case and although there are fewer RIC spikes in the data, they still raise the background noise level significantly – thus lowering the SNR. It should be noted that the bSSFP is the sequence of choice for real-time imaging [Yun, et al., 2012].

Alteration of the MR imaging parameter TR has interesting visual effects that occur due to the interplay between linac pulse timing and TR. Figure 5.6 demonstrates the effect of changing TR – the lines in k-space change their slope with small changes (0.1 ms) and appear as random spikes with larger changes. Changing the parameter TR only changes the appearance of the RIC artefact; RIC's effect on SNR remains constant for a given linac dose rate. This phenomenon is explained by examining the timing mechanisms of the linac and MR systems.

The linear accelerator pulses with a frequency of 180 Hz and, if no pulses are dropped, this leads to 1 radiation pulse every ~ 5.6 ms, with a width of approximately 5 μs per pulse. Examining the original imaging sequence with a TR of 300 ms, a simple calculation reveals 54 (300 ms * 180 pulses/s) radiation pulses per TR – not all of these are seen in k-space because the actual acquisition time, $t_{acq}$, for the MR sequence is much shorter than the total TR. This exact integer multiple means that the radiation pulses will occur at approximately the same sampling points along a given read encode k-space line (read encode lines are horizontal lines in k-space which are acquired during a single TR), resulting in a near vertical line in k-space (Figure 5.6 top image). Changing TR even by a small amount, such as 0.1 ms to 300.1 ms, means that the number of radiation pulses per TR is no longer an exact integer multiple (300.1 ms * 180 Hz = 54.02) so the radiation pulses will shift along the read direction resulting, in this case, a line sloping downward from left to right (Figure 5.6 middle image). When TR is changed by a larger amount, for example to 301ms (54.2 pulses per TR), the shift in location of RIC spikes between subsequent read encode lines becomes so large that the noise appears random (Figure 5.6 bottom image), though on closer examination the noise spikes due to RIC are still spaced the same distance apart on each read encode line of k-space – as is expected because the linac is still pulsing at 180 Hz.

In a separate investigation, we have shown that the RIC results from the lack of electronic equilibrium in the conductor of the RF coil (Section 4). In theory, the RIC can be reduced by establishing electronic equilibrium with

appropriate buildup material and thickness. However, the placement of build up may have negative consequences on the patient`s skin dose, thus we have attempted a post-processing method of RIC removal in this investigation. This simple post-processing algorithm showed promising results, as seen in the final column of Table 5-1throughTable 5-4, and a large percentage of the lost image SNR was restored. Though not shown, the algorithm works equally well for images taken with various TR values, i.e. it does not depend on the structural distribution of actual spikes in k-space. At this point the algorithm relies on the user to manually import the MR data and run the post-processing algorithm in MATLAB; however, future plans involve full automation of the algorithm and the incorporation into the imaging chain so that the k-space data are processed as they are acquired, rather than post-acquisition. To accomplish this goal, the current algorithm may need to be altered in order to examine points line by line as they are acquired, rather than using the algorithm from Section 5.2.4, which is applied after all data is acquired.

## *5.5 Conclusions and future work*

The data presented shows that radiation induced current, present when RF coils are irradiated by linear accelerators and visible as signal spikes in the image k-space data, can negatively affect MR images by lowering the image SNR. The amount of SNR loss increases with increasing linac dose rates. In a typical treatment regime high dose rates, 250 MU/min and above, are routinely used to provide the patient with short treatment times. At these high rates there is significant SNR loss, some of which can be recovered through the use of a post-

processing algorithm which removes the RIC artefact from the image k-space data.

Future work will involve automating the RIC-removal algorithm and possibly its incorporation into the image acquisition chain. While it would be possible to synchronize the linac with the MRI so that no acquisition occurs during beam-on time, this would severely limit the real-time benefits of an integrate linac-MR system and so is not desirable.

## 5.6 References


Burke, B., Fallone, B., & Rathee, S. (2010). Radiation induced currents in MRI RF coils: application to linac/MRI integration. *Physics in Medicine and Biology, 55*, 735-746.

Fallone, B. G., Carlone, M., Murray, B., Rathee, S., Stanescu, T., Steciw, S., et al. (2007). Development of a Linac-MRI system for real-time ART. *Medical Physics*, 2547.

Fallone, B., Murray, B., Rathee, S., Stanescu, T., Steciw, S., Vidakovic, S., et al. (2009). First MR images obtained during megavoltage photon irradiation from a prototype integrated linac-MR system. *Medical Physics, 36* (6), 2084-2088.

Lamey, M., Burke, B., Blosser, E., Rathee, S., De Zanche, N., & Fallone, B. (2010a). Radio frequency shielding for a linac-MRI system. *Physics in Medicine and Biology, 55*, 995-1006.

Yun, J., Yip, E., Wachowicz, K., Rathee, S., Mackenzie, M., Robinson, D., et al. (2012). Evaluation of a lung tumor autocontouring algorithm for intrafractional

tumor tracking using low-field MRI: A Phantom Study. *Medical Physics, 39* (3), 1481-1494.

# 6 Conclusions, Summary and Future Work

An integrated linac-MR system for real-time image guided radiotherapy has been designed and constructed at the University of Alberta/Cross Cancer Institute. One of the obstacles associated with such a system is the transient radiation induced current in MRI RF coils exposed to the linac's pulsed radiation beam and the work presented in this thesis was concerned with studying this RIC. The chapters of this thesis were divided into three distinct, but related, investigations of RIC.

Chapter 3 contained preliminary measurements which measured the RIC in MRI RF coils subjected to the pulsed radiation of typical clinical linacs. The measurements showed that the RIC has duration proportionate to the duration of the linac radiation pulse. The frequency analysis of the measured RIC signal determined that the RIC noise is broadband noise and could thus be present in MR images. The conductive windings of the RF coils were isolated as the main source of RIC. The RIC showed a linear dependence on dose rate, which further proved that the noise was caused by radiation and not by RF. Wax buildup applied to the RF coil was shown to reduce the magnitude of the RIC, but not eliminate it, which supports the hypothesis that an electronic disequilibrium in the conductive windings of the RF coils is the source of the RIC seen in MRI RF coils.

Chapter 4 expanded on the conclusions of chapter 3, namely, attempting to establish electronic equilibrium in the coil windings, thus reducing or eliminating the RIC noise, through the application of buildup. A Monte Carlo script was written for the Monte Carlo radiation simulation program PENELOPE

specifically to calculate the RIC in a volume of interest. Simulations were performed mimicking the planar measurement setup used by A. Ghila to validate the simulation algorithm and then to simulate the effectiveness of using buildup material to reduce to RIC seen in conductors. The measurements and simulations confirmed that buildup can effectively be used in a planar setup to significantly reduce the magnitude of the RIC. This was tested on an aluminum surface coil using Teflon buildup material and shown to reduce the RIC magnitude by 92% using only 0.9 cm of Teflon. Cylindrical coil geometries simulations showed that buildup can be effective in these situations only if the air gap between the coil and the patient is minimized. Large air gaps significantly reduce the effectiveness of RIC removal with buildup. Magnetic fields were then introduced into both the planar and cylindrical simulations and were not seen to significantly alter the effectiveness of the buildup method, minimizing the air gap is a much more important consideration. Finally, a cylindrical buildup was constructed and applied to an RF coil exposed to the pulsed radiation of the linac-MR. The SNR lost due to RIC was shown to be reduced through the use of buildup – up to 55% of the lost SNR was recovered in this simple setup.

Chapter 5 examines the appearance and the effect of RIC on MR imaging. The RIC appeared as visible noise spikes in the image k-space data and was shown to be present only when radiation was incident on the RF coils. MR images showed a loss in SNR which increased with increasing linac dose rates. There is significant SNR loss, up to ~ 15% in our experiments (Table 5-2), when high dose rates (250 MU/min) were used and these are commonly used in clinical

treatments. Some of the SNR was recovered through the use of an image post-processing algorithm which removed some of the RIC-corrupted MR k-space data.

There are several possible directions for future work stemming from the work presented in this thesis. The buildup method described in Chapter 4 should be explored further with specially designed and constructed RF coils. Chapter 4 showed that the presence of air between the buildup and coil, and between the coil and patient can significantly reduce the effectiveness of buildup. The buildup-coil combination that we used for the imaging experiment in § 4.3.6 was extremely rudimentary and definitely contained gaps between the buildup and coil. Specially designed coils should have the buildup snuggly fitted around the coil windings. This should increase the effectiveness of the buildup.

The dosimetric effects of having RF coils, and potentially RF coils with buildup, in the radiation beam path needs to be investigated. The presence of the RF coils in the radiation beam path could affect both the patient surface dose through increased scatter and the dose at depth by altering the spectrum of the photon beam through the absorption of some of the low energy photons.

The post-processing algorithm described in Chapter 5 currently processes the k-space data after the images are acquired and requires some input from the user regarding the size of the k-space matrix. This algorithm could be automated and could also be integrated as part of the image acquisition chain so that the corrupted data is removed before the image is generated. This is necessary if the processed images are to be used in conjunction with real-time image guidance.

There are also a few research directions which are tangentially related to this work. A method to remove both the RIC and the dosimetric problems caused by RF coils would be to investigate RF coils which would be constructed to be outside the radiation beam. An example of this would be Maxwell pair-type RF coil in which the space between the two coils would be sufficient for the radiation beam to pass through. A third method for RIC removal could also be investigated, where a 'detector' would be placed in the radiation beam path to measure RIC. This detector would be connected to a parallel branch of the MR signal acquisition chain and the measured RIC signal would be subtracted from the acquired MR raw data in order to remove the RIC noise from all affected data points. In theory this type of system could provide RIC-noise free images with essentially no increase in imaging time.

The work presented in this thesis has shown that RIC is present in the MRI RF coils used in integrated linac-MR systems and can affect the SNR of images acquired with such a system. Two separate methods were shown which reduced the RIC magnitude and improved the SNR of the acquired images. RIC will be present in all RF coils that are exposed to the pulsed radiation of a linac, but this work has shown that the severity of the problem can be reduced and that high quality images can still be acquired.

# 7 Bibliography

Abdel-Rahman, W., Seuntjens, J. P., Verhaegen, F., & Podgorsak, E. B. (2006). Radiation induced currents in parallel plate ionization chambers: Measurement and Monte Carlo simulation for megavoltage photon and electron beams. *Medical Physics , 33* (9), 3094-3104.

Balter, J., Wright, J., Newell, J., Friemel, B., Dimmer, S., Cheng, Y., et al. (2005). Accuracy of a wireless localization system for radiotherapy. *International Journal of Radiation Oncology*Biology*Physics , 61* (3), 933-937.

Bernier, J., Hall, E., & Giaccia, A. (2004). Radiation oncology: a century of achievemens. *Nature Reviews Cancer , 4*, 737-747.

Burke, B., Fallone, B., & Rathee, S. (2010). Radiation induced currents in MRI RF coils: application to linac/MRI integration. *Physics in Medicine and Biology , 55*, 735-746.

Burke, B., Ghila, A., Fallone, B. G., & Rathee, S. (2012). Radiation induced current in the RF coils of integrated linac-MR systems: The effect of buildup and magnetic field. *Medical Physics , 39*, 5004-5014.

Burke, B., Lamey, M., Rathee, S., Murray, B., & Fallone, B. (2009). Radio frequency noise from clinical linear accelerators. *Physics in Medicine and Biology , 54*, 2483-2492.

Burke, B., Wachowicz, K., Fallone, B. G., & Rathee, S. (2012). Effect of radiation induced current on the quality of MR images in an integrated linac-MR system. *Medical Physics , 39* (10), 6139-6147.

Chowdhury, N., Toth, R., Chappelow, J., Kim, S., Motwani, S., Punekar, S., et al. (2012). Concurrent segmentation of the prostate on MRI and CT via linked statistical shape models for radiotherapy planning. *Medical Physics , 39* (4), 2214-2228.

Dawson, L., & Jaffray, D. (2007). Advances in Image-Guided Radiation Therapy. *Journal of Clinical Oncology , 25* (8), 938-946.

Degenhart, H. J., & Schlosser, W. (1961). Transient effects of pulsed nuclear radiation on electronic parts and materials. *IRE Transactions on Component Parts* , 124-128.

Dempsey, J. (2006). An Image-guided device providing 4D cine MRI simultaneous to radiotherapy delivery. *Journal of Radiotherapy in Practice , 5* (3), 179.

Fallone, B. G., Carlone, M., Murray, B., Rathee, S., Stanescu, T., Steciw, S., et al. (2007). Development of a Linac-MRI system for real-time ART. *Medical Physics* , 2547.

Fallone, B., Murray, B., Rathee, S., Stanescu, T., Steciw, S., Vidakovic, S., et al. (2009). First MR images obtained during megavoltage photon irradiation from a prototype integrated linac-MR system. *Medical Physics , 36* (6), 2084-2088.

Fowler, J. F. (1956). X-ray induced conductivity in insulating materials. *Proceedings of the Royal Society of London A , 236* (1207), 464-480.

Gross, B. (1980). *Radiation-induced charge storage and polarization effects.* (G. M. Sessler, Ed.) Berlin Heidelberg New York: Spinger-Verlag.

Hosiak, J., Sixel, K., Tirona, R., Cheung, P., & Pignol, J. (2004). Correlation of lung tumor motion with external surrogate indicators of respiration. *International Journal of Radiation Oncology*Biology*Physics , 60* (4), 1298-1306.

Hu, Y., Pehchenaya Green, O., Parikh, P., Olsen, J., & Mutic, S. (2012). TH-E-BRA-07: Initial Experience with the ViewRay system - Quality Assurance Testing of the Imaging Component. *Medical Physics , 39*, 4013.

ICRU50. (1993). *Prescribing, Recording and Reporting Photon Beam Therapy.* Bethesda: ICRU.

ICRU62. (1999). *Prescribing, Recording and Reporting Photon Beam Therapy.* Bethesda: ICRU.

ICRU85. (2011). *Fundamental quantities and units for ionizing radiation (revised).* Oxford University Press.

Johns, H. E., & Cunningham, J. R. (1983). *The physics of radiology* (4th ed.). Springfield, Illinois, U.S.A.: Charles C Thomas.

Johns, H. E., Aspin, N., & Baker, R. G. (1958). Currents induced in the dielectrics of ionization chambers through the action of high energy radiation. *Radiation Research , 9*, 573-588.

Karzmark, C. J., Nunan, C. S., & Tanabe, E. (1993). *Medical Electron Accelerators.* New York: McGraw-Hill.

Keyvanloo, A., Burke, B., Tadic, T., Warkentin, B., Kirkby, C., Rathee, S., et al. (2012). WE-E-BRB-06: Monte Carlo Calculations of the Skin Dose for Longitudinal Linac-MR System Using Realistic Three-Dimensional Magnetic Field Modeling. *Medical Physics , 39*, 3957.

Keyvanloo, A., Burke, B., Warkentin, B., Tadic, T., Rathee, S., Kirkby, C., et al. (2012). Skin dose in longitudinal and transverse linac-MRIs using Monte Carlo and realistic 3D MRI models. *Medical Physics , 39* (10), 6509-6521.

Kim, S., & Suh, T.-S. (2006). Imaging in radiation therapy. *Nuclear Engineering and Technology , 38* (4), 327-342.

Kirkby, C., Murray, B., Rathee, S., & Fallone, B. (2010). Lung dosimetry in a linac-MRI radiotherapy unit with a longitudinal magnetic field. *Medical Physics , 37* (9), 4722-4732.

Kirkby, C., Stanescu, T., & Fallone, B. (2009). Magnetic field effects on the energy deposition spectra of MV photon radiation. *Physics in Medicine and Biology , 54*, 243-257.

Kirkby, C., Stanescu, T., Rathee, S., Carlone, M., Murray, B., & Fallone, B. (2008). Patient dosimetry for hybrid MRI-radiotherapy systems. *Medical Physics , 35* (3), 1019-1027.

Kuperman, V. L. (2000). *Magnetic Resonance Imaging: Physical Principles and Applications.* San Diego: Academic Press.

Lagendijk, J., Raaymakers, B., Raaijmakers, A., Overweg, J., Brown, K., Kerkhof, E., et al. (2008). MRI/linac integration. *Radiotherapy and Oncology , 86*, 25-29.

Lamey, M., Burke, B., Blosser, E., Rathee, S., De Zanche, N., & Fallone, B. (2010a). Radio frequency shielding for a linac-MRI system. *Physics in Medicine and Biology , 55*, 995-1006.

Lamey, M., Rathee, S., Johnson, L., Carlone, M., Blosser, E., & Fallone, B. (2010c). Radio frequency noise from the modulator of a linac. *IEEE Transactions on Electromagnetic Compatibility , 52* (3), 530-536.

Lamey, M., Yun, J., Burke, B., Rathee, S., & Fallone, B. (2010b). Radio frequency noise from an MLC: a feasibility study of the use of an MLC for linac-MR systems. *Physics in Medicine and Biology , 55*, 981-994.

Langen, T., & Jones, D. (2001). Organ motion and its management. *International Journal of Radiation Oncology*Biology*Physics , 50* (1), 265-278.

Mackie, T., Balog, J., Ruchala, K., Shepard, D., Alrdridge, S., Fitchard, E., et al. (1999). Tomotherapy. *Seminars in Radiation Oncology , 9* (1), 108-117.

Mackie, T., Holmes, T., Swerdloff, S., Reckwerdt, P., Deasy, J., Yang, J., et al. (1993). Tomotherapy: A new concept for the delivery of dynamic conformal radiotherapy. *Medical Physics , 20* (6), 1709-1719.

Meyer, R. A., Bouquet, F. L., & Alger, R. S. (1956). Radiation induced conductivity in Polyethylene and Teflon. *Journal of Applied Physics , 27* (9), 1012-1018.

Mutic, S. (2012). WE-A-BRA-02: First Commercial Hybrid MRI-IMRT System. *Medical Physics , 39*, 3934.

Nahum, A. (2007). *Handbook of radiotherapy physics: theory and practice.* (A. N. P. Mayles, Ed.) Boca Raton, Florida, U.S.A.: Taylor and Francis Group.

Nurushev, T., Kim, J., Hearshen, D., Pantelic, M., Kotys-Traughber, M., Elshaikh, M., et al. (2011). SU-E-J-78: Initial Experience with MR Simulation in

Radiation Therapy Using An Open-Platform MR Scanner: Considerations for Routine Clinical Use. *Medical Physics* , 3460.

Raaijmakers, A. J., Raaymakers, B. W., & lagendijk, J. J. (2005). Integrating a MRI scanner with a 6 MV radiotherapy accelerator: dose increase at tissue-air interfaces in a lateral magnetic field due to returning electrons. *Physics in Medicine and Biology , 50*, 1363-1376.

Raaijmakers, A., Raaymakers, B., & Lagendijk, J. (2007b). Experimental verification of magnetic field dose effects for the MRI-accelerator. *Physics in Medicine and Biology , 52*, 4283-4291.

Raaijmakers, A., Raaymakers, B., van der Meer, S., & Lagendijk, J. (2007a). Integrating a MRI scanner with a 6MV radiotherapy accelerator: impact of the surface orientation on the entrance and exit dose due to the transverse magnetic field. *Phyics in Medicine and Biology* , 929-939.

Raaymakers, B., Lagendijk, J., Overweg, J., Kok, J., Raaijmakers, A., Kerkhof, E., et al. (2009). Integrating a 1.5 T MRI scanner with a 6 MV accelerator: proof of concept. *Physics in Medicine and Biology , 54* (12), N229-N237.

Raaymakers, B., Raaijmakers, A., Kotte, A., Jette, D., & Lagendijk, J. (2004). Integrating a MRI scanner with a 6MV radiotherapy accelerator: dose deposition in a transverse magnetic field. *Physics in Medicine and Biology , 49*, 4109-4118.

Rieke, V., Ganguly, A., Daniel, B. L., Scott, G., Pauly, J. M., Fahrig, R., et al. (2005). X-ray compatible radiofrequency coil for magnetic resonance imaging. *Magnetic Resonance in Medicine* , 1409-1414.

Rietzel, E., Rosenthal, S., Gierga, D., Willett, C., & Chen, G. (2004). Moving targets: detection and tracking of internal organ motion for treatment planning and patient set-up. *Radiotherapy & Oncology , 73*, S68-72.

Russ, J. C. (2002). *The Image Processing Handbook 4th Edition.* Boca Raton: CRC Press.

Salvat, F., Fernandez-Varea, J., & Sempau, J. (2009). *PENELOPE-2008, A code system for Monte Carlo simulation of electron and photon transport.* Barcelona: OECD Nuclear Energy Agency.

Santos, D., St. Aubin, J., Fallone, B., & Steciw, S. (2012). Magnetic shielding investigation for a 6 MV in-line linac within the parallel configuration of a linac-MR system. *Medical Physics , 39* (2), 788-797.

Sato, F., Tanaka, T., Kagawa, T., & Iida, T. (2004). Impedance measurements of thin film ceramics under ion beam irradiation. *Journal of Nuclear Materials , 329-333*, 1034-1037.

Sessler, G. M. (1980). *Topics in applied physics volume 33: Electrets.* (G. M. Sessler, Ed.) Berlin Heidelberg New York: Spinger-Verlag.

St. Aubin, J., Santos, D., Steciw, S., & Fallone, B. (2010d). Effect of longitudinal magnetic fields on a simulated 6 MV linac. *Medical Physics , 37*, 4916-4923.

St. Aubin, J., Steciw, S., & Fallone, B. (2010b). An integrated 6 MV linear accelerator model from electron gun to dose in a water tank. *Medical Physics , 37*, 2279-2288.

St. Aubin, J., Steciw, S., & Fallone, B. (2010c). Effect of transverse magnetic fields on a simulated in-line 6 MV linac. *Physics in Medicine and Biology , 55*, 4861-4869.

St. Aubin, J., Steciw, S., & Fallone, B. (2010f). Magnetic decoupling of the linac in a low field bi-planar linac-MR system. *Medical Physics , 37*, 4755-4761.

St. Aubin, J., Steciw, S., & Fallone, B. (2010a). The design of a simulated in-line side-coupled 6 MV linear accelerator waveguide. *Medical Physics , 37*, 466-476.

St. Aubin, J., Steciw, S., & Fallone, B. (2010e). Waveguide detuning caused by transverse magnetic fields on a simulated in-line 6 MV linac. *Medical Physics , 37*, 4751-4754.

Stanescu, T., Jans, H.-S., Pervez, N., Stavrev, P., & Fallone, B. (2008). A study on the magnetic resonance imaging (MRI)-based radiation treatment planning of intracranial lesions. *Physics in Medicine and Biology , 53*, 3679-3693.

Tadic, T., & Fallone, B. (2010). Design and optimization of a novel bored biplanar permanent-magnet assembly for hybrid magnetic resonance imaging systems. *IEEE transactions on magnetics , 46* (12), 4052-4058.

Tadic, T., & Fallone, B. (2012). Design and optimization of superconducting MRI magnet systems with magnetic materials. *IEEE Transactions on Applied Superconductivity* , 1-11.

Tadic, T., & Fallone, B. (2011). Three-Dimensional nonaxisymmetric pole piece shape optimization for biplanar. *IEEE Transactions on Magnetics , 47* (1), 231-238.

Van Dyke, J. (1999). *The modern technology of radiation oncology: A compendium for medical physicists and radiation oncologists.* Madison: Medical Physics Publishing.

van Herk, M. (2004). Errors and margins in radiotherapy. *Seminars in radiation oncology , 14* (1), 52-54.

Vedam, S., Kini, V., Keall, P., Ramakrishnan, V., Mostafavi, H., & Mohan, R. (2003). Quantifying the predictability of diaphram motion during respiration with a non-invasive external marker. *Medical Physics , 30* (4), 505-513.

Verellen, D., De Ridder, M., Linthout, N., Tournel, K., Soete, G., & Storme, G. (2007). Innovations in image-guided radiotherapy. *Nature Reviews Cancer , 7*, 949-960.

Wachowicz, K., Stanescu, T., Thomas, S., & Fallone, B. (2010). Implications of tissue magnetic susceptibility-related distortion on the rotating magnet in an MR-linac design. *Medical Physics , 37* (4), 1714-1721.

Webb, S. (2006). Motion effects in (intensity modulated) radiation therapy: a review. *Physics in Medicine and Biology , 51*, R403-R425.

Wilman, A., & Beaulieu, C. (2006). *Course notes for BME 564.*

Yun, J., St. Aubin, J., Rathee, S., & Fallone, B. (2010). Brushed permanent magnet DC MLC motor operation in an external magnetic field. *Medical Physics , 37* (5), 2131-2134.

Yun, J., Yip, E., Wachowicz, K., Rathee, S., Mackenzie, M., Robinson, D., et al. (2012). Evaluation of a lung tumor autocontouring algorithm for intrafractional

tumor tracking using low-field MRI: A Phantom Study. *Medical Physics , 39* (3), 1481-1494.